3-14-2014

Automated Driftmeter Fused with Inertial Navigation

Allan D. Tuma

AUTOMATED DRIFTMETER FUSED WITH INERTIAL NAVIGATION

THESIS

Allan D. Tuma, Second Lieutenant, USAF

AFIT-ENG-14-M-79

DEPARTMENT OF THE AIR FORCE
AIR UNIVERSITY

AIR FORCE INSTITUTE OF TECHNOLOGY

Wright-Patterson Air Force Base, Ohio

AFIT-ENG-14-M-79

AUTOMATED DRIFTMETER FUSED WITH INERTIAL NAVIGATION

THESIS

Presented to the Faculty

Department of Electrical and Computer Engineering

Graduate School of Engineering and Management

Air Force Institute of Technology

Air University

Air Education and Training Command

in Partial Fulfillment of the Requirements for the

Degree of Master of Science in Electrical Engineering

Allan D. Tuma, B.S.E.E.

Second Lieutenant, USAF

March 2014

AFIT-ENG-14-M-79

AUTOMATED DRIFTMETER FUSED WITH INERTIAL NAVIGATION

Allan D. Tuma, B.S.E.E.
Second Lieutenant, USAF

Approved:

//signed//	14 March 2014
Dr. Meir Pachter, PhD (Chairman)	Date
//signed//	14 March 2014
Major Marshall Haker, PhD (Member)	Date
//signed//	14 March 2014
Dr. Kyle J. Kauffman, PhD (Member)	Date

AFIT-ENG-14-M-79

Abstract

The motivation of this research is to address the use of bearing-only measurements taken by an optical sensor to aid an Inertial Navigation System (INS) whose accelerometers and gyroscopes are subject to drift and bias errors. The concept of Simultaneous Localization And Mapping (SLAM) is employed in a bootstrapping manner: the bearing measurements are used to geolocate ground features, following which the bearings taken over time of the said ground features are used to improve the navigation state provided by the INS. In this research the INS aiding action of tracking stationary, but unknown, ground features over time is evaluated. It does not, however, address the critical image registration issue associated with image processing. It is assumed that stationary ground features are able to be detected and tracked as pixel representations by a real-time image processing algorithm.

Simulations are performed which indicate the potential of this research. It is shown that during wings level flight at constant speed and fixed altitude, an aircraft that geolocates and tracks ground objects can significantly reduce the error in two of its three dimensions of flight, relative to an Earth-fixed navigation frame. The aiding action of geolocating and tracking ground features, in-line with the direction of flight, with a downward facing camera did not provide improvement in the aircraft's x-position estimate. However, the aircraft's y-position estimate, as well as the altitude estimate, were significantly improved.

Table of Contents

Page

Page

List of Figures

List of Tables

List of Abbreviations

Abbreviation		Page
GPS	Global Positioning System	1
AFIT	Air Force Institute of Technology	1
INS	Inertial Navigation System	5
SAMSO	Air Force Space and Missile Organization	6
NRL	Naval Research Laboratory	6
JCS	Joint Chiefs of Staff	6
NAVSEG	Navigation Satellite Executive Steering Group	6
SPS	Standard Positioning Service	6
PPS	Precise Positioning Service	6
LOS	Line of Sight	6
IMU	Inertial Measurement Unit	7
SLAM	Simultaneous Localization and Mapping	8
SIFT	Scale Invariant Feature Transform	9
SURF	Speeded Up Robust Features	9
FOV	field of view	9
MP	megapixel	11
NED	North-East-Down	17
DCM	direction cosine matrix	20
RLG	ring laser gyro	22
FOG	fiber optic gyroscope	22
KF	Kalman filter	24
R_{LOS}	line-of-sight range	33

AUTOMATED DRIFTMETER FUSED WITH

INERTIAL NAVIGATION

I. Introduction

Much work has been accomplished in recent years to reduce the military's dependence on the Global Positioning System (GPS). General Norton Schwartz, the 19^{th} Chief of Staff of the Air Force, was quoted in January of 2010 as saying,

> Global positioning has transformed an entire universe of war-fighting capability. Our dependence on precision navigation in time will continue to grow,... It seemed critical to me that the joint force reduce its dependence on GPS aid... Our operations cannot grind to a halt for a degraded or denied system,... We must ... proceed to build more resilient systems... [3]

This thesis develops a theoretical analysis of an integrated airborne navigation system fusing optical and inertial measurements. The specific focus is on autonomy where GPS signals are not available, but precision navigation is achieved through the use of passive self-contained sensors. This work is a follow-on to previous research efforts at the Air Force Institute of Technology (AFIT), utilizing a strategy of fusing bearing measurements with an optical sensor and inertial navigation [3], [4], [5]. This research continues to investigate the use of bearing measurements, taken with a monocular camera, as a viable aid to inertial sensors, in order to provide automated navigation comparable to modern GPS precision.

1.1 History

Since the inception of the heavier-than-air aircraft in 1903, methods and tools for navigation have evolved tremendously. Arthur Hughes, the author of *History of Air*

Navigation [6], stated, “in the first twenty years of flying, men were equal to, or better than, the machine”. Navigation tools were not available and the ability to navigate was dependent on the skill and instinct of the pilot. This section provides the historical background of a few of the early navigation methods that are related to the development of this modern application of the driftmeter concept fused with inertial navigation.

1.1.1 Air Pilotage.

Air pilotage, or piloting, is the method of directing an aircraft from place to place by referring to visible landmarks on Earth’s surface, such as light-beacons, landmarks, railroads, rivers, mountains, or lakes, with the use of a map and dead reckoning [7]. Dead reckoning, in the context of pilotage, combines the knowledge of the aircraft’s position over visible landmarks with map readings and the measured time between the landmarks to determine ground speed, estimated time of arrival, required heading changes, and/or wind speed and direction. There are many limitations to navigating solely on pilotage. The most obvious being that it requires an accurate land map and ideal conditions of flight. For instance, the weather must be clear and the aircraft must be flying low enough so that the landmarks can be seen.

1.1.2 Driftmeter.

The driftmeter was one of the earliest instruments developed to determine the effect of wind on the direction of flight and the ground speed of an aircraft. A dedicated navigator used information from an altimeter and an airspeed indicator along with bearing measurements of ground features to calculate the ground speed and the directional drift caused by wind vectors on his aircraft during flight. The bearing measurements were determined by visibly tracking stationary objects on the ground or whitecaps on the water surface [7]. The drift meter was installed so that a zero degree line was parallel to the longitudinal axis of the aircraft and the navigator would have an unobstructed view downward through a glass plate in the floor of the aircraft. The track arm could be rotated

so that objects on the ground appear to travel along the horizontal drift line. The amount that the horizontal drift line rotated from the zero degree line would indicate the drift angle.

The Pioneer Speed and Drift Indicator was one of these devices [8]. It is illustrated graphically in Figure 1.1 and can be viewed online at the Smithsonian "Time and Navigation" webpage [9]. It had a pivoting eye piece for the navigator to look through, which was mounted on an arm that established a set distance between the navigator's eye and the horizontal drift line. (The set distance between the eye piece and the horizontal drift line can be compared to the focal distance of a camera.) The horizontal drift line had two sets of cross wires that the navigator used to initiate and stop a timer as a ground object crossed under. The ground speed of the aircraft was then determined by dividing the altitude of the airplane above the ground by the time required for the ground feature to pass from one cross wire to the next. While navigation measurements were being made, the aircraft would have to be flown straight and level.

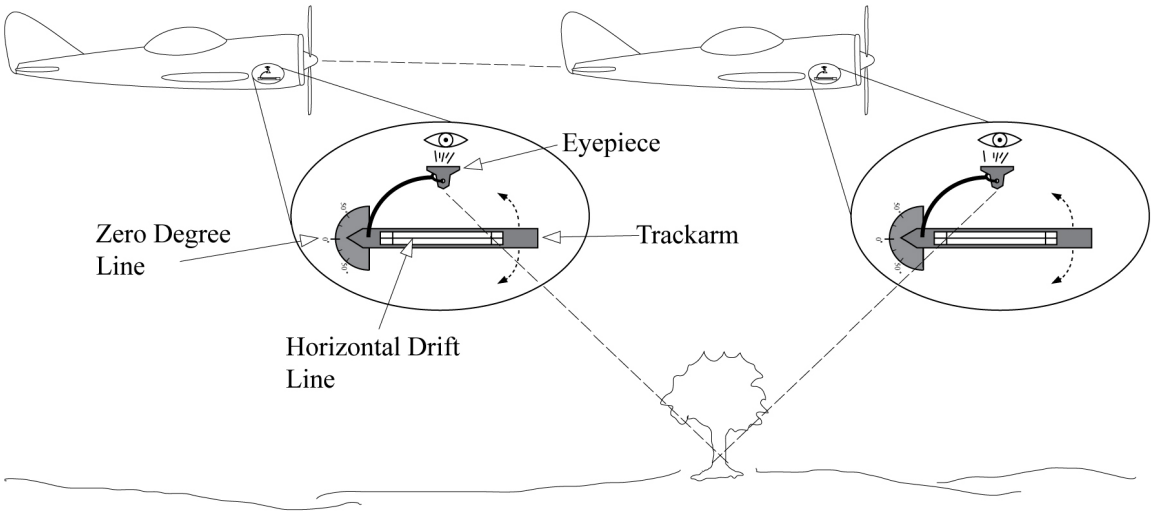

Figure 1.1: Pioneer Drift Meter

A more advanced driftmeter, named the B-3, was manufactured by the Eclipse-Pioneer Division of the Bendix Aviation Corp., and was standard equipment on Air Force and transoceanic aircraft [7] through the World War II and early Cold War eras [10]. It was stabilized by a gyroscope, which allowed the set of reference timing lines to remain horizontal at all times, regardless of turbulence and within 20 degrees of roll, pitch, and yaw of the aircraft. It had two different eye pieces, which allowed for viewing ground features at different elevations: one for normal sight and one for three times magnification.

The drift meter was a proven tool for determining the drift angle, wind speed, and ground speed of an aircraft by tracking the bearing angle of distinct ground features. It was utilized over land with stationary features such as houses, roads, trees, and rivers. It was also used for transoceanic flights where the navigator utilized whitecaps as a reference point. Although the driftmeter improved navigation compared to the method of air pilotage, it also shared several similar shortcomings which greatly limited navigation. It required flight conditions to be ideal in order to view ground objects, which limited the altitude of flight and flight through or above cloud formations. Perhaps the greatest of its shortcoming was the accrued error, because the navigator was not physically capable of continuously monitoring changes in flight conditions (altitude, airspeed, etc.).

1.1.3 Inertial Navigation.

The ability to determine position, velocity, and attitude through the use of inertial sensors revolutionized navigation. This was first demonstrated by the Germans during World War II aboard the V-2 ballistic missile and further developed in the United States in the late 1940s and early 1950s by the MIT Instrumentation Laboratory, Northrop, and the Autonetics division of North American Aviation, under Air Force sponsorship [11]. By integrating a body's acceleration and angular rotation rate, the position, velocity, and attitude could be determined.

Inertial navigation systems (INS) have remained a vital tool in modern navigation. Reference [12] states that INSs are special because they are "self-contained: they are independent of weather conditions and are operable anywhere in seas, underwater, lands, tunnels, or in air." The self-contained nature of INS is the result of employing six inertial sensors. Three orthogonally mounted accelerometers are used to detect the three-dimensional specific forces acting on the body and three gyroscopes are used to establish the spatial attitude in a three-dimensional Cartesian coordinate frame [13]. The quality of these inertial sensors directly reflects the precision and performance of the INS.

INS's have been, and continue to be, used in a variety of applications. They can be found on ships, aircraft, submarines, guided missiles, spacecraft, and, to some extent, modern automobiles, where each specific application requires different levels of precision. Grewal [14] defined general usage categories as strategic (very high performance navigation), navigational (medium-accuracy navigation), tactical (low-accuracy navigation), or consumer (non-navigational applications). The performance of the INS is characterized by the quality of the inertial sensors, because their measurements are integrated over time to determine the INS output. Therefore, the integration of small accelerometer and gyroscope errors over time cause navigation precision to deteriorate over time. Consequently, the quality of the inertial sensors determines how long the navigation information can be trusted and, like anything else, the price generally determines their quality.

1.1.4 Satellite Based Navigation.

The first fully operational satellite-based navigation system was the U.S. Navy's system known as Transit, which was developed and implemented from the early to mid-1960's [15]. Each satellite was a self-contained navigation beacon. It was designed to update dead reckoning navigational information from an INS aboard the Polaris submarines, where the position updates were done at intervals of more than an hour. Since

Transit was designed primarily for oceanic vessels, accuracy was degraded for aircraft or users on land by uncertainties in their altitude and their velocity.

The second operational navigation satellite system, Cicada, was developed by Russia in response to the Cold War. It was similar in design to Transit and primarily used for ship navigation [15]. Two more satellite navigation programs were established and began development in the mid 1960's: "621B" by the Air Force Space and Missile Organization (SAMSO) and "Timation" by the Naval Research Laboratory (NRL) [15].

"In 1968, the Joint Chiefs of Staff (JCS) issued new requirements for precisely locating military forces worldwide" [15]. The most stringent of these requirements were for aircraft, which became the driving parameters for a newly established DOD Navigation Satellite Executive Steering Group (NAVSEG). This group commissioned a number of comparative studies and evaluated three US satellite navigation systems, ultimately leading to the GPS program.

Since the first launch of an operational GPS satellite in 1978 [15], GPS has become the benchmark for precision navigation. It requires that a minimum of four satellites are visible to the user to determine his or her position. The orbital configuration utilized a total of 24 satellites in 6 different orbits, providing a minimum of six satellites in view at any time. Unlike the previous satellite navigation systems, it provided continuous three-dimensional positioning needed for aircraft. The military and civilian applications are countless.

At the time [15] was written, the Standard Positioning Service (SPS) provided to civilian users was 6 [m] accuracy and the Precise Positioning Service (PPS) provided to military users was 2.3 [m] accuracy. Because of the error accumulation over time associated with INS, GPS better satisfied the requirements set for a precise navigation system. However, low power signals transmitted from the satellites require that the user's antenna have a direct Line of Sight (LOS) with at least four satellites. This prevents usage

indoors and limits usage in urban canyons. GPS is also vulnerable to attack or disruption, such as jamming or spoofing [16].

1.2 Motivation

Advancements in computer technology over the past few decades has drastically increased data processing speeds and thus improved the usage of recursive algorithms like the Kalman filter, introduced in 1960 [2]. The Kalman filter algorithm has been used to merge inertial navigational data from Inertial Measurement Units (IMU) with position data from GPS receivers to create an accurate passive navigation solution. Passive navigation systems are required for military applications because they do not transmit signals out for the purpose of navigating; therefore, they are not easily detected. Active navigation tools using radar are less desirable in combat environments.

The performance of an INS is characterized by the drift of the accelerometers and gyroscopes discussed in section 1.1.3. The INS accuracy can be improved through the use of more accurate sensors; however, the cost of these sensors quickly escalates. An alternative approach, referred to as integrated navigation [17], utilizes an additional navigation source along with a Kalman filter algorithm to aid the INS and significantly reduce its drift over time. When this technique is employed, the INS is allowed to drift without influence from the additional navigational source. The Kalman filter utilizes the measurements from the additional navigation source and estimates the drift error of the INS, which is then subtracted from the output of the INS to improve navigation performance. The INS without any aiding is referred to as the"Free INS".

The work presented in this thesis is motivated by the possibilities of aiding a navigation-grade INS with an optical sensor, acting as a automated driftmeter, to achieve precision results similar to GPS. Therefore, it provides an alternative passive navigation system for military aircraft applications. A three-dimensional measurement equation will be utilized in this work that blends optical sensor data of tracked ground features with

output INS data. This will be done on the principles of the method developed by Pachter and Relyea [18] [3].

Much research has been accomplished in recent years on a process known as Simultaneous Localization and Mapping (SLAM) [19], which is the process of jointly establishing an aircraft's ownship position and geolocating ground features. For this particular work, geolocation is the act of acquiring stationary ground features to establish reference points, whose bearings will be measured over time. These measurements will be used to aid the INS in order to improve the aircraft's position estimate. This particular method of SLAM is herein referred to as "bootstrapping". First, the aircraft's somewhat inaccurate position and bearing measurement are used to geolocate a ground feature. Then, the bearing measurements of the said ground feature taken over time are used to aid the aircraft's INS in order to improve the aircrafts's position estimate. These steps are taken in the same way as a man is able to "pull himself out" of quicksand by his own bootstraps.

The advantage of this method of SLAM is that it allows for navigation without a strict, predefined map or a priori information of ground features. The disadvantage is that the aircraft's position uncertainty increases with time. However, while a ground feature is being tracked over time, its position uncertainty does not increase. It remains the same from the moment of geolocating that ground feature. Thus, an improved navigation system, comparable to GPS, is provided.

Image processing associated with the geolocation and tracking of ground features from raw optical sensor data is still a developing field. The aircraft navigators of the early 1900's had the God given ability of discernment and reason as they selected stationary ground features to track while operating the driftmeter. This is not an easy task for a computer, which must scan a two-dimensional pixel representation of a three-dimensional

world in order to detect the best features to track and flawlessly perform the image registration task as it moves from frame to frame.

Two algorithms currently used are Scale Invariant Feature Transform (SIFT) and Speeded Up Robust Features (SURF) [20], [21]. One of the most challenging tasks is the process of determining the slant range to a specific ground feature while the terrain elevation is changing. The absolute altitude was used for calculating the ground speed while using the driftmeter [7]. The absolute altitude, while flying over land, was determined by subtracting the terrain elevation from the altitude measurement provided by an altimeter.

Advantages of the automated feature tracking algorithm are that it would have the ability to track more than one ground feature at a time and it would be able to continuously track and update the INS at increments much smaller than humanly possible. The navigator of the past would only periodically track features in order to determine ground speed for dead-reckoning, creating accumulated error throughout the flight.

1.3 Scope and Assumptions

There are very few things that are definite in this world. Even as you read these words, you may be very confident in your position of where you are sitting and confident in the distance of stationary objects around you, but your exact position is only stationary relative to Earth. Calculating your position or distance from stellar objects, not rotating with the Earth, is much more difficult. Moreover, there is a certain amount of doubt in your position. This doubt or uncertainty is quantified by the term covariance, from statistics.

The contribution of this research is the calculation of the covariance associated with geolocating a ground feature and then tracking that feature until it disappears from the field of view (FOV) of the camera, whereupon is replaced by a newly geolocated ground feature. This process has been accomplished by other research, but not in the particular manner, involving bearing measurements, presented in this research.

To evaluate the possible contributions of bearing measurements as a viable aid to an INS, a plausible navigation scenario is established. The scope of this research focuses on the navigation contribution of SLAM. Consequently, assumptions are made in the scenario which improve the focus of this research. The greatest of these assumptions is that stationary ground features may be detected and tracked as pixel representations by a real-time image processing algorithm. The next is that two distinct ground features are available for each image frame throughout the navigation scenario and their elevation is known to be zero. Involving the navigation environment, it is assumed that the aircraft is nominally flying straight and level at a constant ground speed over a flat and non-rotating Earth.

The critical image registration issue associated with image processing is outside the scope of this research and will not be addressed. It is fair to assume that ground features may be detected and tracked as pixel representations, because current image processing algorithms identify features as pixel locations on a coordinate system relative to each image frame [16]. However, it was stated in 2008 that a "great leap in feature generation/tracking technology and significantly more precise optics" are required for the development of a viable vision based navigation platform [19].

The assumption that two distinct ground features are available does not imply that these features are known. When utilizing the navigation method of pilotage the ground features were associated with maps that identified specific, known feature locations. This research considers features which are measured with an uncertainty (covariance) relative to the quality (resolution) of the optical sensor. However, their locations are not known. The assumption that the ground feature elevations are known/zero is fair because generally ground feature heights are relatively small in comparison with the elevation of aircraft flying overhead.

To ensure a proper evaluation of the benefit of bearings tracking to aid an INS, the calculations of this navigation scenario are justifiably simplified, with the assumption of a flat and non-rotating Earth. By simplifying these parameters, the flight dynamics are simplified. Furthermore, the development of errors from the Free INS and the Kalman filter's estimate of those errors are more easily compared with the truth data in the simulations.

1.4 Related Research

This section presents modern research in the field of navigation by use of optical sensors. It presents their research task along with the specifications of equipment used. Finally, their achieved navigation precision and the research's limitations are presented.

1.4.1 Binocular Feature Tracking Fused with Inertial Measurements.

Veth's AFIT PhD dissertation in 2005 was inspired by the precision navigation capabilities of animals/biometrics [16]. It claimed that "there exists a natural synergy between imaging and inertial systems" [16]. Veth performed indoor measurements and outdoor flight test with two identical monochrome digital cameras, a consumer-grade strapdown IMU, and a tactical-grade strapdown IMU. His system was configured such that both IMUs would record measurements simultaneously. This configuration insured the same dynamics for both grades of IMUs and thus fair testing between the two. The specifications for his two IMUs are listed in Table 1.1.

The cameras had a 1280×1024 (1.3 megapixel (MP)) resolution. They were rigidly mounted with space between them, allowing distance for triangulation for range calculations of the features. They had a measurement rate of three frames per second at full resolution. The camera data was processed using the SIFT algorithm, which determined features in each frame and tracked them according to their pixel location.

Table 1.1: Veth's Inertial Measurement Sensor Specifications for the Crista consumer-grade IMU and the Honeywell HG1700 tactical-grade IMU. Veth estimated the parameters with an asterisk since they were not included in manufacturer specification data [16].

Parameter	UNITS	Crista IMU	HG1700
Sampling interval	ms	5.0	10.0
Gyro bias sigma	deg/hr	1800	1.0
Gyro bias time constant	hr	2*	2*
Angular random walk	deg/ $\sqrt{hr}$	2.23	0.3
Gyro scalefactor sigma	PPM	10000	150
Accel bias sigma	m/s^2	0.196	0.0098
Accel bias time constant	hr	2*	2*
Velocity random walk	m/s / $\sqrt{hr}$	0.261	0.57*
Accel scalefactor sigma	PPM	10000	300

An extended Kalman filter was used to aid the SIFT algorithm according to matched estimations of propagated feature locations, determining whether they were good or bad features. As new features were determined to be stronger, they replaced weaker ones. His algorithm assumed that the navigation state errors and the landmark errors were independent. His system "learned" its environment by maintaining a database of the tracked features and position estimates.

Veth obtained meter level position precision in the indoor environment, but the flight test results were non-conclusive, because the test lacked a faithful truth source. Ultimately, his work proved that a combination of optical data and inertial data can provide precision navigation capabilities equivalent to GPS, while utilizing binocular measurement geometry to determine the LOS range of tracked features.

1.4.2 Covariance Analysis of Vision Aided Navigation by Bootstrapping.

Relyea's AFIT Master's thesis in 2012 followed the work of Guner Mutlu, a previous AFIT student under the guidance of Dr. Meir Pachter [3]. Relyea further developed the calculations for bearing measurements of ground features from a single/monocular camera, ultimately used in this current work. He also developed the simplified flight dynamics, used herein, where he applied the camera measurements to a Free INS and performed covariance analysis. His Free INS specifications were calculated based on $1\frac{km}{hr}$ propagated sensor bias errors, which qualifies it as a navigation-grade INS. The accuracy of his camera bearing measurements was based on an assumption of a 9 MP camera with an aspect ratio of one. His non-dimensional INS specifications are listed in Table 1.2.

Table 1.2: Relyea's calculated 1-σ inertial sensor specifications provided a variance of $1\frac{km}{hr}$ drift error due to the influence of biases. These values are non-dimensional according to his navigation scenario [3].

Parameter	UNITS	1 km/hr
Sampling interval	ms	10
Gyro bias sigma	Non-Dim	1.0912×10^{-5}
Accel bias sigma	Non-Dim	9.0935×10^{-8}

His camera only tracked two ground features at a time, and he started the navigation scenario with two "known" ground features and progressed until he only tracked "unknown" features. The covariance of newly tracked ground feature's (x and y) position was determined by adding the covariance of the navigation state error (x and y) position, at the time of geolocating the new ground feature, with the covariance of the camera measurement.

The resulting standard deviations of his covariance analysis are provided in Table 1.3. Relyea's 1-σ standard deviation achieved meter level precision with the simulated flight of one hour, while utilizing INS specifications equivalent to a navigation-grade INS.

However, he only used INS sensor bias in his system – not process noise, a.k.a sensor drift. Also, he only evaluated the overall system covariance – not the aided results.

Table 1.3: Relyea's covariance analysis results of one hour simulated flight [3].

Std Dev	Unaided Final Value	Aided Peak Value	Aided Final Value
σ_x	1 km	4.7 m	4.7 m
σ_y	1 km	4.0 m	4.0 m
σ_z	0.7071 km	0.10 m	0.0389 m
σ_{v_x}	7×10^{-3} m/s	8.21×10^{-5} m/s	3.93×10^{-5} m/s
σ_{v_y}	7×10^{-3} m/s	3.06×10^{-5} m/s	2.29×10^{-5} m/s
σ_{v_z}	4×10^{-3} m/s	3.9×10^{-5} m/s	2.16×10^{-7} m/s
σ_ϕ	3.27×10^{-5} rad	2.40×10^{-6} rad	1.07×10^{-7} rad
σ_θ	3.27×10^{-5} rad	3.16×10^{-6} rad	2.39×10^{-7} rad
σ_ψ	3.27×10^{-5} rad	2.23×10^{-5} rad	2.23×10^{-5} rad

1.4.3 Inertial Navigation System Aiding Using Vision.

Quarmyne's AFIT Master's thesis in 2013 followed the work of Relyea [4]. His goal was to apply a linear Kalman filter to the covariance analysis of the previously developed three-dimensional flight simulation. The camera resolution and inertial sensor specifications were the same as those of Relyea with only bias errors applied to the Free INS.

Quarmyne also began his navigation scenario with two "known" ground features and progressed until he only tracked "unknown" features. However, advancements were made in his research with derivations of newly tracked ground feature's geolocation and associated error covariance by using the corrected (aided) measurement equation. This method is further developed in this current research.

The standard deviations derived from the covariance of his Kalman filter final values are presented in Table 1.4. Quarmyne's Kalman filter estimated the error of the Free INS. By correcting that error, an improvement of one order of magnitude was achieved.

Table 1.4: Qyarmyne's Kalman filter results after one hour of simulated flight. The "Unaided Final Values" are the results of his Free INS and the "Aided Peak Values" are the results of subtracting the KF estimated values from the corresponding Free INS values [4].

Std Dev	Unaided Final Value	Aided Final Value
σ_x	6.56 km	692.72 m
σ_y	6.56 km	18.84 m
σ_z	0.707 km	5.72 m
σ_{v_x}	3.67×10^{-2} m/s	5.74×10^{-3} m/s
σ_{v_y}	3.67×10^{-2} m/s	8.66×10^{-5} m/s
σ_{v_z}	3.93×10^{-3} m/s	3.18×10^{-5} m/s
σ_ϕ	1.05×10^{-4} rad	1.09×10^{-5} rad
σ_θ	1.05×10^{-4} rad	3.27×10^{-5} rad
σ_ψ	1.05×10^{-4} rad	5.85×10^{-5} rad

1.5 Approach/Methodology

The current research follows the work of Quarmyne and utilizes the same flight dynamics for a one hour flight. The tactical-grade Free INS specifications are developed with both sensor bias and sensor drift errors, equally responsible for $1\frac{km}{hr}$ navigation error. The automated driftmeter measurement equations are borrowed from the work of Relyea and utilize a downward facing monocular camera for optical measurements. A recursive linear Kalman filter algorithm utilizes Free INS measurements and automated driftmeter

measurements to determine an optimal estimate of the Free INS error. The estimate is then subtracted from the Free INS output, providing an improved navigation state.

Prior to the beginning of the navigation scenario, flight conditions include an elevation of 1000 [m] flying straight and level over a flat non-rotating Earth, where a GPS aided INS provides precise position data. At the beginning of the navigation scenario, GPS is no longer available, the INS is perfectly aligned, and two "unknown" ground features are geolocated. During the geolocation of all newly tracked ground features, their associated geolocation error estimate is set equal to zero, because it will on average be zero. Their covariance is derived from the improved navigation state error covariance plus the camera measurement covariance.

1.6 Thesis Organization

Chapter 1 discusses the viability of vision/bearing measurements as an aid for inertial sensors and then follows up with the current state of related research. Chapter 2 provides the mathematical concepts needed for the development of the modern driftmeter system. Chapter 3 introduces the methodology used to simulate the system. Chapter 4 discusses and analyzes the results of the simulations. Chapter 5 provides conclusions from the research and details possible future work.

II. Mathematical Background

This chapter describes the mathematics and physics required to understand inertial navigation, Kalman filtering, and bearings-only ground feature tracking. The three reference frames used in this work are presented, followed up by the calculations required to transition between them. The concepts of a strapdown INS, as used in this work, are presented. Design considerations and the equations for linear Kalman filtering are presented. Lastly, the optics model and required calculations for bearings-only tracking are presented. The bulk of this discussion is drawn from the work of Titterton and Weston on strapdown inertial navigation [17], Maybeck on Kalman filter design [1] with the use of Brown and Hwang's Kalman filtering equation notations [2], and Relyea on bearing feature tracking [3].

2.1 Reference Frames

For navigation over the Earth, it is necessary to define a convenient set of axes. The inertial frame, Earth frame, navigation frame, wander azimuth frame, and the body frame are the co-ordinate frames described in [17]. For this research, the two frames of concern are the navigation frame and the body frame. The focal frame is also introduced as a concept, but is not of major concern because it is perfectly aligned with the body frame.

2.1.1 Navigation reference frame.

The navigation frame is a local geographic frame, which has its origin placed at the position of the aircraft near the surface of the Earth (at the location of the INS) [17]. The x_n-y_n plane is tangent to the surface of the Earth, with the positive x_n-axis pointing true North, the positive y_n-axis pointing East, and the positive z_n-axis pointing down, toward the center of the Earth. This is referred to as the North-East-Down (NED) axes convention. See Figure 2.1 for an illustration of the navigation reference frame.

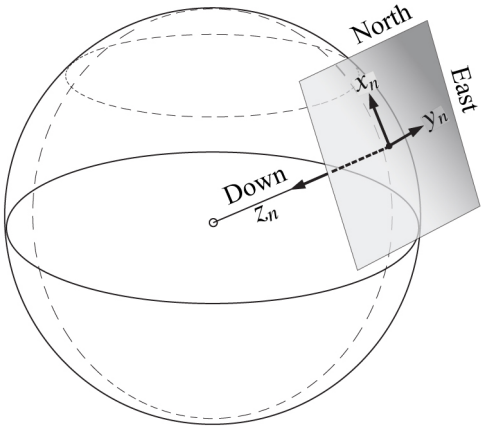

Figure 2.1: Navigation reference frame

2.1.2 Body-fixed reference frame.

The body frame is affixed to the aircraft, where the origin is commonly located at the aircraft's center of gravity. The axes of the frame have the same rotational motion as the body does. The positive x_b-axis points out of the nose of the aircraft creating the roll axis, the positive y_b-axis points out the starboard (right) wing creating the pitch axis, and the z_b-axis points out the bottom of the aircraft, which creates the yaw axis. See Figure 2.2 for an illustration of the aircraft body frame.

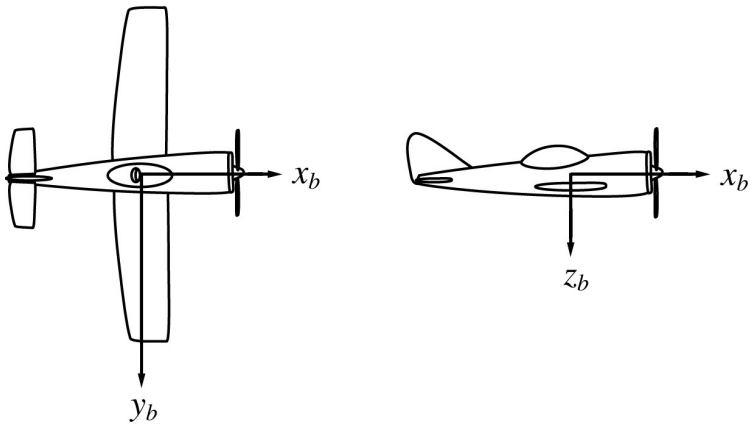

Figure 2.2: Aircraft body frame

2.1.3 Camera-focal reference frame.

The focal frame is rigidly attached to the camera, with its origin at the camera's optical center [16]. The x_f and y_f axes point up and to the right, respectively, while the z_f axis is perpendicular to the focal plane, as shown in Figure 2.3.

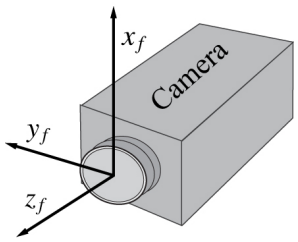

Figure 2.3: Camera focal frame

The focal plane is best represented as an array of pixels with a physical height of H and width of W [16]. The aspect ratio is determined by dividing the H by W. For this research, the FOV captured in this array is square and thus the aspect ratio is equal to one. The camera is facing downward and co-located with the INS; hence, the x_f axis is aligned with the x_b axis and y_f axis is aligned with y_b axis. The number of pixels determines the image resolution, which determines the variance of the camera measurements.

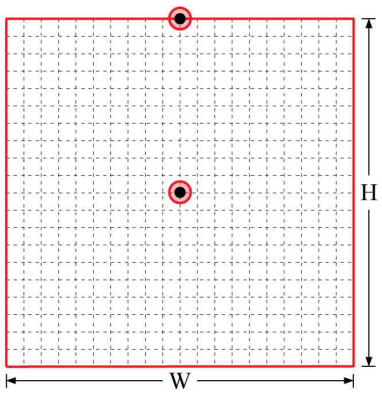

Figure 2.4: Camera focal plane represented as a pixel array

2.2 Coordinate System Transformation

This section develops the mathematics needed to transition navigation vectors from one coordinate frame to another. Reference [17] is primarily used for this introduction of Euler rotation angles and the direction cosine matrix (DCM). Although there are other methods of coordinate transformation, this method is preferred when dealing with a stable platform INS.

The three orthogonal gyroscopes described in Section 1.1.3 measure the rotation rate about the three body frame axes. The corresponding body angles are referred to as the Euler rotation angles. Using the Euler angles, transformation from the body frame to the navigation frame can be carried out as three successive rotations about the three body frame axes as follows [17]:

$$\text{rotation } \psi \text{ about } z_b\text{-axis}, \quad \mathbf{C}_1 = \begin{bmatrix} \cos\psi & -\sin\psi & 0 \\ \sin\psi & \cos\psi & 0 \\ 0 & 0 & 1 \end{bmatrix}$$

$$\text{rotation } \theta \text{ about } y_b\text{-axis}, \quad \mathbf{C}_2 = \begin{bmatrix} \cos\theta & 0 & \sin\theta \\ 0 & 1 & 0 \\ -\sin\theta & 0 & \cos\theta \end{bmatrix}$$

$$\text{rotation } \phi \text{ about } x_b\text{-axis}, \quad \mathbf{C}_3 = \begin{bmatrix} 1 & 0 & 0 \\ 0 & \cos\phi & -\sin\phi \\ 0 & \sin\phi & \cos\phi \end{bmatrix}$$

Thus, the transformation from the body frame to the navigation frame may be expressed as the product of these three separate transformations as follows [17]:

$$\mathbf{C}_b^n = \mathbf{C}_1 \cdot \mathbf{C}_2 \cdot \mathbf{C}_3$$

where $\mathbf{C}_b^n$ is the DCM specifically for the transformation from the body frame to the navigation frame. The resultant product is as follows:

$$\mathbf{C}_b^n = \begin{bmatrix} \cos\theta \cdot \cos\psi & \begin{matrix} -\cos\phi \cdot \sin\psi \\ +\sin\phi \cdot \sin\theta \cdot \cos\psi \end{matrix} & \begin{matrix} \sin\phi \cdot \sin\psi \\ +\cos\phi \cdot \sin\theta \cdot \cos\psi \end{matrix} \\ \cos\theta \cdot \sin\psi & \begin{matrix} \cos\ \phi \cdot \cos\psi \\ +\sin\phi \cdot \sin\theta \cdot \sin\psi \end{matrix} & \begin{matrix} -\sin\phi \cdot \cos\psi \\ +\cos\phi \cdot \sin\theta \cdot \sin\psi \end{matrix} \\ -\sin\theta & \sin\theta \cdot \cos\theta & \cos\phi \cdot \cos\theta \end{bmatrix} \tag{2.1}$$

According to [17], when considering small angle rotations, valid in this research, the body to navigation frame transformation DCM is further simplified as follows:

$$\begin{aligned} \sin\phi &\rightarrow \phi & \cos\phi &\rightarrow 1 \\ \sin\theta &\rightarrow \theta & \cos\theta &\rightarrow 1 \\ \sin\psi &\rightarrow \psi & \cos\psi &\rightarrow 1 \end{aligned}$$

Therefore, making these substitutions in (2.1) and ignoring products of small angles, the DCM expressed in Euler rotations reduces approximately to the skew symmetric form of C_b^n as follows:

$$\mathbf{C}_b^n = \begin{bmatrix} 1 & -\psi & \theta \\ \psi & 1 & -\phi \\ -\theta & \phi & 1 \end{bmatrix} \tag{2.2}$$

If transformation from the navigation frame to the body frame is desired, then C_b^n would be calculated as follows

$$\mathbf{C}_n^b = \mathbf{C}_b^{n^T} = \mathbf{C}_3^T \cdot \mathbf{C}_2^T \cdot \mathbf{C}_1^T$$

where the superscript ^{T} indicates that it is the transpose of the matrix being evaluated. Applying the transpose and the small angle rotations provides the DCM for transforming from the navigation to the body frame, as follows:

$$\mathbf{C}_n^b = \begin{bmatrix} 1 & \psi & -\theta \\ -\psi & 1 & \phi \\ \theta & -\phi & 1 \end{bmatrix} \tag{2.3}$$

Due to the placement of the camera, the focal frame is perfectly aligned with the body frame, so the transformation is simply $\mathbf{C}_f^b = \mathbf{I}$.

2.3 Strapdown INS

This section presents fundamental information pertaining to the understanding of the INS utilized in this research. Original applications of inertial navigation technology used stable platform techniques [17]. These systems isolated the rotational motion of the vehicle by mounting the inertial sensors on a stable platform. Modern systems, including the system used in this research, have removed the mechanical complexity of stable platform systems by rigidly mounting or "strapping down" the inertial sensors directly to the body of the aircraft. These systems have decreased both cost and size and have greater reliability. However, they demand increased computational complexity and the gyros must have an expanded dynamics range. Fortunately, both of these concerns are easily satisfied with today's ring laser gyro (RLG) or fiber optic gyroscope (FOG) technology.

2.3.1 Specific Force Model.

The strapdown INS utilizes three orthogonally mounted accelerometers whose input axes are aligned with the body axes. This determines the specific force applied to the body in three dimensions. The measured components of specific force and estimate of gravity are summed to determine components of acceleration with respect to the navigation frame. The summed value is then integrated once to determine the velocity of the body and a second time to determine the position of the body relative to the navigation frame.

The acceleration components $a^{(n)}$ of the aircraft body in the navigation frame is mathematically represented, as follows:

$$\mathbf{a}^{(n)} = \frac{d^2\mathbf{r}^{(n)}}{dt^2} \tag{2.4}$$

where $\mathbf{r}$ is the vector which describes the three dimensional position of the body in the navigation frame. Each accelerometer contributes to the specific force vector $\mathbf{f}^{(n)}$, which is

described mathematically as a perfect sensor with no errors, as follows

$$\mathbf{f}^{(n)} = \mathbf{a}^{(n)} - \mathbf{g}^{(n)}$$

where $g^{(n)}$ is the specific force due to gravity. During constant altitude and wings level flight, $f_x^{(n)} = a$, $f_y^{(n)} = 0$, and $f_z^{(n)} = g$, where g is the acceleration of gravity and a is the longitudinal acceleration of the aircraft [3]. Thus,

$$\mathbf{f}^{(n)} = \begin{bmatrix} a \\ 0 \\ 0 \end{bmatrix} - \begin{bmatrix} 0 \\ 0 \\ -g \end{bmatrix} = \begin{bmatrix} a \\ 0 \\ g \end{bmatrix}$$

and the skew symmetric [13] matrix form of the vector is defined by $\mathbf{f}^{(n)}\times$:

$$\mathbf{f}^{(n)}\times = \mathbf{F}^{(n)}$$

$$\mathbf{F}^{(n)} = \begin{bmatrix} 0 & -g & 0 \\ g & 0 & -a \\ 0 & a & 0 \end{bmatrix} \tag{2.5}$$

The skew symmetric matrix of the specific force vector is used in the development of the INS error equations.

2.3.2 Imperfect Sensors.

The reality of the accelerometers and gyroscopes is that they provide imperfect representations of the true specific force and true body rotation rate information. The two dominant sources of error are described as sensor bias and sensor random-walk (drift). The sensor bias error is random on start-up but constant thereafter. A random-walk error is an accumulation of zero-mean random errors associated with "electronic noise from power supplies, intrinsic noise from semiconductor devices, or from quantization errors in digitization" [14]. This research analyzes the effect of modeling both of these errors separately, as well as combined.

2.3.3 Navigation State.

The navigation state vector, **x**, presented in [3] is used for this research. It is comprised of nine states, which describe the position, velocity, and attitude of the aircraft body in the navigation frame. The previously described imperfections from the sensor measurements contribute to the output of the INS and are described as the error states, $\delta\mathbf{x}$, of the INS. Therefore, the calculated (output) states of the INS are as follows:

$$\mathbf{x}_c = \mathbf{x} + \delta\mathbf{x}$$

The error states are the primary focus of this research, as the goal is to evaluate the contribution of an automated driftmeter's ability to help estimate these INS error states so they can be removed and thus provide an improved navigation state.

2.4 Kalman Filtering

This section provides some basic Kalman filter (KF) design considerations and the basic equations for the KF loop. Most information in this section will be drawn from [1] and [2]. Kalman filtering is a perfect match for the performance characteristics of a navigation-grade INS. INSs provide very good high frequency information. However, the long term, or low frequency, performance is poor [1]. All INSs have position errors that grow slowly with time, and ultimately these errors are unbounded. The KF utilizes the statistical characteristics of the errors in both the INS and the external source to optimally estimate the error from the INS. This is used to reduce error.

2.4.1 Kalman filter system design.

The KF design is determined by the application. Maybeck [1] stated that four design choices are available: "total state space" versus "error state space" formulation, and "feedforward" versus "feedback" mechanization. These design aspects are presented in Figure 2.5 with the aspects utilized in this research emphasized with a gray background. This is followed with a discussion of the advantages and disadvantages of each.

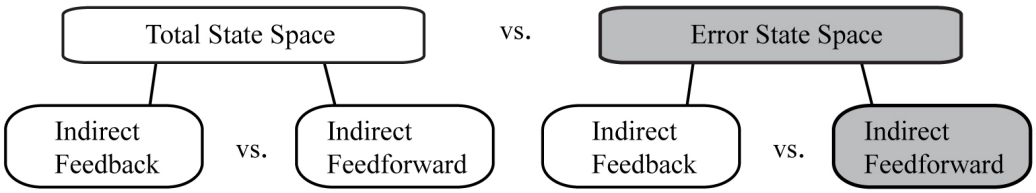

Figure 2.5: Kalman filter design aspects [1]

The “total state space” configuration integrates the KF inside the INS loop, where the accelerometers, gyroscopes, and external navigation measurements are the KF input and the navigation state information is the output. This provides “optimal time-varying gains,” thus improving the performance response time [1]. The major drawback is that it requires very high bandwidth, which creates a high computation burden. Another drawback is that the INS cannot operate without the filter. The risk of losing INS operation completely makes this a less desirable configuration.

The “error state space” KF is what is used in this current work. The inputs for this KF are the INS navigation states and the external navigation data, while the outputs are the navigation state error estimates. The KF dynamics are based on the INS error propagation equations, which for a navigation-grade INS are adequately represented as linear. The update rate can be much lower than the previously discussed configuration. Maybeck states that an effective sampling rate could be “on the order of half a minute”, because the Scheuler period is 84 minutes [1]. The configuration used in this research is a variation of this “error state space” KF, focusing solely on the error states of the INS and utilizing a sampling frequency of 1 second.

Furthermore, the “indirect feedforward” configuration is used in this work. The basic block diagram presented in [1] is illustrated in Figure 2.6. The KF compares the data from each navigational source and estimates the errors in the INS. These errors are then subtracted from the Free INS-provided navigation state, yielding an improved estimate of

the aircraft position, velocity, and attitude. In the event of KF or external navigation system failure, the Free INS data is still available; hence the advantage of this configuration. However, allowing the INS to drift with unbounded errors may compromise the validity of the linear error dynamics model, which is directly related to the KF performance.

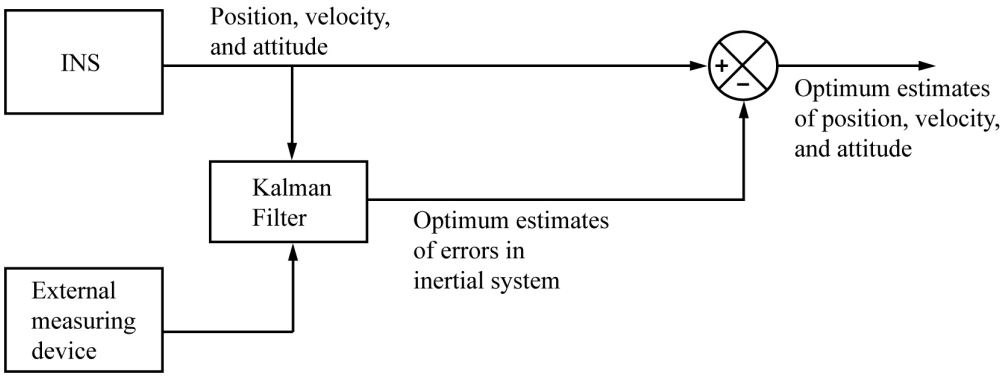

Figure 2.6: Indirect feedforward Kalman filter [1]

An alternative design is the "indirect feedback" configuration, illustrated in Figure 2.7. The KF estimates the INS errors, which are then fed back into the INS to reset it. This feedback action prevents the unbounded runaway of the INS error. Therefore, the "adequacy of a linear model is enhanced," improving KF performance [1]. Maybeck further stated that the "slow sample rate and the slow INS error dynamics" would allow for detection of filter or external aid failure and "the correction to the INS could be removed before much (any) performance deterioration were caused" [1]. This will be a design consideration for future work discussed in Chapter 5.

2.4.2 Continuous-Time Linear Stochastic System Model.

The continuous-time linear stochastic system model presented in [1] and [19] is

$$\dot{\mathbf{x}} = \mathbf{F} \cdot \mathbf{x} + \mathbf{B} \cdot \mathbf{u} + \mathbf{G} \cdot \dot{\mathbf{w}} \tag{2.6}$$

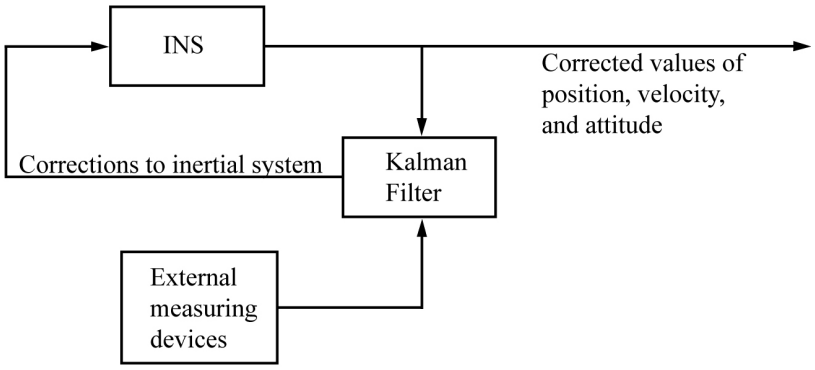

Figure 2.7: Indirect feedback Kalman filter [1]

where **x** is the state vector, **u** is a deterministic control input vector, **F** is the system dynamics matrix, **B** is a deterministic input matrix, **G** is the noise input matrix, and **w** is a vector of white, Gaussian, noise. **w** is described as a zero-mean Gaussian process with statistics, that follow:

$$\mathbf{E}\{\mathbf{w}(t) \cdot \mathbf{w}^T(t+\tau)\} = \mathbf{Q}(t) \cdot \delta(\tau)$$

where **Q** is the noise intensity, and $\delta(\tau)$ is the Dirac delta function.

The continuous-time linear error equation $\delta\dot{\mathbf{x}}$, presented in state space form by [3] and [4], is as follows:

$$\delta\dot{\mathbf{x}} = \mathbf{A} \cdot \delta\mathbf{x} + \mathbf{\Gamma} \cdot \delta\mathbf{u} \tag{2.7}$$

where $\delta\mathbf{x}$ is the navigation state error vector, $\delta\mathbf{u}$ is the random bias vector, **A** is the system error dynamics matrix, and $\mathbf{\Gamma}$ is the input matrix for the sensor bias terms. These error equations do not have a stochastic term. Therefore, they only model errors caused by the sensor biases, which are random on start-up but constant thereafter.

2.4.3 Linear Measurement Model.

The measurements **z** are provided to the KF in discrete time increments. The equation is presented in [1] as follows:

$$\mathbf{z}(t_i) = \mathbf{H}(t_i) \cdot \mathbf{x}(t_i) + \mathbf{v}(t_i)$$

where $\mathbf{z}(t_i)$ is a vector of measurements taken at time instant t_i. $\mathbf{H}(t_i)$ is the observation matrix, which relates the state values in $\mathbf{x}$ at time t_i to the measurement values in $\mathbf{z}$ produced by the sensor at time t_i. The covariance of the white Gaussian noise vector $\mathbf{v}$ is specified as follows:

$$\mathbf{E}\{\mathbf{v}(t_i) \cdot \mathbf{v}^T(t_j)\} = \mathbf{R}(t_i) \cdot \delta_{ij}$$

where $\mathbf{R}$ is the noise strength in the measurements $\mathbf{z}$ and δ_{ij} is a Kroeneker delta function [19].

2.4.4 Discrete-Time Linear Stochastic System Model.

The discrete-time linear stochastic system model is presented in [1] as follows:

$$\mathbf{x}(t_i) = \mathbf{\Phi}(t_i, t_{i-1}) \cdot \mathbf{x}(t_{i-1}) + \mathbf{B}_d(t_{i-1}) \cdot \mathbf{u}(t_{i-1}) + \mathbf{w}(t_{i-1}) \tag{2.8}$$

where the state vector $\mathbf{x}$ is calculated for time instant (t_i) with state transition matrix $\mathbf{\Phi}$ and discrete input matrix $\mathbf{B}_d$ plus white Gaussian noise at time instant (t_{i-1}). Reference [2] utilizes subscript $_k$ for the discrete time notation, so (2.8) would instead be presented as

$$\mathbf{x}_{k+1} = \mathbf{\Phi}_k \cdot \mathbf{x}_k + \mathbf{B}_{d_k} \cdot \mathbf{u}_k + \mathbf{w}_k \tag{2.9}$$

This discrete-time notation is adopted herein.

2.4.5 Discrete-Time Kalman Filter Loop.

The recursive equations for the discrete-time KF loop, as presented in [2], are illustrated in Figure 2.8. The recursive loop begins with an estimate of the initial conditions which are considered suboptimal and designated with a superscript minus sign. The Kalman gain is then calculated based on the initial covariance $\mathbf{P}_0^-$ and the measurement covariance $\mathbf{R}_k$. This gain value is then used to update (optimize) the initial conditions estimate with initial conditions of the external measurement $\mathbf{z_0}$. Since this is now an optimal estimate, it is used by the system and the associated covariance is calculated. The state transition matrix $\mathbf{\Phi}$ is then used to project ahead (propagate) what the estimated values of the navigation state error should be for the next instant in time,

$k + 1$. Thus, a suboptimal state estimate and an associated covariance are created. From this point, the recursive loop starts over by calculating the Kalman gain associated with the suboptimal estimates.

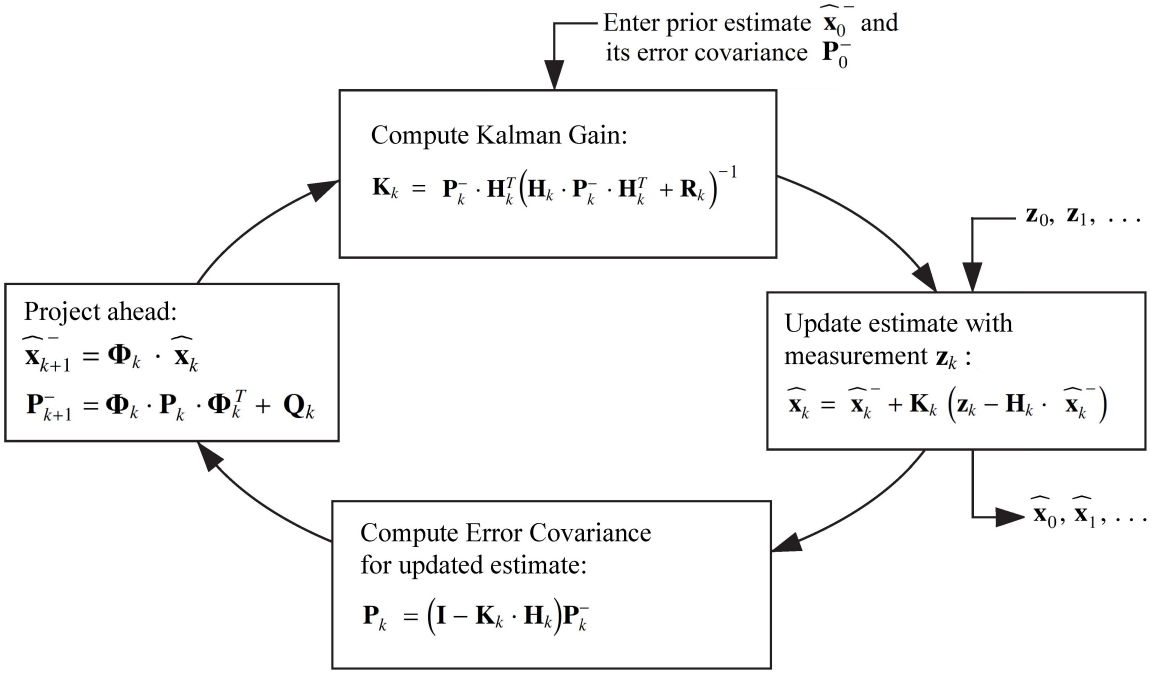

Figure 2.8: Linear Kalman Filter Recursive Loop [2]

2.5 Camera Model

This section introduces the optical sensor model. The ground feature is a pixel in the camera's focal plane. It explains the calculations of the ground feature's bearing measurements from the pixel's position in the camera's focal plane. The bearing measurements are used to develop the measurement equation for the Kalman filter and are borrowed from [5] and [3].

2.5.1 *Optical Sensor Model.*

The measurements that are used to aid the Free INS are from an optical sensor/camera located on the belly of an aircraft, co-located with the INS, and pointing downward in the same manner as a driftmeter. The optical sensor is modeled as a pinhole camera as in Figure 2.9, where all incoming light must pass through the optical center and is projected onto a focal plane located at distance f from the lens [16]. The focal distance from the lens to the focal plane is crucial to the calculations of ground speed in the same way it was used for the driftmeter in Section 1.1.2. A ground feature is acquired at the very edge of the camera's FOV and its centroid is represented in its focal plane as a single pixel. The pixel is tracked as it moves in the camera's focal plane and is used to determine the bearing of the ground feature.

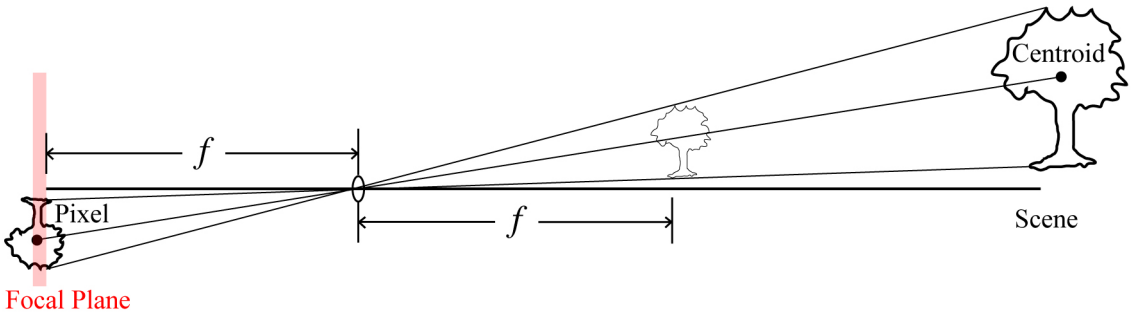

Figure 2.9: Pinhole camera model. The centroid of the ground features are tracked as a pixel representations in the focal plane.

2.5.2 *Bearing Measurements.*

The concept of bearing measurement tracking used as an automated driftmeter is presented in this section. This concept is first introduced from a two-dimensional perspective and then further explained for three dimensions. Finally, the equations used for the measurements input into the Kalman filter are presented.

A two dimensional representation of an aircraft flying along the x axis while tracking a single ground feature is illustrated in Figure 2.10. The ground feature's position is represented by x_p and the corresponding pixel location in the focal plane is represented as $x_{f\ell}$, where ℓ indicates a discrete time instant. The aircraft position relates to its horizontal distance d_ℓ from that ground feature at time ℓ. As the ground feature is tracked across the camera's FOV in the focal plane, pixel by pixel, the camera measures the ground feature's bearing angle.

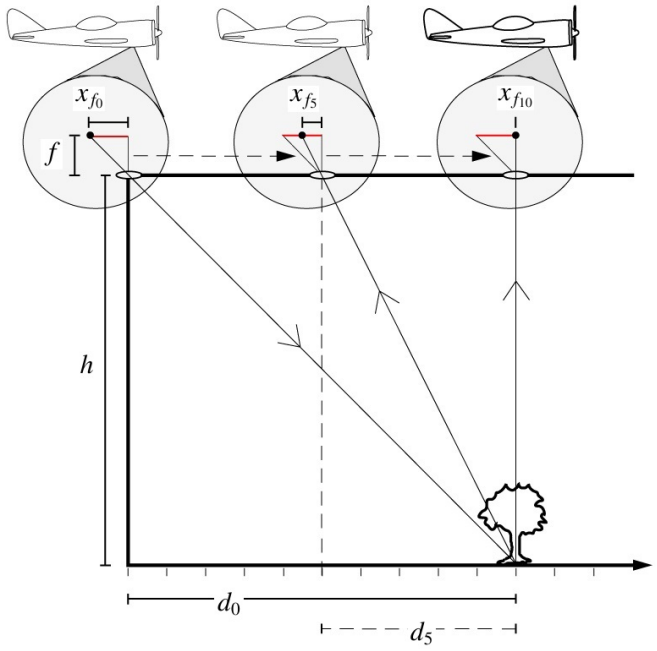

Figure 2.10: Two dimensional bearing measurement model

Consider the simplified two dimensional scenario where the aircraft's distance from the tracked ground feature is determined based on three factors: the "known" altitude h, the fact that pitch angle $\theta \equiv 0$, and the measured bearing angle. Thus, the camera provides a measurement d_ℓ of the aircraft's horizontal distance directly from the tracked ground

feature position x_p through the relationship that follows:

$$\frac{d_\ell}{h} = \frac{x_{f\ell}}{f} \tag{2.10}$$

where $x_{f\ell}$ is the location of the ground feature image in the focal plane of the camera.

Transitioning to the three dimensional scenario, Figure 2.11 illustrates that the camera's focal plane is placed a distance f in front of the camera. This is done in order to invert the image in the focal plane, simplifying the calculations.

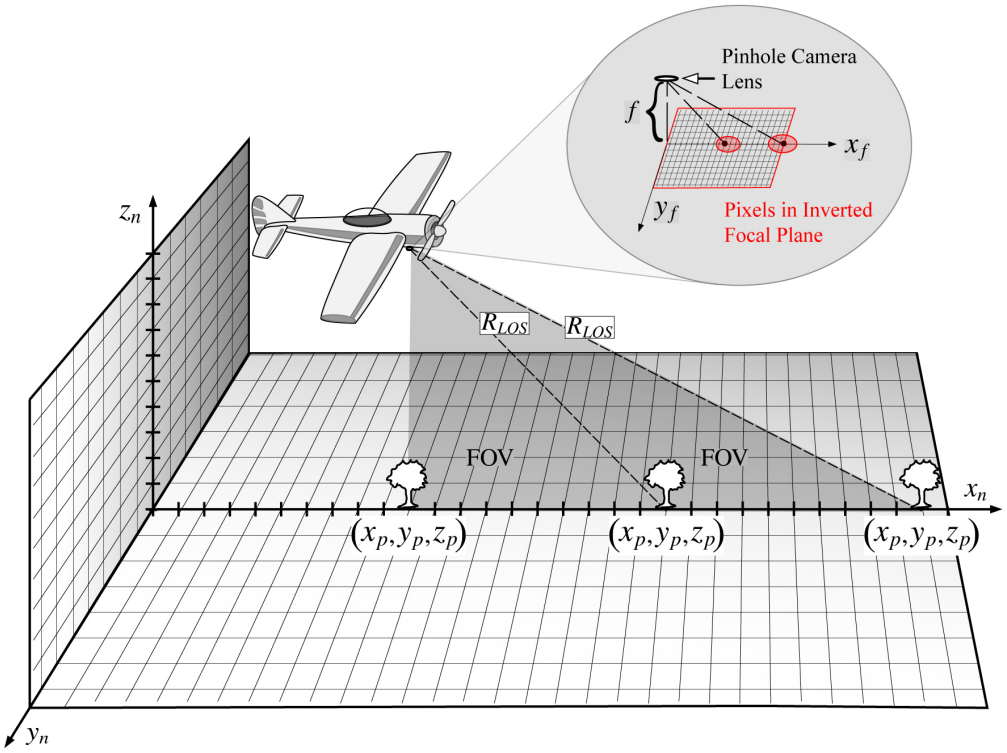

Figure 2.11: Three dimensional image representation

The relationship of the true position and true attitude of the aircraft to that of a ground feature is determined by the attendant geometry and is given by the Main Equation

derived in [3] that follows:

$$\begin{bmatrix} x \\ y \\ z \end{bmatrix} = \begin{bmatrix} x_p \\ y_p \\ z_p \end{bmatrix} - \frac{|R_{LOS}|}{\sqrt{x_f^2 + y_f^2 + f^2}} \mathbf{C}_b^n \begin{bmatrix} x_f \\ y_f \\ -f \end{bmatrix} \tag{2.11}$$

where x_f and y_f are the pixel coordinates in the focal plane of the projected ground feature, whose true position is x_p and y_p, and f is the camera's focal length. The direction cosine matrix $\mathbf{C}_b^n$ previously described in (2.2) transforms a vector coordinatized in the body frame into the very same vector coordinatized in the navigation frame. The expression $\sqrt{x_f^2 + y_f^2 + f^2}$ is used to scale the line-of-sight range (R_{LOS}) between the aircraft and the ground feature. The subscript p designates the position in the navigation frame of the ground feature and the coordinates (x, y, z) without subscripts designate the true position of the aircraft in the navigation frame.

Recall that the navigation frame is attached to the flat and non-rotating Earth. Equation (2.11) can then be separated into three equations as follows:

$$x_p - x = \frac{|R_{LOS}|}{\sqrt{x_f^2 + y_f^2 + f^2}} \begin{bmatrix} 1 & 0 & 0 \end{bmatrix} \mathbf{C}_b^n \begin{bmatrix} x_f \\ y_f \\ -f \end{bmatrix} \tag{2.12}$$

$$y_p - y = \frac{|R_{LOS}|}{\sqrt{x_f^2 + y_f^2 + f^2}} \begin{bmatrix} 0 & 1 & 0 \end{bmatrix} \mathbf{C}_b^n \begin{bmatrix} x_f \\ y_f \\ -f \end{bmatrix} \tag{2.13}$$

$$z_p - z = \frac{|R_{LOS}|}{\sqrt{x_f^2 + y_f^2 + f^2}} \begin{bmatrix} 0 & 0 & 1 \end{bmatrix} \mathbf{C}_b^n \begin{bmatrix} x_f \\ y_f \\ -f \end{bmatrix} \tag{2.14}$$

Equation (2.14) can be rearranged such that the following is true:

$$\frac{|R_{LOS}|}{\sqrt{x_f^2 + y_f^2 + f^2}} = \frac{z_p - z}{\begin{bmatrix} 0 & 0 & 1 \end{bmatrix} \mathbf{C}_b^n \begin{bmatrix} x_f \\ y_f \\ -f \end{bmatrix}} \tag{2.15}$$

It is assumed that the elevation z_p of the tracked ground feature is known to be zero. Two measurement equations are obtained by substituting the right side of (2.15) into (2.12) and (2.13), which yields the following equation:

$$\begin{bmatrix} x_p \\ y_p \end{bmatrix} - \begin{bmatrix} x \\ y \end{bmatrix} = \frac{z_p - z}{\begin{bmatrix} 0 & 0 & 1 \end{bmatrix} \mathbf{C}_b^n \begin{bmatrix} x_f \\ y_f \\ -f \end{bmatrix}} \begin{bmatrix} 1 & 0 & 0 \\ 0 & 1 & 0 \end{bmatrix} \mathbf{C}_b^n \begin{bmatrix} x_f \\ y_f \\ -f \end{bmatrix}$$

This is further simplified by multiplying out the matrices as follows, where $\mathbf{C}_b^n$ is given by (2.2):

$$\begin{bmatrix} x_p \\ y_p \end{bmatrix} - \begin{bmatrix} x \\ y \end{bmatrix} = (z_p - z) \frac{1}{-x_f \cdot \theta + y_f \cdot \phi - f} \begin{bmatrix} x_f - y_f \cdot \psi - f \cdot \theta \\ x_f \cdot \psi + y_f + f \cdot \phi \end{bmatrix}$$

Nondimensionalizing such that the following is the case:

$$x_f \to \frac{x_f}{f}, \qquad y_f \to \frac{y_f}{f}$$

yields the following equation:

$$\begin{bmatrix} x_p \\ y_p \end{bmatrix} - \begin{bmatrix} x \\ y \end{bmatrix} = (z_p - z) \frac{1}{-x_f \cdot \theta + y_f \cdot \phi - 1} \begin{bmatrix} x_f - y_f \cdot \psi - \theta \\ y_f + x_f \cdot \psi + \phi \end{bmatrix}$$

This result can now be separated into two nonlinear measurement equations as follows:

$$x_p - x = (z_p - z) \left(\frac{x_f - \psi \cdot y_f - \theta}{-1 - \theta \cdot x_f + \phi \cdot y_f} \right) \tag{2.16}$$

$$y_p - y = (z_p - z) \left(\frac{y_f + \psi \cdot x_f + \phi}{-1 - \theta \cdot x_f + \phi \cdot y_f} \right) \tag{2.17}$$

To further simplify the measurement equations we can apply the binomial approximation with the small angle assumption. This causes the denominator of (2.16) and (2.17) to be multiplied by the numerator while changing the signs of the small angles as follows:

$$x_p - x \approx (z_p - z)(x_f - y_f \cdot \psi - \theta)(-1 + x_f \cdot \theta - y_f \cdot \phi) \tag{2.18}$$

$$y_p - y \approx (z_p - z)(y_f + x_f \cdot \psi + \phi)(-1 + x_f \cdot \theta - y_f \cdot \phi) \tag{2.19}$$

It is assumed that the ground feature elevation is known and then, without loss of generality, z_p is set equal to zero. Equations (2.18) and (2.19) are further simplified, such that the products of the small angles after distribution are also set equal to zero, thus yielding:

$$x_p - x \approx z\Big(x_f - \theta(1 + x_f^2) + x_f \cdot y_f \cdot \phi - y_f \cdot \psi\Big) \tag{2.20}$$

$$y_p - y \approx z\Big(y_f - x_f \cdot y_f \cdot \theta + \phi(1 + y_f^2) + x_f \cdot \psi\Big) \tag{2.21}$$

The states and measurements are then perturbed such that the following is true:

$$x = x_c - \delta x \qquad y = y_c - \delta y \qquad z = z_c - \delta z$$

$$\theta = \theta_c - \delta\theta \qquad \phi = \phi_c - \delta\phi \qquad \psi = \psi_c - \delta\psi$$

$$x_p = x_{pc} - \delta x_{pc} \qquad y_p = y_{pc} - \delta y_{pc}$$

$$x_f = x_{fm} - \delta x_f \qquad y_f = y_{fm} - \delta y_f$$

where the subscript "c" indicates the navigation state components provided by the Free INS. The subscript "m" indicates measured quantities of the pixels in the focal frame. Inserting the perturbation equations into the measurement equations (2.20) and (2.21) yields the following:

$$\begin{aligned} x_{pc} - \delta x_{pc} - (x_c - \delta x) = (z_c - \delta z)\Big(&x_{fm} - \delta x_f - (\theta_c - \delta\theta)(1 + x_{fm}^2 - 2x_{fm} \cdot \delta x_f + \delta x_f^2) \\ &+ (x_{fm} - \delta x_f)(y_{fm} - \delta y_f)(\phi_c - \delta\phi) - (y_{fm} - \delta y_f)(\psi_c - \delta\psi)\Big) \end{aligned}$$

$$y_{pc} - \delta y_{pc} - (y_c - \delta y) = (z_c - \delta z)\Big(y_{fm} - \delta y_f - (x_{fm} - \delta x_f)(y_{fm} - \delta y_f)(\theta_c - \delta\theta) + (\phi_c - \delta\phi)(1 + y_{fm}^2 - 2y_{fm} \cdot \delta y_f + \delta y_f^2) + (x_{fm} - \delta x_f)(\psi_c - \delta\psi)\Big)$$

Due to the small error in the measurements and the small angles, the products of these terms can be neglected. Therefore, the measurement equations can be further reduced to the linear forms that follow:

$$x_{pc} - \delta x_{pc} - (x_c - \delta x) = (z_c - \delta z)\Big(x_{fm} - \delta x_f - (\theta_c - \delta\theta)(1 + x_{fm}^2) + (x_{fm} \cdot y_{fm})(\phi_c - \delta\phi) - y_{fm}(\psi_c - \delta\psi)\Big)$$

$$y_{pc} - \delta y_{pc} - (y_c - \delta y) = (z_c - \delta z)\Big(y_{fm} - \delta y_f - (x_{fm} \cdot y_{fm})(\theta_c - \delta\theta) + (\phi_c - \delta\phi)(1 + y_{fm}^2) + x_{fm}(\psi_c - \delta\psi)\Big)$$

By moving all the error terms (navigation state error and measurement errors) to the Right Hand Side (RHS) and all the non-error terms (INS-provided navigation state and pixel position measurements) to the Left Hand Side (LHS) of the two measurement equations, the Kalman filter measurement equations are obtained as follows:

$$\boxed{\begin{aligned} x_{pc} - x_c - z_c\Big(x_{fm} - \theta_c(1 + x_{fm}^2) + \phi_c \cdot x_{fm} \cdot y_{fm} - \psi_c \cdot y_{fm}\Big) = \\ - \delta x - \delta z \cdot x_f + \delta\theta(1 + x_f^2) - \delta\phi \cdot x_f \cdot y_f + \delta\psi \cdot y_f + \delta x_{pc} - \delta x_f \end{aligned}} \tag{2.22}$$

$$\boxed{\begin{aligned} y_{pc} - y_c - z_c\Big(y_{fm} - \theta_c \cdot x_{fm} \cdot y_{fm} + \phi_c(1 + y_{fm}^2) + \psi_c \cdot x_{fm}\Big) = \\ - \delta y - \delta z \cdot y_f + \delta\theta \cdot x_f \cdot y_f - \delta\phi(1 + y_f^2) - \delta\psi \cdot x_f + \delta y_{pc} - \delta y_f \end{aligned}} \tag{2.23}$$

2.6 Summary

In summary, this chapter has presented the mathematical background required to understand the development and simulation of the automated driftmeter fused with inertial measurements. The three reference frames used in this research, strapdown INS concepts, Kalman filtering equations, and bearing measurement equations were introduced in this chapter. Chapter 3 will now provide the specific calculations used to develop the navigation scenario for this research.

III. Methodology

This chapter provides a detailed description of the simulations conducted and the algorithms used in this research. The navigation scenario developed in [3] and followed up in [4] is first presented. Next, the continuous-time INS error equations developed in this research from the merging of equations (2.6) and (2.7) is introduced. This is followed by the discrete-time equivalent INS error equations, which are used to develop the navigation-grade INS specifications for this research. After these 1-σ INS error specifications are developed, they are used throughout the research for three different INS scenarios. The first scenario incorporates the error specifications for the accelerometers' and gyroscopes' drift. The second incorporates the error specifications for the accelerometers' and gyroscopes' biases. Finally, the third incorporates a combination of these two error sources. This presentation method is employed with the development of geolocation and tracking as well as the transitioning between these tracked ground features.

3.1 Navigation Scenario

It is assumed the aircraft is flying straight and level at a constant velocity over a flat and non-rotating Earth. All of the system variables and parameters are non-dimensionalized according to Table 3.1 [5]. With the aircraft cruising at a constant

Table 3.1: Non-dimensionalized navigation scenario parameters

Position	Velocity	Specific Force Error	Angular Rate Error	Time
$x \rightarrow \frac{x}{h}$	$v_x \rightarrow \frac{v_x}{v}$	$\delta f_x \rightarrow \frac{\delta f_x}{g}$	$\delta\omega_x^{(b)} \rightarrow h\frac{\delta\omega_x^{(b)}}{v}$	$t \rightarrow t\frac{v}{h}$
$y \rightarrow \frac{y}{h}$	$v_y \rightarrow \frac{v_y}{v}$	$\delta f_y \rightarrow \frac{\delta f_y}{g}$	$\delta\omega_y^{(b)} \rightarrow h\frac{\delta\omega_y^{(b)}}{v}$	$T \rightarrow T\frac{v}{h}$
$z \rightarrow \frac{z}{h}$	$v_z \rightarrow \frac{v_z}{v}$	$\delta f_z \rightarrow \frac{\delta f_z}{g}$	$\delta\omega_z^{(b)} \rightarrow h\frac{\delta\omega_z^{(b)}}{v}$	

nominal/true altitude $h = 1000\ m$, the nominal/true velocity is $v = 100\ \frac{m}{s}$. The gravity acceleration is assumed to be $g = 10\ \frac{m}{s^2}$ and is non-dimensionalized according to the following:

$$g \rightarrow \frac{h \cdot g}{v^2} = \frac{1000\ m \cdot 10\ \frac{m}{s^2}}{(100\ \frac{m}{s})^2} = \frac{10000\ \frac{m^2}{s^2}}{10000\ \frac{m^2}{s^2}} = 1 \tag{3.1}$$

The camera frame rate is the same as the sampling frequency f_s which is 1 Hz. The sampling time ΔT is non-dimensionalized and calculated according to the following:

$$\Delta T \rightarrow \frac{1}{f_s} \cdot \frac{v}{h} = \frac{1}{1\ \frac{1}{s}} \cdot \frac{100\ \frac{m}{s}}{1000\ m} = 0.1 \tag{3.2}$$

3.2 INS Error Equations

It is necessary to develop a linear dynamic model of the INS errors. The flight scenario is highly idealized so that the aircraft dynamics are minimized and the INS errors are modeled. There are many sources of errors that impact the performance of an INS. Reference [17] states that significant error sources include alignment errors, sensor drift/bias errors, and computational errors. In this research, the INS alignment errors are assumed to be zero. An evaluation of computational errors is outside the scope of this research and will not be addressed. The INS's accelerometer and gyroscope sensors each have two types of errors: a Gaussian distributed random start-up bias error and a Gaussian random walk/drift error.

The continuous-time INS navigation state error $\delta\mathbf{x}$ dynamics are represented in state space form as follows:

$$d\delta\mathbf{x} = (\mathbf{A_c} \cdot \delta\mathbf{x} + \mathbf{\Gamma_c} \cdot \delta\mathbf{u})dt + \mathbf{\Gamma_c} \cdot d\mathbf{w} \tag{3.3}$$

which is rewritten as follows:

$$\boxed{\delta\dot{\mathbf{x}}(t) = \mathbf{A_c} \cdot \delta\mathbf{x}(t) + \mathbf{\Gamma_c} \cdot \delta\mathbf{u}(t) + \mathbf{\Gamma_c} \cdot \dot{\mathbf{w}}(t)} \tag{3.4}$$

where $\delta\mathbf{x}$ is the navigation state error vector $\mathbf{A_c}$ is the system error dynamics matrix, $\mathbf{\Gamma_c}$ is an input matrix, $\delta\mathbf{u}$ is the unknown accelerometer and gyro biases vector, and $\mathbf{w}$ is a

Brownian motion vector (which quantifies the gyros' and accelerometers' drift). The navigation state error vector is as follows:

$$\delta\mathbf{x} = [\ \delta x,\ \ \delta y,\ \ \delta z,\ \ \delta v_x,\ \ \delta v_y,\ \ \delta v_z,\ \ \delta\phi,\ \ \delta\theta,\ \ \delta\psi\ ]^T \tag{3.5}$$

The accelerometers' and gyros' bias errors are random on start-up but constant thereafter. The errors are expressed as follows:

$$\delta\mathbf{u} = [\ \delta f_x^{(b)},\ \ \delta f_y^{(b)},\ \ \delta f_z^{(b)},\ \ \delta\omega_x^{(b)},\ \ \delta\omega_y^{(b)},\ \ \delta\omega_z^{(b)}\ ]^T \tag{3.6}$$

where the accelerometer's bias errors ($\delta f^{(b)}$) are Gaussian distributed with a mean of zero and a standard deviation of σ_{b_a}. The gyroscope's bias errors, ($\delta\omega^{(b)}$) are also Gaussian distributed with a mean of zero and a standard deviation of σ_{b_g}. They are described as follows:

$$\begin{aligned} \delta f^{(b)} &\sim N(0,\ \sigma_{b_a}^2) \\ \delta\omega^{(b)} &\sim N(0,\ \sigma_{b_g}^2) \end{aligned} \tag{3.7}$$

The vector of white noise processes $\dot{\mathbf{w}}$ is an additive zero mean Gaussian process with covariance expressed as follows:

$$E\{\dot{\mathbf{w}}(t)\cdot\dot{\mathbf{w}}^T(t+\tau)\} = \mathbf{Q}\cdot\delta(\tau)$$

where $\delta(\tau)$ is the Dirac delta function. It accounts for high-bandwidth error sources such as electrical noise and/or thermal noise in the gyros and accelerometers. The $\dot{\mathbf{w}}$ vector contains the random walk standard deviation scale values for the accelerometers (σ_{d_a}) and gyroscopes (σ_{d_g}), is expressed as follows

$$\dot{\mathbf{w}} = \begin{bmatrix} N(0,\ \mathbf{I}_3\cdot\sigma_{d_a}^2) \\ N(0,\ \mathbf{I}_3\cdot\sigma_{d_g}^2) \end{bmatrix}_{6\times1} \tag{3.8}$$

where all four sensor noise standard deviation values will be calibrated for this navigation scenario in a later section.

The error dynamics matrix $\mathbf{A_c}$ is as follows:

$$\mathbf{A_c} = \begin{bmatrix} 0 & \mathbf{I}_3 & 0 \\ 0 & 0 & -\mathbf{F}^{(n)} \\ 0 & 0 & 0 \end{bmatrix}_{9\times 9} \tag{3.9}$$

where $\mathbf{F}^{(n)}$, as developed in (2.5), is the skew-symmetric matrix form of the specific force vector $f^{(n)}$ in the navigation frame.

The input matrix $\mathbf{\Gamma_c}$ is as follows:

$$\mathbf{\Gamma_c} = \begin{bmatrix} 0 & 0 \\ \mathbf{C}_b^n & 0 \\ 0 & \mathbf{C}_b^n \end{bmatrix}_{9\times 6} \tag{3.10}$$

where the matrix $\mathbf{C}_b^n$ is the body to navigation frame DCM developed in (2.2). At constant altitude flight in the direction of the x axis, the nominal/true $\mathbf{C}_b^n = \mathbf{I}_3$.

3.3 Discrete-Time Dynamics

The continuous-time navigation state error in (3.4) is converted to discrete-time with a sampling interval of ΔT, calculated in (3.2). The discrete-time navigation error state equation is then as follows:

$$\boxed{\delta\mathbf{x}_{k+1} = \mathbf{A_d} \cdot \delta\mathbf{x}_k + \mathbf{\Gamma_d} \cdot \delta\mathbf{u}_k + \mathbf{\Gamma_c} \cdot \mathbf{w}_k} \tag{3.11}$$

where the subscript k represents discrete instances in time.

The discrete-time state transition matrix $\mathbf{A_d}$ is calculated from the continuous-time dynamics matrix $\mathbf{A_c}$ according to the following:

$$\mathbf{A_d} = e^{\mathbf{A_c}\cdot\Delta T}$$

Therefore, we calculate matrix $\mathbf{A_d}$ as follows:

$$\mathbf{A_d} = \begin{bmatrix} \mathbf{I}_3 & \mathbf{I}_3 \cdot \Delta T & -\frac{1}{2} \cdot \mathbf{F}^{(n)} \cdot \Delta T^2 \\ 0 & \mathbf{I}_3 & -\mathbf{F}^{(n)} \cdot \Delta T \\ 0 & 0 & \mathbf{I}_3 \end{bmatrix}_{9\times 9}$$

which for the substitutions in Section 3.1 quantifies to the following:

$$\mathbf{A_d} = \begin{bmatrix} 1 & 0 & 0 & 0.1 & 0 & 0 & 0 & 0.005 & 0 \\ 0 & 1 & 0 & 0 & 0.1 & 0 & -0.005 & 0 & 0 \\ 0 & 0 & 1 & 0 & 0 & 0.1 & 0 & 0 & 0 \\ 0 & 0 & 0 & 1 & 0 & 0 & 0 & 0.1 & 0 \\ 0 & 0 & 0 & 0 & 1 & 0 & -0.1 & 0 & 0 \\ 0 & 0 & 0 & 0 & 0 & 1 & 0 & 0 & 0 \\ 0 & 0 & 0 & 0 & 0 & 0 & 1 & 0 & 0 \\ 0 & 0 & 0 & 0 & 0 & 0 & 0 & 1 & 0 \\ 0 & 0 & 0 & 0 & 0 & 0 & 0 & 0 & 1 \end{bmatrix}$$

The input matrix $\mathbf{\Gamma_c}$ is transformed to discrete-time according to the following equation:

$$\mathbf{\Gamma_d} = \left(\int_0^{\Delta T} e^{\mathbf{A_c} \cdot t} dt \right) \cdot \mathbf{\Gamma_c}$$

where the integral is as follows:

$$\left(\int_0^{\Delta T} e^{\mathbf{A_c} \cdot t} dt \right) = \begin{bmatrix} \mathbf{I}_3 \cdot \Delta T & \frac{1}{2} \cdot \mathbf{I}_3 \cdot \Delta T^2 & -\frac{1}{6} \cdot \mathbf{F}^{(n)} \cdot \Delta T^3 \\ 0 & \mathbf{I}_3 \cdot \Delta T & -\frac{1}{2} \cdot \mathbf{F}^{(n)} \cdot \Delta T^2 \\ 0 & 0 & \mathbf{I}_3 \cdot \Delta T \end{bmatrix}_{9 \times 9}$$

This integral quantifies as follows:

$$\left(\int_0^{\Delta T} e^{\mathbf{A_c} \cdot t} dt\right) = \begin{bmatrix} 0.1 & 0 & 0 & 0.005 & 0 & 0 & 0 & 0.000167 & 0 \\ 0 & 0.1 & 0 & 0 & 0.005 & 0 & -0.000167 & 0 & 0 \\ 0 & 0 & 0.1 & 0 & 0 & 0.005 & 0 & 0 & 0 \\ 0 & 0 & 0 & 0.1 & 0 & 0 & 0 & 0.005 & 0 \\ 0 & 0 & 0 & 0 & 0.1 & 0 & -0.005 & 0 & 0 \\ 0 & 0 & 0 & 0 & 0 & 0.1 & 0 & 0 & 0 \\ 0 & 0 & 0 & 0 & 0 & 0 & 0.1 & 0 & 0 \\ 0 & 0 & 0 & 0 & 0 & 0 & 0 & 0.1 & 0 \\ 0 & 0 & 0 & 0 & 0 & 0 & 0 & 0 & 0.1 \end{bmatrix}$$

The product of the integral and $\mathbf{\Gamma_c}$ yields the discrete-time input matrix that follows:

$$\mathbf{\Gamma_d} = \begin{bmatrix} \frac{1}{2} \cdot \mathbf{I}_3 \cdot \Delta T^2 & -\frac{1}{6} \cdot \mathbf{F}^{(n)} \cdot \Delta T^3 \\ \mathbf{I}_3 \cdot \Delta T & -\frac{1}{2} \cdot \mathbf{F}^{(n)} \cdot \Delta T^2 \\ 0 & \mathbf{I}_3 \cdot \Delta T \end{bmatrix}_{9 \times 6}$$

$\mathbf{\Gamma_d}$ finally quantifies to the following:

$$\mathbf{\Gamma_d} = \begin{bmatrix} 0.005 & 0 & 0 & 0 & 0.0001667 & 0 \\ 0 & 0.005 & 0 & -0.0001667 & 0 & 0 \\ 0 & 0 & 0.005 & 0 & 0 & 0 \\ 0.1 & 0 & 0 & 0 & 0.005 & 0 \\ 0 & 0.1 & 0 & -0.005 & 0 & 0 \\ 0 & 0 & 0.1 & 0 & 0 & 0 \\ 0 & 0 & 0 & 0.1 & 0 & 0 \\ 0 & 0 & 0 & 0 & 0.1 & 0 \\ 0 & 0 & 0 & 0 & 0 & 0.1 \end{bmatrix}$$

The discrete-time random drift error vector $\mathbf{w}_k$ remains the same as the continuous-time, random drift error vector in (3.8) as follows:

$$\mathbf{w_k} \sim \begin{bmatrix} N(0,\ \mathbf{I}_3 \cdot \sigma_{d_a}^2) \\ N(0,\ \mathbf{I}_3 \cdot \sigma_{d_g}^2) \end{bmatrix}_{6\times 1} \tag{3.12}$$

where it remains multiplied by the continuous-time input matrix $\mathbf{\Gamma_c}$. This is done while taking into account the discrete-time sampling interval ΔT. Each of the six drift errors are Gaussian distributed and randomly selected at every time instant k. The associated covariance is as follows:

$$E\{\mathbf{w}_k \cdot \mathbf{w}_k^T\} = \mathbf{Q_d}$$

and in matrix form is as follows:

$$\mathbf{Q_d} = \begin{bmatrix} \mathbf{I}_3 \cdot \sigma_{d_a}^2 & 0 \\ 0 & \mathbf{I}_3 \cdot \sigma_{d_g}^2 \end{bmatrix}_{6\times 6}$$

3.4 Augmenting the System Dynamics with Constant Biases

The navigation state error vector $\delta\mathbf{x}$ is augmented with the bias input error vector $\delta\mathbf{u}$, because the bias errors are random on system start-up but constant thereafter. The augmented navigation state error vector is as follows:

$$\delta\mathbf{x_a}_k = \begin{bmatrix} \delta\mathbf{x}_k \\ \vdots \\ \delta\mathbf{u}_k \end{bmatrix}_{15\times 1} \qquad \delta\mathbf{x_a}_0 \sim N\left(0,\ \begin{bmatrix} \mathbf{0}_{9\times 9} & \mathbf{0}_{3\times 3} & \mathbf{0}_{3\times 3} \\ \mathbf{0}_{3\times 3} & \mathbf{I}_3 \cdot \sigma_{b_a}^2 & \mathbf{0}_{3\times 3} \\ \mathbf{0}_{3\times 3} & \mathbf{0}_{3\times 3} & \mathbf{I}_3 \cdot \sigma_{b_g}^2 \end{bmatrix}_{15\times 15}\right) \tag{3.13}$$

The augmented discrete-time navigation state error equation is as follows:

$$\boxed{\delta\mathbf{x_a}_{k+1} = \mathbf{A_{da}} \cdot \delta\mathbf{x_a}_k + \mathbf{\Gamma_{ca}} \cdot \mathbf{w}_k} \tag{3.14}$$

where the initial covariance accounts for the uncertainty in the original nine INS error states' alignment and the Gaussian distributed random bias error states. The state transition matrix $\mathbf{A_d}$ is augmented with the discrete-time input matrix $\mathbf{\Gamma_d}$ as follows:

$$\mathbf{A_{da}} = \begin{bmatrix} \mathbf{A_d} & \mathbf{\Gamma_d} \\ \mathbf{0}_{6\times 9} & \mathbf{I}_6 \end{bmatrix}_{15\times 15} \tag{3.15}$$

The continuous-time input matrix $\mathbf{\Gamma_c}$ must be augmented with zeros, as follows:

$$\mathbf{\Gamma_{ca}} = \begin{bmatrix} \mathbf{\Gamma_c} \\ \mathbf{0}_{6\times6} \end{bmatrix}_{15\times6} \tag{3.16}$$

The discrete-time random walk vector $\mathbf{w}_k$ remains the same as specified in (3.12).

3.5 Navigation Grade INS Calibration

For this simulation the bias and random walk measurement errors for the accelerometers and gyroscopes are assumed to be equally responsible for the INS errors. A covariance analysis of the INS x position error state is used to calculate the standard deviation values for the sensors biases and drift, which will cause a 1 $\frac{km}{hr}$ navigation error. Using the discrete-time Lyapunov equation that follows:

$$\mathbf{P}_{k+1} = \mathbf{A_{da}} \cdot \mathbf{P}_k \cdot \mathbf{A_{da}}^T + \mathbf{\Gamma_{ca}} \cdot \mathbf{Q_d} \cdot \mathbf{\Gamma_{ca}}^T, \qquad k = 0, 1, \ \ldots \ , 3600 \tag{3.17}$$

The state covariance matrix $\mathbf{P}$ (uncertainty in the system state dynamics) is propagated throughout a one hour flight. The discrete noise covariance matrix $\mathbf{Q_d}$ (uncertainty in the system noise input) is constant throughout the flight. It is assumed that there are no INS initial alignment errors. Therefore, the navigation state errors provided in (3.5) at the initial time step ($k = 0$) are all zero and the measurement bias errors are random and Gaussian distributed. Measurement bias errors are represented within the navigation state error initial conditions $\delta\mathbf{x_{a0}}$ as follows:

$$\delta\mathbf{x}_{\mathbf{a}0} = \begin{bmatrix} \mathbf{0}_{9\times1} \\ \zeta_{3\times1} \\ \gamma_{3\times1} \end{bmatrix}_{15\times1} \tag{3.18}$$

where $\zeta \sim N(0, \ \mathbf{I}_3 \cdot \sigma_{b_a}^2)$ and $\gamma \sim N(0, \ \mathbf{I}_3 \cdot \sigma_{b_g}^2)$. The uncertainty at start-up is specified by the accelerometers' and gyroscopes' bias standard deviation σ_{b_a} and σ_{b_g}, respectively.

Therefore, the navigation state error covariance matrix $\mathbf{P}_k$ is initialized as follows:

$$\mathbf{P}_0 = \begin{bmatrix} \mathbf{0}_{9\times9} & \mathbf{0}_{9\times3} & \mathbf{0}_{9\times3} \\ \mathbf{0}_{3\times9} & \mathbf{I}_3 \cdot \sigma_{b_a}^2 & \mathbf{0}_{3\times3} \\ \mathbf{0}_{3\times3} & \mathbf{0}_{3\times3} & \mathbf{I}_3 \cdot \sigma_{b_g}^2 \end{bmatrix}_{15\times15} \tag{3.19}$$

The accelerometers' and gyros' drift is described as follows:

$$\mathbf{Q_d} = \begin{bmatrix} \mathbf{I}_3 \cdot \sigma_{d_a}^2 & \mathbf{0}_{3\times3} \\ \mathbf{0}_{3\times3} & \mathbf{I}_3 \cdot \sigma_{d_g}^2 \end{bmatrix}_{6\times6} \tag{3.20}$$

The system dynamics are propagated at the non-dimensional sampling interval ΔT with the Lyapunov equation shown in (3.17). This is done for one non-dimensional hour, 3600 time steps, in order to determine the final variance value of x-position. This final value constitutes element (1,1) of the covariance matrix so it equals $(\mathbf{P}_{3600})_{1,1}$.

This propagation is repeated four times to determine the final x-position of the variance for each measurement error. Each time only one measurement error contributes to the 1 $\frac{km}{hr}$ navigation error. This is represented in Table 3.2. There is a linear relationship

Table 3.2: Final x-position variance values after propagating for one hour according to set INS sensor error parameters.

Final Value	Accel bias σ	Gyro bias σ	Accel drift σ	Gyro drift σ
$\alpha_b = (\mathbf{P}_{3600})_{1,1}$	$\sigma_{b_a} = 1$	$\sigma_{b_g} = 0$	$\sigma_{b_g} = 0$	$\sigma_{d_g} = 0$
$\beta_b = (\mathbf{P}_{3600})_{1,1}$	$\sigma_{b_a} = 0$	$\sigma_{b_g} = 1$	$\sigma_{b_g} = 0$	$\sigma_{d_g} = 0$
$\alpha_d = (\mathbf{P}_{3600})_{1,1}$	$\sigma_{b_a} = 0$	$\sigma_{b_g} = 0$	$\sigma_{b_g} = 1$	$\sigma_{d_g} = 0$
$\beta_d = (\mathbf{P}_{3600})_{1,1}$	$\sigma_{b_a} = 0$	$\sigma_{b_g} = 0$	$\sigma_{b_g} = 0$	$\sigma_{d_g} = 1$

between the uncertainty in the accelerometer and the gyro variance, which can be directly related to the aircraft's final x-position variance. This linear relationship is as follows:

$$(\mathbf{P}_{3600})_{1,1} = \alpha_b \cdot \sigma_{b_a}^2 + \beta_b \cdot \sigma_{b_g}^2 + \alpha_d \cdot \sigma_{d_a}^2 + \beta_d \cdot \sigma_{d_g}^2 \tag{3.21}$$

The accelerometers and gyros are assumed to be equally at fault and their standard deviations are scaled according to Table 3.3. These standard deviation values are now

Table 3.3: Calibrated navigation-grade INS specifications for $1\frac{km}{hr}$.

Final x-Position Variance	Scaled With	Calibrated INS Sensor Specifications
$\alpha_b = 4.2037 \times 10^9$	$\frac{1}{\sqrt{4 \cdot \alpha_b}}$	$\sigma_{b_a} = 7.7118 \times 10^{-6}$
$\beta_b = 6.0567 \times 10^{13}$	$\frac{1}{\sqrt{4 \cdot \beta_b}}$	$\sigma_{b_g} = 6.4247 \times 10^{-8}$
$\alpha_d = 1.5558 \times 10^8$	$\frac{1}{\sqrt{4 \cdot \alpha_d}}$	$\sigma_{d_a} = 4.0085 \times 10^{-5}$
$\beta_d = 3.0254 \times 10^{12}$	$\frac{1}{\sqrt{4 \cdot \beta_d}}$	$\sigma_{d_g} = 2.8746 \times 10^{-7}$

used together in the Lyapunov equation shown in (3.17) to propagate the x-position variance of the INS throughout the one hour flight and verify that it does yield the $1\ \frac{km}{hr}$ navigation error. Figure 3.1 illustrates the propagated x-position variance with accelerometer and gyroscope noise standard deviations according to the calibrated sensor specifications in Table 3.3.

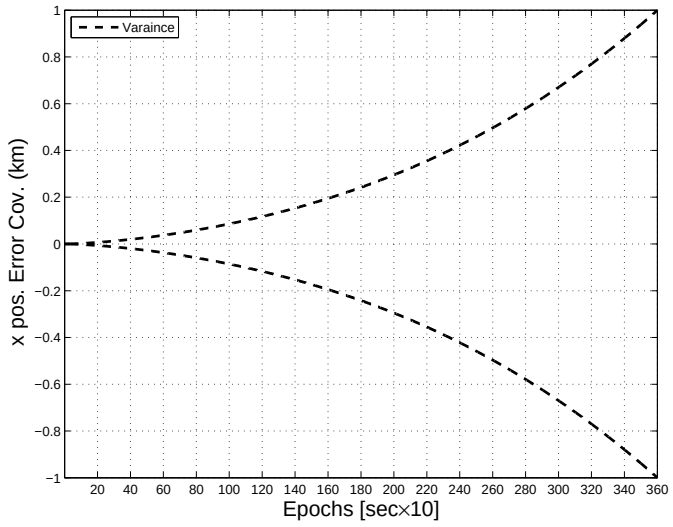

Figure 3.1: x-position error standard deviation with biases and process noise

3.6 Free INS

The drift errors for the simulated Free INS are developed by propagating the discrete-time stochastic INS error equations for one hour. In this section the performance of the Free INS is presented with just drift errors sources, just bias errors sources, and with combined error sources. The calibrated sensor error standard deviation values in Table 3.3 are used throughout this research.

3.6.1 Drift Induced Error.

The sensor drift errors that plague an INS are a result of high-bandwidth sources such as electrical noise and/or thermal noise from every accelerometer and gyroscope discrete measurement throughout the flight. The result of the noisy measurements is a random walk superimposed on the true measurement. The random walk measurement errors will cause the errors to drift either positive or negative of the true measurement with a strength drawn from a zero mean, Gaussian distribution. The strictly drift-driven navigation state error equation is extracted from the original form of the discrete-time navigation error state equation shown in (3.11) before any augmentation as follows:

$$\boxed{\delta\mathbf{x}_{k+1} = \mathbf{A_d} \cdot \delta\mathbf{x}_k + \mathbf{\Gamma_c} \cdot \mathbf{w}_k} \tag{3.22}$$

This equation is propagated with k throughout the one hour flight. The vector of white noise processes $\mathbf{w}_k$ is randomly selected for every iteration according to (3.12). The covariance $\mathbf{P}_{k+1}$ of the drift-caused navigation state error is calculated using the discrete-time Lyapunov equation as follows:

$$\mathbf{P}_{k+1} = \mathbf{A_d} \cdot \mathbf{P}_k \cdot \mathbf{A_d}^T + \mathbf{\Gamma_c} \cdot \mathbf{Q_d} \cdot \mathbf{\Gamma_c}^T \tag{3.23}$$

where the navigation state error covariance matrix $\mathbf{P}$ is propagated for one hour to generate a 68% error state estimate for each of the nine state values throughout the flight. It is assumed that there are no INS alignment errors. Therefore, the navigation state errors provided in (3.5) at $k = 0$ are all zero and there is 100% confidence in the alignment. This

confidence is inversely proportional to the uncertainty in the alignment (also referred to as the covariance **P**). The covariance matrix for the Free INS alignment is therefore as follows:

$$\mathbf{P}_0 = \begin{bmatrix} 0 & & 0 \\ & \ddots & \\ 0 & & 0 \end{bmatrix}_{9\times 9}$$

The random input from the white noise processes $\mathbf{w_k}$ will be different each time the simulation is run and consequently so will be the navigation state error dynamics. Appendix B contains Figures B.1, B.2, and B.3, which illustrate the drift error and covariance from just one run of the Free INS with only sensor drift error inputs.

3.6.2 Bias Induced Error.

The accelerometers' and gyroscopes' bias errors are random on start-up but constant thereafter. Maybeck [1] refers to these types of error as turnon-to-turnon nonrepeatability biases, because they change from one period of operation to another. They should not be confused with alignment errors (said to be zero for this simulation) that occur as a result of the error between the aircraft's true position, velocity, and attitude relative to where the external navigation source said it was during the alignment. After alignment, the biases are constant and cause the INS measurements to be offset by that bias until the next alignment. Therefore the strictly bias-caused navigation state error equation is only random during initial alignment. The simulation randomly selects the bias values during initialization from a Gaussian distribution described in (3.7). They then remain constant throughout that simulated one hour flight.

The strictly bias state space error equation $\delta\mathbf{x}_{\mathbf{a}k+1}$ is extracted from (3.14) and is as follows:

$$\boxed{\delta\mathbf{x}_{\mathbf{a}k+1} = \mathbf{A_{da}} \cdot \delta\mathbf{x}_{\mathbf{a}k}} \tag{3.24}$$

where it is propagated with iterations of k throughout the one hour flight and the bias terms are augmented into the state transition matrix $\mathbf{A_{da}}$. The covariance of the navigation

state error caused by the bias is calculated using the augmented discrete-time Lyapunov equation as follows:

$$\mathbf{P}_{k+1} = \mathbf{A_{da}} \cdot \mathbf{P}_k \cdot \mathbf{A_{da}}^T \tag{3.25}$$

The augmented navigation state error vector $\delta\mathbf{x_a}$ is initialized according to (3.18). Therefore, the augmented covariance matrix $\mathbf{P}_0$ is initialized according to (3.19).

The covariance for the Free INS will be driven by the covariance of the bias terms and will be the same every time the simulation is run. However, the random choice that creates the bias terms during initialization will be different each time the simulation is run and the propagated error will be different each time. Appendix B contains Figures B.4, B.5, B.6, B.7, and B.8, which illustrate the bias-caused error and covariance from just one run of the Free INS with only sensor bias error inputs.

3.6.3 Bias and Drift Induced Errors.

The combination of the two error sources creates a noisy output that has a random walk about the bias relative to the true measurement. If the true measurement were zero, then the bias offset would be added first and then the random walk would be added to cause a drift around the bias. The navigation state error equation with both error sources is the same as presented in (3.14). It is presented again here for reference:

$$\boxed{\delta\mathbf{x}_{\mathbf{a}k+1} = \mathbf{A_{da}} \cdot \delta\mathbf{x}_{\mathbf{a}k} + \mathbf{\Gamma_{ca}} \cdot \mathbf{w}_k}$$

The navigation state error is propagated for one hour and its covariance $\mathbf{P}_{k+1}$ is calculated using the following equation:

$$\mathbf{P}_{k+1} = \mathbf{A_{da}} \cdot \mathbf{P}_k \cdot \mathbf{A_{da}}^T + \mathbf{\Gamma_{ca}} \cdot \mathbf{Q_d} \cdot \mathbf{\Gamma_{ca}}^T \tag{3.26}$$

The realization of the drift-caused error and the bias error will be different every time the simulation is run. Appendix B contains Figures B.9, B.10, B.11, B.12, and B.13, which illustrate the error and covariance from just one run of the Free INS with drift and bias sensor error.

3.6.4 Free INS Output.

The errors developed in this section from propagating the Free INS must be added to the true state of the simulated aircraft flight in order to establish an INS output of a moving aircraft. As mentioned in Section 3.1, the aircraft is flying straight and level at a constant velocity over a flat and non-rotating Earth. Therefore, the only true dynamics of the simulated aircraft is the movement in the x direction. This movement is due to the aircraft's constant velocity, which directly relates to the true aircraft position. Therefore, the output of the Free INS is calculated according to Table 3.4, where the subscript c indicates that the value is the INS-calculated output. These calculated INS output values are used in the measurement equation to establish the measurements provided to the Kalman filter.

Table 3.4: Free INS Output

Position	Velocity	Attitude
$x_c = t + \delta x$	$v_{x_c} = 1 + \delta v_x$	$\phi_c = \delta\phi$
$y_c = \delta y$	$v_{y_c} = \delta v_y$	$\theta_c = \delta\theta$
$z_c = 1 + \delta x$	$v_{z_c} = \delta v_z$	$\psi_c = \delta\psi$

3.7 SLAM

A measurement epoch n (period of time) is initiated by the geolocation of a new ground feature. Without loss of generality it is simulated that the ground features are arranged such that they are evenly spaced 1000 m apart. With the aircraft moving at a constant speed of 100 $\frac{m}{s}$ ground speed in the direction of the ground features, each epoch is $10s$ long. Therefore, the simulation of a one hour flight will have 360 epochs, and $n = 1, ..., N$, where $N = 360$. Camera measurements are taken at the same interval that the Free INS is sampled $\Delta T = 1\ s$, so there are 10 camera measurements per measurement epoch. According to [19], at least two ground features must be tracked at all times in order

to maintain observability when bearing-only measurements are used. Observability is increased as more ground features are tracked. However, this work assumes only two ground features are tracked in each measurement epoch.

The first epoch ($n = 1$) is different from the remaining epochs because in the first epoch the camera simultaneously geolocates two ground features. The first ground feature, x_{p_1}, is at 1000 m and the second, x_{p_2}, is at 2000 m. These factors are non-dimensionalized according to Table 3.1 to $x_{p_1} = 1$ and $x_{p_2} = 2$. A two-dimensional representation of the geolocated ground features for the first epoch is illustrated in Figure 3.2. The Free INS is perfectly aligned. The INS x calculated position, x_c, is exactly zero. The INS z calculated position, z_c, is exactly one. The INS y calculated position, y_c, is exactly zero, and is not illustrated.

The geolocated ground features are acquired while the aircraft position is exactly known with noisy camera measurements. Therefore, the first two geolocated ground feature's positions are calculated according to Table 3.5, where the geolocation state error values δx_{pc} and δy_{pc} are on average zero, with an uncertainty associated with the standard deviation of the camera measurement σ_c^2.

Table 3.5: Calculated non-dimensional position measurements for first two ground features

Ground Feature # 1	Ground Feature # 2
$x_{pc_1} = 1 + \delta x_{pc_1}$	$x_{pc_2} = 2 + \delta x_{pc_2}$
$y_{pc_1} = 0 + \delta y_{pc_1}$	$y_{pc_2} = 0 + \delta y_{pc_2}$

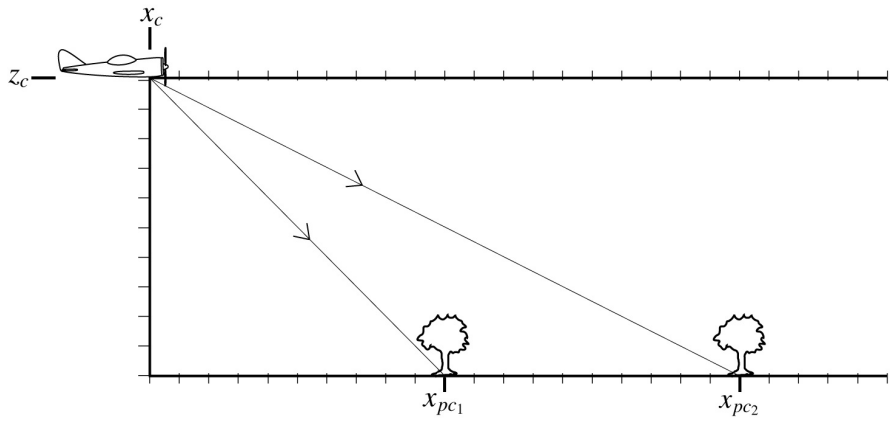

Figure 3.2: First Epoch where the first two ground features are geolocated

The navigation state error vector $\delta\mathbf{x}$ is augmented with the geolocation error vector $\delta\mathbf{s}$ as follows:

$$\delta\mathbf{s} = \begin{bmatrix} \delta x_{pc_1} \\ \delta y_{pc_1} \\ \delta x_{pc_2} \\ \delta y_{pc_2} \end{bmatrix}_{4\times 1} \tag{3.27}$$

which accounts for the accumulated error from acquiring a ground feature while using a noise-corrupted bearing measurement and the error prone INS-provided ownship position. For the first epoch it is assumed that the aircraft position measurements are known exactly. However, the camera measurements are noise-corrupted with a standard deviation σ_c. Therefore, the initial geolocation error vector $\delta\mathbf{s}_0$ is as follows:

$$\delta\mathbf{s}_0 = \begin{bmatrix} \delta x_{pc_1} \\ \delta y_{pc_1} \\ \delta x_{pc_2} \\ \delta y_{pc_2} \end{bmatrix}_{4\times 1} \sim \begin{bmatrix} N(0,\sigma_c^2) \\ N(0,\sigma_c^2) \\ N(0,\sigma_c^2) \\ N(0,\sigma_c^2) \end{bmatrix}_{4\times 1} \tag{3.28}$$

where the geolocation error is on average zero and is included in the augmented navigation state error vector $\delta\mathbf{x}$, while the associated variance is captured in the augmented covariance matrix $\mathbf{P}$. The following subsections present how the augmentation

for SLAM is accomplished for the three different methods: strictly INS drift/process noise error, strictly INS bias error, and combined INS drift and bias errors.

3.7.1 SLAM with INS Process Noise Only.

The errors associated with geolocating two ground features are augmented into the navigation state error. The augmented dynamics are as follows:

$$\boxed{\delta\mathbf{x}_{\mathbf{s}_{k+1}} = \mathbf{A}_{\mathbf{ds}} \cdot \delta\mathbf{x}_{\mathbf{s}_k} + \mathbf{\Gamma}_{\mathbf{cs}} \cdot \mathbf{w}_k} \tag{3.29}$$

where

$$\delta\mathbf{x}_{\mathbf{s}} = \begin{bmatrix} \delta\mathbf{x} \\ \\ \delta\mathbf{s} \end{bmatrix}_{13\times 1} \tag{3.30}$$

The state transition matrix $\mathbf{A}_{\mathbf{ds}}$ and the noise input matrix $\mathbf{\Gamma}_{\mathbf{cs}}$ account for the geolocation error and are augmented as follows:

$$\mathbf{A}_{\mathbf{ds}} = \begin{bmatrix} \mathbf{A}_{\mathbf{d}} & \mathbf{0}_{9\times 4} \\ \mathbf{0}_{4\times 9} & \mathbf{I}_4 \end{bmatrix}_{13\times 13} \tag{3.31}$$

$$\mathbf{\Gamma}_{\mathbf{cs}} = \begin{bmatrix} \mathbf{\Gamma}_{\mathbf{c}} \\ \\ \mathbf{0}_{4\times 6} \end{bmatrix}_{13\times 6} \tag{3.32}$$

The discrete-time random drift vector $\mathbf{w}_k$ is the same as presented before in (3.12). Since the INS initial alignment is assumed perfect, and the geolocation errors are on average zero, the augmented navigation state error vector is initialized with a vector of zeros as follows:

$$\delta\mathbf{x}_{\mathbf{s}_0} = \begin{bmatrix} \mathbf{0} \\ \vdots \\ \mathbf{0} \end{bmatrix}_{13\times 1} \tag{3.33}$$

and the associated covariance $\mathbf{P}_0$ is initialized according to the following equation:

$$\mathbf{P}_0 = \begin{bmatrix} \mathbf{0}_{9\times 9} & \mathbf{0}_{9\times 4} \\ \mathbf{0}_{4\times 9} & \mathbf{I}_4 \cdot \sigma_c^2 \end{bmatrix}_{13\times 13}$$

3.7.2 SLAM with INS Bias Errors Only.

The augmented navigation state error vector in (3.24) includes the INS bias errors. In this section, the state vector is augmented again to include the geolocation error vector $\delta\mathbf{s}$ as follows:

$$\boxed{\delta\mathbf{x}_{\mathbf{as}_{k+1}} = \mathbf{A}_{\mathbf{das}} \cdot \delta\mathbf{x}_{\mathbf{as}_k}} \tag{3.34}$$

The new augmented state transition matrix $\mathbf{A}_{\mathbf{das}}$ is as follows:

$$\mathbf{A}_{\mathbf{das}} = \begin{bmatrix} \mathbf{A}_{\mathbf{d}} & \mathbf{\Gamma}_{\mathbf{d}} & \mathbf{0}_{9\times4} \\ \mathbf{0}_{6\times9} & \mathbf{I}_6 & \mathbf{0}_{6\times4} \\ \mathbf{0}_{4\times9} & \mathbf{0}_{4\times6} & \mathbf{I}_4 \end{bmatrix}_{19\times19} \tag{3.35}$$

This augmented navigation state error vector is initialized with a vector of zeros because the error from the first nine states is assumed to be zero, the error from the six INS bias states is assumed to be on average zero, and the four states that track the geolocation error for the first two ground features is on average zero. This is expressed as follows:

$$\delta\mathbf{x}_{\mathbf{as}_0} = \begin{bmatrix} \mathbf{0} \\ \vdots \\ \mathbf{0} \end{bmatrix}_{19\times1} \tag{3.36}$$

The associated covariance is initialized according to the following equation:

$$\mathbf{P}_0 = \begin{bmatrix} \mathbf{0}_{9\times9} & \mathbf{0}_{9\times3} & \mathbf{0}_{9\times3} & \mathbf{0}_{9\times4} \\ \mathbf{0}_{3\times9} & \mathbf{I}_3 \cdot \sigma_{b_a}^2 & \mathbf{0}_{3\times3} & \mathbf{0}_{3\times4} \\ \mathbf{0}_{3\times9} & \mathbf{0}_{3\times3} & \mathbf{I}_3 \cdot \sigma_{b_g}^2 & \mathbf{0}_{3\times4} \\ \mathbf{0}_{3\times9} & \mathbf{0}_{3\times3} & \mathbf{0}_{3\times3} & \mathbf{I}_4 \cdot \sigma_c^2 \end{bmatrix}_{19\times19}$$

where the first nine entries represent the navigation state error and the uncertainty is zero because of perfect INS alignment. The next six entries represent the standard deviation of the accelerometers' and gyroscopes' biases. The last four entries represent the uncertainty in the camera measurements. This method of augmenting for geolocation error is applied again for the combined INS error scenario in Section 3.7.3.

3.7.3 SLAM with INS Drift and Bias Errors.

The augmented navigation state error equation in (3.14) includes the INS bias errors and the INS process noise errors. In this section, the geolocation state error $\delta\mathbf{s}$ is also augmented into the dynamics as follows:

$$\boxed{\delta\mathbf{x}_{\mathbf{as}k+1} = \mathbf{A}_{\mathbf{das}} \cdot \delta\mathbf{x}_{\mathbf{as}k} + \mathbf{\Gamma}_{\mathbf{cas}} \cdot \mathbf{w}_k} \tag{3.37}$$

where the process noise terms are simply added to the navigation state error equation from the previous section. The process noise input matrix $\mathbf{\Gamma}_{\mathbf{cas}}$ is augmented to account for the geolocation error as follows:

$$\mathbf{\Gamma}_{\mathbf{cas}} = \begin{bmatrix} \mathbf{\Gamma}_{\mathbf{c}} \\ \mathbf{0}_{10\times 6} \end{bmatrix}_{19\times 6} \tag{3.38}$$

where the zeros in (3.38) do not allow the random drift error vector $\mathbf{w}_k$ to influence the geolocation state error terms. The navigation state error vector and the associated covariance matrix are initialized as in Section 3.7.2.

3.8 The Kalman Filter

The Kalman filter algorithm optimally combines noise-corrupted bearing measurements from the camera with noise-corrupted accelerometer and gyroscope measurements, to determine an estimate of the INS navigation state error. The algorithm uses the Free INS navigation state error dynamics to propagate the navigation state error estimate $\widehat{\delta\mathbf{x}}^-$ for the next discrete time instant according to the system model. The algorithm then updates the estimate with the knowledge of the camera measurement $\mathbf{z}$ to determine an optimal estimate $\widehat{\delta\mathbf{x}}^+$ of the INS navigation state error. This optimal estimate is then subtracted from the Free INS calculated navigation state $\mathbf{x}_{\mathbf{c}}$ to determine an improved navigation state estimate $\widehat{\mathbf{x}}$. $\widehat{\mathbf{x}}$ is expressed as follows:

$$\widehat{\mathbf{x}} = \mathbf{x} + \delta\mathbf{x} - \widehat{\delta\mathbf{x}}^+ \tag{3.39}$$

The algorithm is illustrated in block diagram form in Figure 3.3.

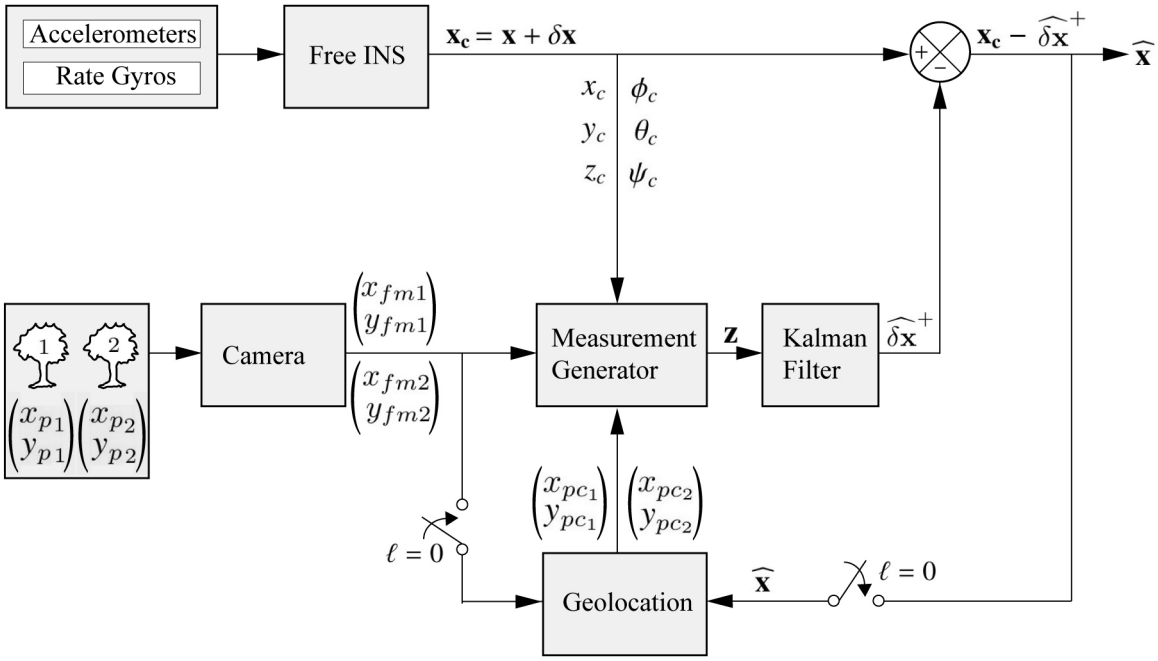

Figure 3.3: INS Aiding Using a Kalman Filter

During a measurement epoch, the Free INS error equations described in (3.29), (3.34), or (3.37) (according to the system being modeled) are updated using the measurement equation that follows:

$$\mathbf{z}_\ell = \mathbf{H}_\ell \cdot \delta\mathbf{x}_\ell + \mathbf{v}_\ell \tag{3.40}$$

where the subscript $\ell = 1, ..., L$ represents discrete instants of time within each epoch and L is the last measurement within that epoch. The optical measurement $\mathbf{z}_\ell$ at time instant ℓ is related to the navigation state error $\delta\mathbf{x}$ through the observation matrix $\mathbf{H}$ plus the measurement error $\mathbf{v}$. The measurement error is a white Gaussian sequence with a covariance $\mathbf{R}$ expressed as follows:

$$\mathbf{R} = \begin{bmatrix} \sigma_c^2 & 0 & 0 & 0 \\ 0 & \sigma_c^2 & 0 & 0 \\ 0 & 0 & \sigma_c^2 & 0 \\ 0 & 0 & 0 & \sigma_c^2 \end{bmatrix} \tag{3.41}$$

Calculation of σ_c is based on the measurements in the camera's focal plane having a one pixel error. Therefore, the camera's aspect ratio of one and its resolution (MP count)

determine the standard deviation σ_c of the camera, calculated as follows:

$$\sigma_c = \sqrt{\frac{1}{\#\,\mathrm{MP}} \cdot 10^{-6}} \tag{3.42}$$

where $\#MP$ is the resolution of the camera.

The 4×1 measurement vector $\mathbf{z}_\ell$ contains the measurements of the geolocated ground features in the two dimensional x and y plane, relative to the position of the aircraft. The first and second measurement terms relate to the first ground feature's (x, y) position and the third and fourth measurement terms relate to the second ground feature's (x, y) position. These measurements are best explained by relating the measurement d_ℓ in the two dimensional illustration in Figure 2.10, where the bearing measurement provides the position of the aircraft relative to the position of the ground feature.

The measurement vector $\mathbf{z}_\ell$ is derived from the geolocated ground feature measurements at the beginning of each epoch, the Free INS measurements from the beginning of the navigation, and the optical measurements in the focal plane of the geolocated ground features throughout each epoch. Measurement vector $\mathbf{z}_\ell$ is developed from the LHS of (2.22) and (2.23) as follows:

$$\mathbf{z}_\ell = \begin{bmatrix} x_{pc_1} - x_{c_k} - z_{c_k}\left(x_{fm1_\ell} - \theta_{c_k}(1 + x_{fm1_\ell}^2) + \phi_{c_k} \cdot x_{fm1_\ell} \cdot y_{fm1_\ell} - \psi_{c_k} \cdot y_{fm1_\ell}\right) \\ y_{pc_1} - y_{c_k} - z_{c_k}\left(y_{fm1_\ell} - \theta_{c_k} \cdot x_{fm1_\ell} \cdot y_{fm1_\ell} + \phi_{c_k}(1 + y_{fm1_\ell}^2) + \psi_{c_k} \cdot x_{fm1_\ell}\right) \\ x_{pc_2} - x_{c_k} - z_{c_k}\left(x_{fm2_\ell} - \theta_{c_k}(1 + x_{fm2_\ell}^2) + \phi_{c_k} \cdot x_{fm2_\ell} \cdot y_{fm2_\ell} - \psi_{c_k} \cdot y_{fm2_\ell}\right) \\ y_{pc_2} - y_{c_k} - z_{c_k}\left(y_{fm2_\ell} - \theta_{c_k} \cdot x_{fm2_\ell} \cdot y_{fm2_\ell} + \phi_{c_k}(1 + y_{fm2_\ell}^2) + \psi_{c_k} \cdot x_{fm2_\ell}\right) \end{bmatrix}_{4\times 1} \tag{3.43}$$

where the geolocated ground feature measurements, (x_{pc_1}, y_{pc_1}, x_{pc_2}, and y_{pc_2}) remain constant throughout each measurement epoch n, because the tracked ground features are stationary. These measurement values are presented in Table 3.5 for the first epoch where the position of the aircraft is initially known exactly and the only error in geolocation is

from the camera measurement. However, the geolocated ground feature measurements for the remaining epochs are established from the aided (corrected) INS-provided aircraft position and the camera measurement of the ground features. The INS-calculated navigation state values are drawn directly from the Free INS according to Table 3.4 for the one hour flight. The camera measurements in the focal plane (x_{fm1_ℓ}, y_{fm1_ℓ}, x_{fm2_ℓ}, and y_{fm2_ℓ}) include the error from the camera and are taken throughout each epoch at each discrete time instant ℓ. These camera measurements are iterated according to ℓ and are calculated as in Table 3.6, where ζ is the error from the camera measurement drawn randomly according to the Gaussian distribution, $N(0,\ \sigma_c^2)$. The calculations embodied in (3.40) and (3.43) are represented in the block labeled "Measurement Generator" in Figure 3.3.

Table 3.6: Pixel measurements in focal plane over time for the 1^{st} and 2^{nd} ground features

time	x_{fm} for 1^{st}	y_{fm} for 1^{st}	x_{fm} for 2^{nd}	y_{fm} for 2^{nd}
$\ell = 0$	$x_{fm_{1_0}} = 1.0 + \zeta$	$y_{fm_{1_0}} = 0 + \zeta$	$x_{fm_{2_0}} = 2.0 + \zeta$	$y_{fm_{2_0}} = 0 + \zeta$
$\ell = 1$	$x_{fm_{1_1}} = 0.9 + \zeta$	$y_{fm_{1_1}} = 0 + \zeta$	$x_{fm_{2_1}} = 1.9 + \zeta$	$y_{fm_{2_1}} = 0 + \zeta$
$\vdots$	$\vdots$	$\vdots$	$\vdots$	$\vdots$
$\ell = 9$	$x_{fm_{1_9}} = 0.1 + \zeta$	$y_{fm_{1_9}} = 0 + \zeta$	$x_{fm_{2_9}} = 1.1 + \zeta$	$y_{fm_{2_9}} = 0 + \zeta$
$\ell = 10$	$x_{fm_{1_{10}}} = 0.0 + \zeta$	$y_{fm_{1_{10}}} = 0$	$x_{fm_{2_{10}}} = 1.0 + \zeta$	$y_{fm_{2_{10}}} = 0 + \zeta$

The observation matrix $\mathbf{H}_\ell$ is a 4×9 matrix, which relates the optical measurements in the focal frame to the navigation state error vector shown in (3.5) in the navigation frame. It is augmented according to the specific navigation state error vector configuration being considered. The observation matrix is generated using the RHS of (2.22) and (2.23) for both ground features' bearing measurements. The first and second rows relate to the first ground feature's x and y coordinates and the third and fourth rows relate to the second

ground feature's x and y coordinates. $\mathbf{H}_\ell$ is as follows:

$$\mathbf{H}_\ell = \begin{bmatrix} -1 & 0 & -x_{f1_\ell} & 0 & 0 & 0 & -x_{f1_\ell} \cdot y_{f1_\ell} & 1 + x_{f1_\ell}^2 & y_{f1_\ell} \\ 0 & -1 & -y_{f1_\ell} & 0 & 0 & 0 & -(1 + y_{f1_\ell}^2) & x_{f1_\ell} \cdot y_{f1_\ell} & -x_{f1_\ell} \\ -1 & 0 & -x_{f2_\ell} & 0 & 0 & 0 & -x_{f2_\ell} \cdot y_{f2_\ell} & 1 + x_{f2_\ell}^2 & y_{f2_\ell} \\ 0 & -1 & -y_{f2_\ell} & 0 & 0 & 0 & -(1 + y_{f2_\ell}^2) & x_{f2_\ell} \cdot y_{f2_\ell} & -x_{f2_\ell} \end{bmatrix}_{4\times 9} \tag{3.44}$$

Since the aircraft is moving in the positive x direction, and in the first measurement epoch the ground features are located at 1000 and 2000 meters in the positive x direction, the x_{f1_ℓ} and x_{f2_ℓ} non-dimensional measurements in the camera's focal plane are initially recorded as one and two. These recorded measurements decrease relative to the aircraft's constant forward velocity. Therefore, the tracked ground features' x-direction pixel location values decrease, while y-direction pixel location values remain at zero according to Table 3.7 throughout each epoch.

Table 3.7: Pixel values in observation matrix over time for the 1^{st} and 2^{nd} ground features

time	x_f for 1^{st}	y_f for 1^{st}	x_f for 2^{nd}	y_f for 2^{nd}
$\ell = 0$	$x_{f_{1_0}} = 1.0$	$y_{f_{1_0}} = 0$	$x_{f_{2_0}} = 2.0$	$y_{f_{2_0}} = 0$
$\ell = 1$	$x_{f_{1_1}} = 0.9$	$y_{f_{1_1}} = 0$	$x_{f_{2_1}} = 1.9$	$y_{f_{2_1}} = 0$
$\vdots$	$\vdots$	$\vdots$	$\vdots$	$\vdots$
$\ell = 9$	$x_{f_{1_9}} = 0.1$	$y_{f_{1_9}} = 0$	$x_{f_{2_9}} = 1.1$	$y_{f_{2_9}} = 0$
$\ell = 10$	$x_{f_{1_{10}}} = 0.0$	$y_{f_{1_{10}}} = 0$	$x_{f_{2_{10}}} = 1.0$	$y_{f_{2_{10}}} = 0$

3.8.1 Kalman Filter with only INS Drift Error.

This section presents the equations used to propagate and update the navigation state error estimate of the Free INS with only process noise errors. The recursive KF algorithm begins by initializing a loop in each measurement epoch when $\ell = 0$ and when the two ground features are geolocated. Since it is assumed that the INS alignment is perfect in the

first measurement epoch ($n = 1$), the KF is initialized using the following equation:

$$\left(\widehat{\delta \mathbf{x}_{\mathbf{s}0}}^{+}\right)^{n=1} = \begin{bmatrix} \mathbf{0} \\ \vdots \\ \mathbf{0} \end{bmatrix}_{13\times 1} \tag{3.45}$$

where the superscript plus sign indicates that it is an optimal estimate of the navigation state error. The four geolocation error estimates are on average zero. The product of the optimal state estimate and the state transition matrix $\mathbf{A_{ds}}$ provides a propagated navigation state error estimate $\widehat{\delta \mathbf{x}}^{-}$ for the next discrete-time instant, as follows:

$$\widehat{\delta \mathbf{x}_{\mathbf{s}\ell+1}}^{-} = \mathbf{A_{ds}} \cdot \widehat{\delta \mathbf{x}_{\mathbf{s}\ell}}^{+} \tag{3.46}$$

where the superscript minus sign indicates that it is before the camera measurements have been received.

The uncertainty in the KF navigation state error estimates are captured in the covariance matrix $\mathbf{P}_\ell$ for each discrete time iteration ℓ. The initial covariance matrix $\mathbf{P}_0^+$ describes the confidence in the initial alignment and describes the navigation state error estimate in (3.45) where the superscript plus sign indicates that it is the covariance of the optimal navigation state error estimate.

In order to maintain consistency with [4], the uncertainty in position at the beginning of the navigation scenario is assumed to be one meter, while the uncertainty in velocity is assumed to be 10^{-3} z mm/s, and the uncertainty in the aircraft attitude is assumed to be 20 arc seconds. Thus, the non-dimensional navigation state error covariance values are as follows:

$$\begin{aligned}
\delta \mathbf{P_x},\ \ \delta \mathbf{P_y},\ \ \delta \mathbf{P_z} &\sim N\left(\mathbf{0}_{3\times 1},\ 1 \times 10^{-6} \cdot I_3\right) \\
\delta \mathbf{V_x},\ \ \delta \mathbf{V_y},\ \ \delta \mathbf{V_z} &\sim N\left(\mathbf{0}_{3\times 1},\ 1 \times 10^{-16} \cdot I_3\right) \\
\delta \mathbf{\Psi}_\phi,\ \ \delta \mathbf{\Psi}_\theta,\ \ \delta \mathbf{\Psi}_\psi &\sim N\left(\mathbf{0}_{3\times 1},\ 1 \times 10^{-8} \cdot I_3\right)
\end{aligned}$$

The initial covariance matrix for the KF also includes the covariance of the geolocation error terms described in (3.28) as $N(0,\ \sigma_c^2)$, which is unique for the initialization of the first epoch. The initialization of the following epochs is discussed in Section 3.9. The KF initial state covariance matrix $\mathbf{P}_0^+$ is as follows:

$$\mathbf{P}_0^+ = \begin{bmatrix} \mathbf{I}_3 \cdot 10^{-6} & \mathbf{0} & \mathbf{0} & \mathbf{0} \\ \mathbf{0} & \mathbf{I}_3 \cdot 10^{-16} & \mathbf{0} & \mathbf{0} \\ \mathbf{0} & \mathbf{0} & \mathbf{I}_3 \cdot 10^{-8} & \mathbf{0} \\ \mathbf{0} & \mathbf{0} & \mathbf{0} & \mathbf{I}_4 \cdot \sigma_c^2 \end{bmatrix}_{13\times 13} \tag{3.47}$$

The propagated KF covariance of the navigation state error estimate at time instant $(\ell + 1)$ is calculated by solving the Lyapunov equation, as follows:

$$\mathbf{P}_{\ell+1}^- = \mathbf{A_{ds}} \cdot \mathbf{P}_\ell^+ \cdot \mathbf{A_{ds}}^T + \mathbf{\Gamma_{cs}} \cdot \mathbf{Q_d} \cdot \mathbf{\Gamma_{cs}}^T \tag{3.48}$$

where the superscript minus sign indicates that it is the covariance of the suboptimal navigation state error estimate and is calculated according to the following:

$$E\left\{\left(\delta\mathbf{x} - \widehat{\delta\mathbf{x}}_{\ell+1}^-\right)\left(\delta\mathbf{x} - \widehat{\delta\mathbf{x}}_{\ell+1}^-\right)\right\} \tag{3.49}$$

The Kalman gain $\mathbf{K}_{\ell+1}$ is calculated as follows:

$$\mathbf{K}_{\ell+1} = \mathbf{P}_{\ell+1}^- \cdot \mathbf{H}_{\mathbf{s}\ell+1}^T (\mathbf{H}_{\mathbf{s}\ell+1} \cdot \mathbf{P}_{\ell+1}^- \cdot \mathbf{H}_{\mathbf{s}\ell+1}^T + \mathbf{R})^{-1} \tag{3.50}$$

where the observation matrix $\mathbf{H}$ in (3.44) is augmented to account for the geolocation error terms as follows:

$$\mathbf{H}_{\mathbf{s}\ell} = \begin{bmatrix} \mathbf{H}_{4\times 9} & \mathbf{I}_4 \end{bmatrix}_{4\times 13} \tag{3.51}$$

Through this augmentation, the geolocation error terms in (3.28) directly enter the measurement equation ($\mathbf{z} = \mathbf{H} \cdot \delta\mathbf{x_s} + \mathbf{v}$). The Kalman gain is then used to establish the navigation state error estimate $\widehat{\delta\mathbf{x}_{\mathbf{s}\ell+1}}^+$ for the discrete time instant $\ell + 1$, after the measurement $\mathbf{z}_{\ell+1}$ has been received.

An update to the navigation state error estimate, $\widehat{\delta \mathbf{x}_{\mathbf{s}_{\ell+1}}}^{-}$ occurs when the measurement $\mathbf{z}$ from the optical sensor has been received. The optimal navigation state error estimate $\widehat{\delta \mathbf{x}_{\mathbf{s}_{\ell+1}}}^{+}$ is determined according to the following equation:

$$\widehat{\delta \mathbf{x}_{\mathbf{s}_{\ell+1}}}^{+} = \widehat{\delta \mathbf{x}_{\mathbf{s}_{\ell+1}}}^{-} + \mathbf{K}_{\ell+1}\left(\mathbf{z}_{\ell+1} - \mathbf{H}_{\mathbf{s}_{\ell+1}} \cdot \widehat{\delta \mathbf{x}_{\mathbf{s}_{\ell+1}}}^{-}\right) \tag{3.52}$$

The covariance $\mathbf{P}^{+}_{\ell+1}$ of the estimation error for the navigation state error at time $\ell + 1$ is calculated as follows:

$$\mathbf{P}^{+}_{\ell+1} = \left(\mathbf{I}_{13} - \mathbf{K}_{\ell+1} \cdot \mathbf{H}_{\mathbf{s}_{\ell+1}}\right)\mathbf{P}^{-}_{\ell+1} \tag{3.53}$$

The recursive loop starts over by propagating with (3.46) and (3.48). This loop continues until time $\ell = 10 = L$. After $L = 10$, the first ground feature is no longer in the camera's FOV and a new ground feature must be geolocated.

3.8.2 Kalman Filter with only INS Bias Error.

This section presents the equations used to propagate and update the navigation state error estimate for the Free INS model with only bias noise errors. The algorithm is the same as presented in Section 3.8.1, however the augmentation of the bias terms into the state transition matrix must be handled differently. As with the previous algorithm, the recursive loop begins when the ground features are geolocated and the INS is aligned with the external navigation source and thus provides an optimal navigation state error estimate $\widehat{\delta \mathbf{x}}^{+}$ as follows:

$$\left(\widehat{\delta \mathbf{x}_{\mathbf{as}_0}}^{+}\right)^{n=1} = \begin{bmatrix} \mathbf{0} \\ \vdots \\ \mathbf{0} \end{bmatrix}_{19\times 1} \tag{3.54}$$

where the nine navigation state error estimates are aligned with the external navigation source and said to be zero, the six bias error estimates are on average zero, and the four geolocation error estimates are on average zero. The navigation state error estimates are propagated with the state transition matrix which accounts for the bias terms according to

the following equation:

$$\widehat{\delta \mathbf{x}_{\mathbf{as}_{\ell+1}}}^{-} = \mathbf{A}_{\mathbf{das}} \cdot \widehat{\delta \mathbf{x}_{\mathbf{as}_{\ell}}}^{+} \tag{3.55}$$

The initial covariance matrix $\mathbf{P}_0^+$ for the bias error model will be the same as with the drift error model in (3.47), except it will include the covariance for the bias terms as shown in the following equation:

$$\mathbf{P}_0^+ = \begin{bmatrix} \mathbf{I}_3 \cdot 10^{-6} & \mathbf{0} & \mathbf{0} & \mathbf{0} & \mathbf{0} & \mathbf{0} \\ \mathbf{0} & \mathbf{I}_3 \cdot 10^{-16} & \mathbf{0} & \mathbf{0} & \mathbf{0} & \mathbf{0} \\ \mathbf{0} & \mathbf{0} & \mathbf{I}_3 \cdot 10^{-8} & \mathbf{0} & \mathbf{0} & \mathbf{0} \\ \mathbf{0} & \mathbf{0} & \mathbf{0} & \mathbf{I}_3 \cdot \sigma_{b_a}^2 & \mathbf{0} & \mathbf{0} \\ \mathbf{0} & \mathbf{0} & \mathbf{0} & \mathbf{0} & \mathbf{I}_3 \cdot \sigma_{b_g}^2 & \mathbf{0} \\ \mathbf{0} & \mathbf{0} & \mathbf{0} & \mathbf{0} & \mathbf{0} & \mathbf{I}_4 \cdot \sigma_c^2 \end{bmatrix}_{19\times19} \tag{3.56}$$

It is propagated for time instant $\ell + 1$ with the state transition matrix according to the following equation:

$$\mathbf{P}_{\ell+1}^- = \mathbf{A}_{\mathbf{das}} \cdot \mathbf{P}_{\ell}^+ \cdot \mathbf{A}_{\mathbf{das}}{}^T \tag{3.57}$$

The Kalman gain $\mathbf{K}_{\ell+1}$ is calculated the same as in Section 3.8.1, as shown in the following equation:

$$\mathbf{K}_{\ell+1} = \mathbf{P}_{\ell+1}^- \cdot \mathbf{H}_{\mathbf{as}\ell+1}^T (\mathbf{H}_{\mathbf{as}\ell+1} \cdot \mathbf{P}_{\ell+1}^- \cdot \mathbf{H}_{\mathbf{as}\ell+1}^T + \mathbf{R})^{-1} \tag{3.58}$$

however, the observation matrix $\mathbf{H}$ in (3.44) is augmented to exclude the bias error terms and include geolocation error terms as follows:

$$\mathbf{H}_{\mathbf{as}\ell} = \begin{bmatrix} \mathbf{H}_{4\times9} & \mathbf{0}_{4\times6} & \mathbf{I}_4 \end{bmatrix}_{4\times19} \tag{3.59}$$

where the bias error terms in the navigation state error vector $\delta \mathbf{x}_{\mathbf{as}\ell}$ do not impact the error from the camera measurement $\mathbf{z}$. The geolocation error terms on the other hand directly influence $\mathbf{z}$.

The Kalman gain is then used to establish the navigation state error estimate $\widehat{\delta\mathbf{x}_{\mathbf{as}_{\ell+1}}}^{+}$ for the next discrete instant after the measurement $\mathbf{z}$ has been received.

An update to the navigation state error estimate $\widehat{\delta\mathbf{x}_{\mathbf{as}_{\ell+1}}}^{-}$ occurs when measurement $\mathbf{z}$ from the optical sensor has been received. The optimal estimate $\widehat{\delta\mathbf{x}_{\mathbf{as}_{\ell+1}}}^{+}$ is determined using the following equation:

$$\widehat{\delta\mathbf{x}_{\mathbf{as}_{\ell+1}}}^{+} = \widehat{\delta\mathbf{x}_{\mathbf{as}_{\ell+1}}}^{-} + \mathbf{K}_{\ell+1}\left(\mathbf{z}_{\ell+1} - \mathbf{H}_{\mathbf{as}_{\ell+1}} \cdot \widehat{\delta\mathbf{x}_{\mathbf{as}_{\ell+1}}}^{-}\right) \tag{3.60}$$

The covariance $\mathbf{P}^{+}_{\ell+1}$ for the optimal estimate at time $\ell + 1$ is calculated as follows:

$$\mathbf{P}^{+}_{\ell+1} = \left(\mathbf{I}_{19} - \mathbf{K}_{\ell+1} \cdot \mathbf{H}_{\mathbf{as}_{\ell+1}}\right)\mathbf{P}^{-}_{\ell+1} \tag{3.61}$$

The recursive loop starts over by propagating with (3.55) and (3.57). This loop continues until the first ground feature is no longer in the camera's FOV and a new ground feature is geolocated at time L.

3.8.3 Kalman Filter with Both INS Error Sources.

This section presents the equations used to propagate and update the navigation state error estimate for the Free INS model with both sensor drift errors and sensor bias errors. This is simply a combination of Sections 3.8.1 and 3.8.2 . The initial conditions are drawn from (3.54) and (3.56). The recursive equations are presented in Figure 3.4.

3.9 Transitioning from epoch n to epoch $n + 1$

At the beginning of navigation the aircraft navigation state is perfectly known and consequently the navigation state error associated with a perfect alignment is zero. At the very instant the alignment is established, the aircraft camera geolocates two ground features. Their measurements(x_{pc_1}, y_{pc_1}, x_{pc_2}, and y_{pc_2}) are established in (3.28) and remain constant throughout the first measurement epoch. They are used in the KF measurement vector $\mathbf{z}$ in (3.40) to establish bearing measurements which are used to ultimately aid the INS courtesy of the KF algorithm.

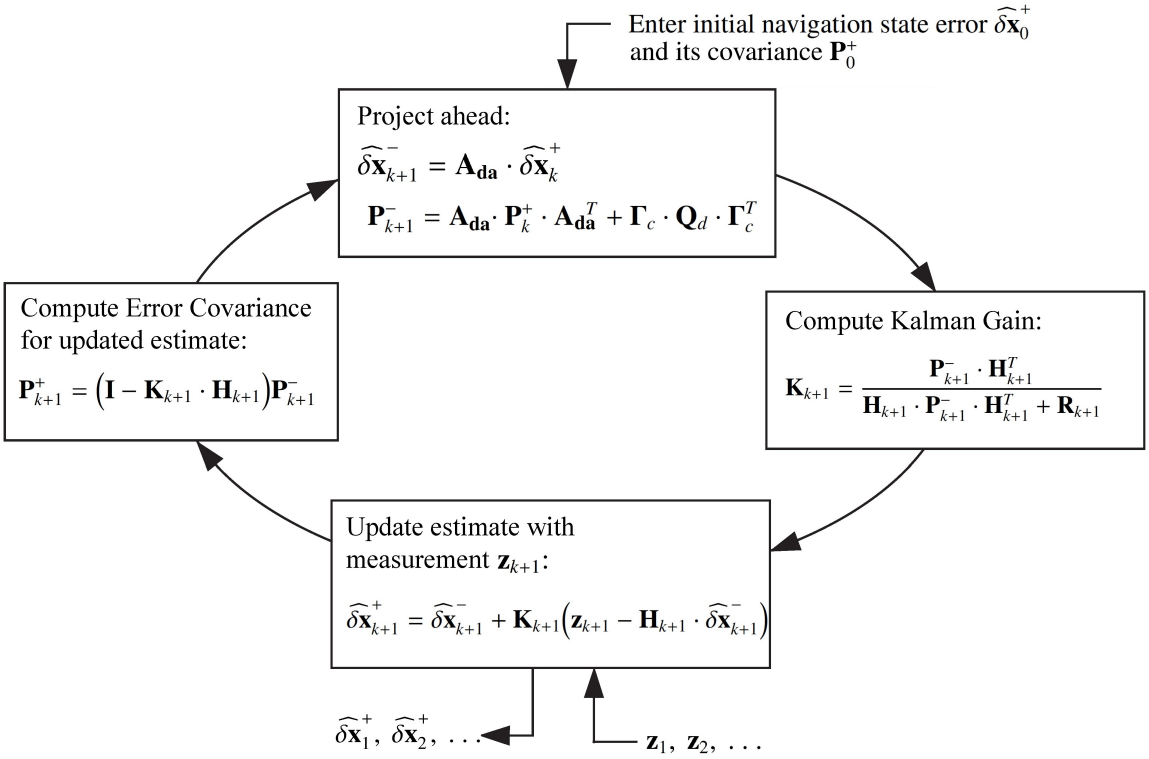

Figure 3.4: Linear Kalman Filter Recursive Loop

At the completion of the first epoch, the first ground feature (whose coordinates are x_{pc_1} and y_{pc_1}) is no longer in the camera's FOV and the coordinate measurements are discarded. Simultaneously, x_{pc_2} and y_{pc_2} are transitioned to be tracked as the new first ground feature, whose coordinates are x_{pc_1} and y_{pc_1} in the new measurement epoch $n + 1$. This new measurement epoch is marked by the geolocation of a new ground feature that replaces x_{pc_2} and y_{pc_2} of the previous epoch n. This is illustrated in Figure 3.5 where the y coordinate is not shown.

The aircraft's corrected navigation state $\widehat{\mathbf{x}}$ is used to establish the location of the new ground feature and thus initializes the next epoch $n + 1$ at time $\ell = 0$. The ground feature measurements for this new epoch are derived from (2.16) and (2.17) utilizing the

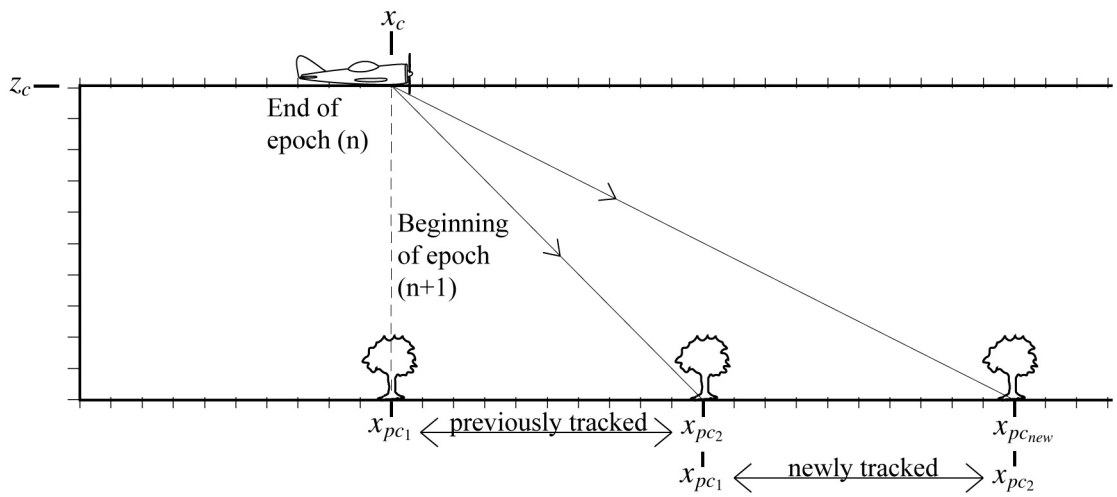

Figure 3.5: Transition from Epoch n to Epoch $n+1$

improved navigation state estimate $\widehat{\mathbf{x}}$ as follows:

$$
\begin{aligned}
x_{pc_1}^{n+1} &= x_{pc_2}^{n} \\
y_{pc_1}^{n+1} &= y_{pc_2}^{n} \\
x_{pc_2}^{n+1} &= \left(x_{c_L} - \widehat{\delta x}_L\right) + \left(z_{c_L} - \widehat{\delta z}_L\right)\frac{x_{fm2_0} - \left(\psi_{c_L} - \widehat{\delta\psi}_L\right)y_{fm2_0} - \left(\theta_{c_L} - \widehat{\delta\theta}_L\right)}{1 + \left(\theta_{c_L} - \widehat{\delta\theta}_L\right)x_{fm2_0} - \left(\phi_{c_L} - \widehat{\delta\phi}_L\right)y_{fm2_0}} \\
y_{pc_2}^{n+1} &= \left(y_{c_L} - \widehat{\delta y}_L\right) + \left(z_{c_L} - \widehat{\delta z}_L\right)\frac{y_{fm2_0} + \left(\psi_{c_L} - \widehat{\delta\psi}_L\right)x_{fm2_0} + \left(\phi_{c_L} - \widehat{\delta\phi}_L\right)}{1 + \left(\theta_{c_L} - \widehat{\delta\theta}_L\right)x_{fm2_0} - \left(\phi_{c_L} - \widehat{\delta\phi}_L\right)y_{fm2_0}}
\end{aligned}
\tag{3.62}
$$

where the terms with a hat are KF estimates of the specific navigation state error components. These estimates are subtracted from their corresponding Free INS outputs, indicated with a subscript c_L where L indicates the last measurement of the previous epoch. This provides the corrected navigation state, which is used with the x_f and y_f camera measurements in the focal plane during geolocation of the new ground feature. These focal plane measurement values for the second ground feature at instant $\ell = 0$ are presented in Table 3.6 and again as follows for convenience:

$$
x_{fm_{2_0}} = 2.0 + \zeta \qquad\qquad y_{fm_{2_0}} = 0 + \zeta
$$

where $\zeta \sim N(0,\ \sigma_c^2)$. The geolocated measurements x_{pc_1}, y_{pc_1}, x_{pc_2}, and y_{pc_2} are used in the calculations for the KF measurement $\mathbf{z}$ and remain constant throughout epoch $n+1$. The associated geolocation error values (δx_{pc_2} and δy_{pc_2}) for the new ground feature have a mean of zero and a covariance which is calculated using the matrix $\mathbf{M}$.

The matrix $\mathbf{M}$ is derived from the measurement equations (2.22) and (2.23) that follow:

$$x_{pc} - x_c - z_c\Big(x_{fm} - \theta_c(1+x_{fm}^2) + \phi_c \cdot x_{fm} \cdot y_{fm} - \psi_c \cdot y_{fm}\Big) = \\ - \delta x - \delta z \cdot x_f - \delta\phi \cdot x_f \cdot y_f + \delta\theta(1 + x_f^2) + \delta\psi \cdot y_f + \delta x_{pc} - \delta x_f$$

$$y_{pc} - y_c - z_c\Big(y_{fm} - \theta_c \cdot x_{fm} \cdot y_{fm} + \phi_c(1 + y_{fm}^2) + \psi_c \cdot x_{fm}\Big) = \\ - \delta y - \delta z \cdot y_f - \delta\phi(1 + y_f^2) + \delta\theta \cdot x_f \cdot y_f - \delta\psi \cdot x_f + \delta y_{pc} - \delta y_f$$

The KF measurement equation in state space form is as follows:

$$\mathbf{z} = \mathbf{H} \cdot \delta\mathbf{x} + \mathbf{v}$$

where the vector $\mathbf{z}$ contains the input measurement values from the camera. These measurement values are calculated with the LHS of (2.22) and (2.23), so, the input measurements $\mathbf{z}_2$ for the second ground feature are as follows:

$$\mathbf{z}_2 = \begin{bmatrix} \boxed{x_{pc_2}} - x_c - z_c\Big(x_{fm_2} - \theta_c(1 + x_{fm_2}^2) + \phi_c \cdot x_{fm_2} \cdot y_{fm_2} - \psi_c \cdot y_{fm_2}\Big) \\ \boxed{y_{pc_2}} - y_c - z_c\Big(y_{fm_2} - \theta_c \cdot x_{fm_2} \cdot y_{fm_2} + \phi_c(1 + y_{fm_2}^2) + \psi_c \cdot x_{fm_2}\Big) \end{bmatrix}_{2\times 1}$$

The new geolocated measurements (x_{pc} and y_{pc}) are derived in (3.62) for epoch $n+1$. The associated variance of these measurements is extracted from the RHS of (2.22) and (2.23). The RHS contains all the error terms for the measurement equation and accounts for the deviation from the true measurements of the LHS. This is equal to the RHS of the state space measurement equation, therefore the following is true:

$$\mathbf{H} \cdot \delta\mathbf{x} + \mathbf{v} = \begin{matrix} -\delta x - \delta z \cdot x_f - \delta\phi \cdot x_f \cdot y_f + \delta\theta(1 + x_f^2) + \delta\psi \cdot y_f + \delta x_{pc} - \delta x_f \\ -\delta y - \delta z \cdot y_f - \delta\phi(1 + y_f^2) + \delta\theta \cdot x_f \cdot y_f - \delta\psi \cdot x_f + \delta y_{pc} - \delta y_f \end{matrix}$$

where the KF estimates of the measurement error are contained in $\delta\mathbf{x}$. This is better presented as follows:

$$\mathbf{H}\cdot\widehat{\delta\mathbf{x}}+\mathbf{v}=\begin{matrix}-\widehat{\delta x}-\widehat{\delta z}\cdot x_f-\widehat{\delta\phi}\cdot x_f\cdot y_f+\widehat{\delta\theta}(1+x_f^2)+\widehat{\delta\psi}\cdot y_f+\boxed{\widehat{\delta x_{pc}}}-\boxed{\delta x_f}\\ -\widehat{\delta y}-\widehat{\delta z}\cdot y_f-\widehat{\delta\phi}(1+y_f^2)+\widehat{\delta\theta}\cdot x_f\cdot y_f-\widehat{\delta\psi}\cdot x_f+\boxed{\widehat{\delta y_{pc}}}-\boxed{\delta y_f}\end{matrix}$$

where $\mathbf{v}$ accounts for the variance of the camera measurements in the focal plane (δx_f and δy_f) and has a covariance of $\mathbf{R}$. The KF's covariance $\mathbf{P}$ accounts for the remaining terms. Therefore, the covariance of the geolocation error term ($\widehat{\delta x}_{pc}$ and $\widehat{\delta y}_{pc}$) can be isolated from the navigation error state terms as follows:

$$\begin{aligned}\boxed{\widehat{\delta x_{pc}}}&=\widehat{\delta x}+\widehat{\delta z}\cdot x_f+\widehat{\delta\phi}\cdot x_f\cdot y_f-\widehat{\delta\theta}(1+x_f^2)-\widehat{\delta\psi}\cdot y_f+\delta x_f\\ \boxed{\widehat{\delta y_{pc}}}&=\widehat{\delta y}+\widehat{\delta z}\cdot y_f+\widehat{\delta\phi}(1+y_f^2)-\widehat{\delta\theta}\cdot x_f\cdot y_f+\widehat{\delta\psi}\cdot x_f+\delta y_f\end{aligned}\tag{3.63}$$

Recall the following:

$$\widehat{\delta\mathbf{x}}=\begin{bmatrix}\widehat{\delta x},&\widehat{\delta y},&\widehat{\delta z},&\widehat{\delta v_x},&\widehat{\delta v_y},&\widehat{\delta v_z},&\widehat{\delta\phi},&\widehat{\delta\theta},&\widehat{\delta\psi}\end{bmatrix}^T$$

Furthermore, the matrix $\mathbf{M}$ is extracted from (3.63) and is the inverse of the observation matrix $\mathbf{H}$ as follows:

$$\mathbf{M}=\begin{bmatrix}1&0&x_f&0&0&0&x_f\cdot y_f&-(1+x_f^2)&-y_f\\ 0&1&y_f&0&0&0&(1+y_f^2)&-x_f\cdot y_f&x_f\end{bmatrix}_{2\times9}$$

where x_f and y_f measurements are for the new geolocated ground feature at $\ell=0$ in epoch $n+1$. Therefore, $x_f=2$, and $y_f=0$ and matrix $\mathbf{M}$ is as follows:

$$\mathbf{M}=\begin{bmatrix}1&0&2&0&0&0&0&-5&0\\ 0&1&0&0&0&0&1&0&2\end{bmatrix}_{2\times9}\tag{3.64}$$

where

$$\begin{bmatrix}\delta x_{pc}\\ \delta y_{pc}\end{bmatrix}=\mathbf{M}\cdot\delta\mathbf{x}+\begin{bmatrix}\delta x_f\\ \delta y_f\end{bmatrix}\tag{3.65}$$

The matrix **M** is used to calculate the covariance of the new geolocated ground feature measurements, which is then combined with the KF covariance matrix **P** during the transition between epochs. The following subsections present the transition of the navigation state error terms and the associated covariance for each of the three INS system error models.

3.9.1 Transitioning from epoch n to epoch $n+1$ with INS Drift Errors Only.

This section develops the transition for the INS system with only random drift errors. The KF's optimal estimate of the navigation state error $\left(\widehat{\delta\mathbf{x}}_{\mathbf{s}}^{+}\right)_{L}^{n}$ at the end of epoch n is transitioned to epoch $n+1$ according to the following:

$$\left(\widehat{\delta\mathbf{x}}_{\mathbf{s}}^{+}\right)_{L}^{n} = \begin{bmatrix} \widehat{\delta\mathbf{x}}_{9\times1} \\ \widehat{\delta x}_{pc_1} \\ \widehat{\delta y}_{pc_1} \\ \widehat{\delta x}_{pc_2} \\ \widehat{\delta y}_{pc_2} \end{bmatrix}_{13\times1} \quad \Rightarrow \quad \left(\widehat{\delta\mathbf{x}}_{\mathbf{s}}^{+}\right)_{0}^{n+1} = \begin{bmatrix} \widehat{\delta\mathbf{x}}_{9\times1} \\ \widehat{\delta x}_{pc_2} \\ \widehat{\delta y}_{pc_2} \\ 0 \\ 0 \end{bmatrix}_{13\times1} \tag{3.66}$$

where the nine error state estimates remain the same. The geolocation error estimates for the first ground feature ($\widehat{\delta x}_{pc_1}$ and $\widehat{\delta y}_{pc_1}$) in epoch n are discarded because the ground feature is no longer in the camera's FOV. However, the geolocation error estimates for the second ground feature ($\widehat{\delta x}_{pc_2}$ and $\widehat{\delta y}_{pc_2}$) in epoch n are transitioned to the first ground feature position for epoch $n+1$. The newly acquired ground feature error estimates are set equal to zero because they are on average zero with a covariance derived from the previous epoch's navigation state error covariance plus the camera measurement error covariance.

The covariance $\left(\mathbf{P}^{+}\right)_{L}^{n}$ of the navigation state error estimates for the last camera measurement L at the end of epoch n is as follows:

$$\left(\mathbf{P}^{+}\right)_{L}^{n} = \left[\begin{array}{c|c|c|c|c} \mathbf{P}\left(\widehat{\delta\mathbf{x}}\right)_{9\times9} & \bullet & \bullet & \bullet & \bullet \\ \hline \bullet & P\left(\delta x_{pc_1}\right) & \bullet & \bullet & \bullet \\ \bullet & \bullet & P\left(\delta y_{pc_1}\right) & \bullet & \bullet \\ \hline \bullet & \bullet & \bullet & P\left(\delta x_{pc_2}\right) & \bullet \\ \bullet & \bullet & \bullet & \bullet & P\left(\delta y_{pc_2}\right) \end{array}\right]_{13\times13} \tag{3.67}$$

where the (•) are place-holders representing the covariance of the error of the navigation state error estimate for each component of the navigation state error. To facilitate the discussion of the covariance matrix transition, the covariance matrix is separated into individual blocks. Likewise the navigation state estimation error covariance matrix $\left(\mathbf{P}^{+}\right)_{0}^{n+1}$ for time $\ell = 0$ in epoch $n + 1$ is separated into individual blocks and labeled as follows:

$$\left(\mathbf{P}^{+}\right)_{0}^{n+1} = \left[\begin{array}{c|c|c} \mathbf{P}_{1,1} & \mathbf{P}_{1,2} & \mathbf{P}_{1,3} \\ \hline \left(\mathbf{P}_{1,2}\right)^{T} & \mathbf{P}_{2,2} & \mathbf{P}_{2,3} \\ \hline \left(\mathbf{P}_{1,3}\right)^{T} & \left(\mathbf{P}_{2,3}\right)^{T} & \mathbf{P}_{3,3} \end{array}\right]_{13\times13} \tag{3.68}$$

The block labeled $\mathbf{P_{1,1}}$ is a 9×9 matrix that contains all of the covariance terms for the navigation state error estimates. The block labeled $\mathbf{P_{1,2}}$ is a 9×2 matrix which contains the off-diagonal covariance terms corresponding to the geolocation error estimates for the first ground feature. The block labeled $\mathbf{P_{2,2}}$ is a 2×2 matrix which contains the diagonal covariance terms for the geolocation error estimates for the first ground feature. The block labeled $\mathbf{P_{1,3}}$ is a 9×2 matrix and the section labeled $\mathbf{P_{2,3}}$ is a 2×2 matrix. These two matrices together contain the off-diagonal covariance terms corresponding to the geolocation error estimates for the second ground feature. The block labeled $\mathbf{P_{3,3}}$ is a 2×2 matrix that contains the diagonal covariance terms corresponding to the geolocaton error estimates for the second ground feature.

Since the nine navigation state error estimates remain the same for the transition between measurement epochs, the corresponding covariance terms will remain the same as well. This is shown as follows:

$$\mathbf{P}_{1,1_0}^{n+1} = \mathbf{P}_{1,1_L}^{n}$$

The section labeled $\mathbf{P_{1,2}}$ is populated with the off-diagonal covariance terms for the previously tracked second ground feature. This is presented as follows:

$$\mathbf{P}_{1,2_0}^{n+1} = \mathbf{P}_{1,3_L}^{n}$$

The terms in $\mathbf{P_{2,3}}$ in epoch n are discarded because they correlate the covariance of the previously tracked first ground feature with the covariance of the second. The section labeled $\mathbf{P_{2,2}}$ is populated with the diagonal covariance terms for the previously tracked second ground feature. This is presented as follows:

$$\mathbf{P}_{2,2_0}^{n+1} = \mathbf{P}_{3,3_L}^{n}$$

The covariance terms for the newly tracked ground feature in sections $\mathbf{P_{1,3}}$, $\mathbf{P_{2,3}}$, and $\mathbf{P_{3,3}}$ are determined by using matrix $\mathbf{M}$. The general matrix $\mathbf{M}$ must be augmented with zeros to account for the geolocation error terms in $\delta\mathbf{x_s}$. This augmentation is shown as follows:

$$\mathbf{M_s} = \begin{bmatrix} \mathbf{M}_{2\times 9} & \mathbf{0}_{2\times 4} \end{bmatrix}_{2\times 13} \tag{3.69}$$

The covariance terms in $\mathbf{P_{1,3}}$ are derived from the expectation of the navigation state error terms minus the KF estimated navigation state error terms. These covariance terms are expressed as follows:

$$\mathbf{P}_{1,3_0}^{n+1} = E\left\{ \left(\delta\mathbf{x_s}\right)_L^n \cdot \left[\mathbf{M_s} \cdot \left(\left(\delta\mathbf{x_s}\right)_L^n - \left(\widehat{\delta\mathbf{x}_\mathbf{s}}^{+}\right)_L^n \right) + \begin{pmatrix} \delta x_f \\ \delta y_f \end{pmatrix} \right]^T \right\}$$

$$\mathbf{P}_{1,3_0}^{n+1} = E\left\{ \left(\delta\mathbf{x_s}\right)_L^n \cdot \left(\delta\mathbf{x_s}\right)_L^{n^T} \right\} \cdot \mathbf{M_s}^T - \left[\left(\widehat{\delta\mathbf{x}_\mathbf{s}}^{+}\right)_L^n \cdot \left(\widehat{\delta\mathbf{x}_\mathbf{s}}^{+}\right)_L^{n^T} \right] \cdot \mathbf{M_s}^T$$

$$\mathbf{P}_{1,3_0}^{n+1} = \left(\mathbf{P}^{+}\right)_L^n \cdot \mathbf{M_s}^T - \left[\left(\widehat{\delta \mathbf{x}}_\mathbf{s}^{+}\right)_L^n \cdot \left(\widehat{\delta \mathbf{x}}_\mathbf{s}^{+}\right)_L^{n^T}\right] \cdot \mathbf{M_s}^T$$

The result is a 13×2 matrix, where the top nine rows fill the section $\mathbf{P_{1,3}}$. The covariance terms in $\mathbf{P_{2,3}}$ are derived from the covariance of the previous δx_{pc_2} and δy_{pc_2} terms in rows 12 and 13 of the covariance matrix minus the KF estimated values for δx_{pc_2} and δy_{pc_2}. These terms are shown as follows:

$$\mathbf{P}_{2,3_0}^{n+1} = \left(\mathbf{P}_{[12:13]}^{+}\right)_L^n \cdot \mathbf{M_s}^T - \begin{bmatrix} \widehat{\delta x}_{pc_2} \\ \widehat{\delta y}_{pc_2} \end{bmatrix} \cdot \left(\widehat{\delta \mathbf{x}}_\mathbf{s}^{+}\right)_L^{n^T} \cdot \mathbf{M_s}^T$$

The resulting matrix is 2×2, which fills $\mathbf{P_{2,3}}$ and relates the previous δx_{pc_2} and δy_{pc_2} uncertainty with the new measurement uncertainty. The covariance terms in $\mathbf{P_{3,3}}$ are derived from the previous covariance plus the covariance from the camera measurement.

$$\mathbf{P}_{3,3_0}^{n+1} = \mathbf{M_s} \cdot \left(\mathbf{P}^{+}\right)_L^n \cdot \mathbf{M_s}^T + \mathbf{I}_2 \cdot \sigma_c^2$$

The resulting matrix is 2×2, which fills $\mathbf{P_{3,3}}$ and is the covariance for the geolocation of the new ground feature.

3.9.2 Transitioning from epoch n to epoch $n+1$ with INS Bias Errors Only.

This section develops the transition for the INS system with only sensor bias errors. It is very similar to Section 3.9.1, except that bias terms must be accounted for appropriately. The KF's optimal estimate of the navigation state error at the end of epoch n is transitioned to epoch $n + 1$ according to the following:

$$\left(\widehat{\delta \mathbf{x}}_\mathbf{as}^{+}\right)_L^n = \begin{bmatrix} \widehat{\delta \mathbf{x}}_{9\times1} \\ \widehat{\mathbf{b}_\mathbf{a}}_{3\times1} \\ \widehat{\mathbf{b}_\mathbf{g}}_{3\times1} \\ \widehat{\delta x}_{pc_1} \\ \widehat{\delta y}_{pc_1} \\ \widehat{\delta x}_{pc_2} \\ \widehat{\delta y}_{pc_2} \end{bmatrix}_{19\times1} \Rightarrow \left(\widehat{\delta \mathbf{x}}_\mathbf{as}^{+}\right)_0^{n+1} = \begin{bmatrix} \widehat{\delta \mathbf{x}}_{9\times1} \\ \widehat{\mathbf{b}_\mathbf{a}}_{3\times1} \\ \widehat{\mathbf{b}_\mathbf{g}}_{3\times1} \\ \widehat{\delta x}_{pc_2} \\ \widehat{\delta y}_{pc_2} \\ 0 \\ 0 \end{bmatrix}_{19\times1} \tag{3.70}$$

where the nine error state estimates and the six INS bias error estimates remain the same. The geolocation error estimates for the first ground feature ($\widehat{\delta x}_{pc_1}$ and $\widehat{\delta y}_{pc_1}$) in epoch n are discarded because the ground feature is no longer in the camera's FOV. However, the geolocation error estimates for the second ground feature ($\widehat{\delta x}_{pc_2}$ and $\widehat{\delta y}_{pc_2}$) in epoch n are transitioned to the first ground feature position for epoch $n + 1$. The newly acquired ground feature error estimates ($\widehat{\delta x}_{pc_{\text{new}}}$ and $\widehat{\delta y}_{pc_{\text{new}}}$) are on average zero with a covariance derived from the previous epoch's navigation state error covariance plus the camera measurement error covariance.

The KF's covariance $\left(\mathbf{P}^{+}\right)_{L}^{n}$ of the navigation state error estimates from the last measurement L at the end of epoch n is as follows:

$$\left(\mathbf{P}^{+}\right)_{L}^{n} = \left[\begin{array}{ccc|cc|cc} \mathbf{P}\left(\widehat{\delta \mathbf{x}}\right)_{9\times 9} & \bullet & \bullet & \bullet & \bullet & \bullet & \bullet \\ \bullet & \mathbf{I}_3 \cdot \sigma_{b_a}^2 & \bullet & \bullet & \bullet & \bullet & \bullet \\ \bullet & \bullet & \mathbf{I}_3 \cdot \sigma_{b_g}^2 & \bullet & \bullet & \bullet & \bullet \\ \hline \bullet & \bullet & \bullet & P\left(\delta x_{pc_1}\right) & \bullet & \bullet & \bullet \\ \bullet & \bullet & \bullet & \bullet & P\left(\delta y_{pc_1}\right) & \bullet & \bullet \\ \hline \bullet & \bullet & \bullet & \bullet & \bullet & P\left(\delta x_{pc_2}\right) & \bullet \\ \bullet & \bullet & \bullet & \bullet & \bullet & \bullet & P\left(\delta y_{pc_2}\right) \end{array}\right]_{19\times 19} \tag{3.71}$$

where the (•) are place-holders representing the covariance values of the error of the navigation state error estimate for each component of the navigation state at time L in epoch n. In the same fashion as described in the previous section, the covariance matrix is separated into smaller sections according to the lines in (3.71). Likewise the covariance matrix $\left(\mathbf{P}^{+}\right)_{0}^{n+1}$ for time $\ell = 0$ in epoch $n + 1$ is separated into smaller sections and labeled

according to the following:

$$\left(\mathbf{P}^{+}\right)_{0}^{n+1} = \left[\begin{array}{c|c|c} \mathbf{P_{1,1}} & \mathbf{P_{1,2}} & \mathbf{P_{1,3}} \\ \hline \left(\mathbf{P_{1,2}}\right)^{T} & \mathbf{P_{2,2}} & \mathbf{P_{2,3}} \\ \hline \left(\mathbf{P_{1,3}}\right)^{T} & \left(\mathbf{P_{2,3}}\right)^{T} & \mathbf{P_{3,3}} \end{array}\right]_{19\times19} \tag{3.72}$$

In general, the transition of this covariance matrix is the same as the Free INS with only drift error terms shown in Section 3.9.1. The major difference is the inclusion of the bias covariance terms; however, their covariance does not change between measurement epochs and as a result the 15×15 section labeled $\mathbf{P_{1,1}}$ remains the same through the transition. This is presented as follows:

$$\mathbf{P}_{1,1_{0}}^{n+1} = \mathbf{P}_{1,1_{L}}^{n}$$

The covariance terms associated with the previously tracked first ground feature are discarded and the previously tracked second ground feature terms are transitioned into the sections for the first ground feature covariance terms, presented as follows:

$$\mathbf{P}_{1,2_{0}}^{n+1} = \mathbf{P}_{1,3_{L}}^{n}$$

$$\mathbf{P}_{2,2_{0}}^{n+1} = \mathbf{P}_{3,3_{L}}^{n}$$

where section $\mathbf{P_{1,2}}$ is a 15×2 matrix of the off-diagonal terms for the first ground feature and section $\mathbf{P_{2,2}}$ is a 2×2 matrix of the diagonal terms for the first ground feature. Section $\mathbf{P_{3,2}}$ contains the correlated covariance terms between the first and second ground features, therefore it is discarded from measurement L of epoch n.

The covariance terms for the newly tracked ground feature in sections $\mathbf{P_{1,3}}$, $\mathbf{P_{2,3}}$, and $\mathbf{P_{3,3}}$ are determined by using matrix $\mathbf{M}$. The general matrix $\mathbf{M}$ must be augmented with zeros to account for the bias error terms and the geolocation error terms in $\delta\mathbf{x_{as}}$. This augmentation is shown as follows:

$$\mathbf{M_{as}} = \left[\begin{array}{cc} \mathbf{M}_{2\times9} & \mathbf{0}_{2\times10} \end{array}\right]_{2\times19} \tag{3.73}$$

The elements in the 15×2 matrix, labeled $\mathbf{P_{1,3}}$, are the covariance of the cross-correlated nine navigation state error estimates and six bias estimates with the newly geolocated ground feature measurement estimates. These covariance values are derived from the expectation of the KF's previous navigation state error estimates with the measurement variance of the second ground feature. These covariance values are as follows:

$$\mathbf{P}_{1,3_0}^{n+1} = E\left\{\left(\delta\mathbf{x_{as}}\right)_L^n \cdot \left[\mathbf{M_{as}} \cdot \left(\left(\delta\mathbf{x_{as}}\right)_L^n - \left(\widehat{\delta\mathbf{x}}_{\mathbf{as}}^{+}\right)_L^n\right) + \begin{pmatrix} \delta x_f \\ \delta y_f \end{pmatrix}\right]^T\right\}$$

$$\mathbf{P}_{1,3_0}^{n+1} = E\left\{\left(\delta\mathbf{x_{as}}\right)_L^n \cdot \left(\delta\mathbf{x_{as}}\right)_L^{n^T}\right\} \cdot \mathbf{M_{as}}^T - \left[\left(\widehat{\delta\mathbf{x}}_{\mathbf{as}}^{+}\right)_L^n \cdot \left(\widehat{\delta\mathbf{x}}_{\mathbf{as}}^{+}\right)_L^{n^T}\right] \cdot \mathbf{M_{as}}^T$$

$$\mathbf{P}_{1,3_0}^{n+1} = \left(\mathbf{P}^{+}\right)_L^n \cdot \mathbf{M_{as}}^T - \left[\left(\widehat{\delta\mathbf{x}}_{\mathbf{as}}^{+}\right)_L^n \cdot \left(\widehat{\delta\mathbf{x}}_{\mathbf{as}}^{+}\right)_L^{n^T}\right] \cdot \mathbf{M_{as}}^T$$

The result is a 19×2 matrix, where the top 15 rows fill section $\mathbf{P_{1,3}}$. The covariance terms in $\mathbf{P_{2,3}}$ are derived from the covariance of the previous δx_{pc_2} and δy_{pc_2} terms, in rows 18 and 19 of the covariance matrix. $\mathbf{P}_{2,3_0}^{n+1}$ is expressed as follows:

$$\mathbf{P}_{2,3_0}^{n+1} = \left(\mathbf{P}_{[18:19]}^{+}\right)_L^n \cdot \mathbf{M_{as}}^T - \begin{bmatrix} \widehat{\delta x}_{pc_2} \\ \widehat{\delta y}_{pc_2} \end{bmatrix} \cdot \left(\widehat{\delta\mathbf{x}}_{\mathbf{as}}^{+}\right)_L^{n^T} \cdot \mathbf{M_{as}}^T$$

The resulting matrix is 2×2, which fills $\mathbf{P_{2,3}}$ and relates the previous δx_{pc_2} and δy_{pc_2} uncertainty with the new measurement uncertainty. The covariance terms in $\mathbf{P_{3,3}}$ are derived from the expectation of the newly geolocated ground feature measurements, and are expressed as follows:

$$\mathbf{P}_{3,3_0}^{n+1} = \mathbf{M_{as}} \cdot \left(\mathbf{P}^{+}\right)_L^n \cdot \mathbf{M_{as}}^T + \mathbf{I}_2 \cdot \sigma_c^2$$

The resulting matrix is 2×2, which fills $\mathbf{P_{3,3}}$ and is the covariance for the geolocation of the new ground feature.

3.9.3 Transitioning from epoch n to epoch $n+1$ with Both INS Error Sources.

The transition from epoch n to epoch $n + 1$ for the INS system with both random drift errors and sensor bias errors is accomplished in the same manner as Section 3.9.2. This is

the case because the transition only changes the KF navigation state error estimate and the associated covariance. At the point of transitioning between epochs the KF has already accounted for the uncertainty in the navigation state error due to system process noise. Therefore, the transition of the geolocation error estimates and the associated covariance are processed in the same manner as with no additive system process noise.

3.10 Summary

In summary, this chapter has fully developed the navigation scenario for simulation of the automated driftmeter fused with inertial measurements. Three INS sensor error configurations were presented: INS drift errors exclusively, INS bias errors exclusively, and combined INS errors. The Kalman filter fused vision measurements from the automated driftmeter with INS measurements in a SLAM process. Chapter 4 will now provide the results for these simulations.

IV. Results

This chapter presents the simulation results of the automated driftmeter aided INS developed in Chapter 3. Monte Carlo analyses are applied to the navigation scenarios to provide a statistical representation of true navigation state performance. The automated driftmeter is first evaluated with the same camera resolution used in the previous works of Relyea [3] and Quarmyne [4]. Two levels of analysis (60 or a 500 run Monte Carlo) are utilized. A 60 run Monte Carlo illustrates the performance of the same three error parameters presented in Chapter 3: INS drift errors exclusively, INS bias errors exclusively, and combined INS errors. Finally, the resolution is modified to provide improved results and is analyzed with a 500 run Monte Carlo, presenting a comparison between the results of a 9 MP and 25 MP camera in tabular form.

The resolution of the camera determines its measurement standard deviation. It is assumed that camera measurements would have an uncertainty of one pixel relative to the truth data. The standard deviation for each camera specification is calculated using equation (3.42), presented again here for convenience:

$$\sigma_c = \sqrt{\frac{1}{\#\,\mathrm{MP}} \cdot 10^{-6}}$$

where the covariance of the camera measurement is the inverse of the number of pixels populating the focal plane. The square root of that value provides the standard deviation of those camera measurements.

The 1-σ inertial sensor specifications for this analysis are drawn from Section 3.5 and presented in Table 4.1. The combined specifications provide a variance of 1 $\frac{km}{hr}$. However, some sections only utilize part of these specifications and consequently do not provide the full 1 $\frac{km}{hr}$ variance. The sampling rate of the inertial sensors and the camera are set to 1 Hz. The Kalman filter measurement updates from the camera therefore occur at the same rate that inertial measurements are made.

Table 4.1: Calculated 1-σ inertial sensor specifications provided a variance of 1 $\frac{km}{hr}$ drift error due to the influence of drift and biases. These values are non-dimensional for this navigation scenario.

Parameter	UNITS	1 km/hr
Sampling interval	s	1
Gyro bias sigma	Non-Dim	6.4247×10^{-8}
Angular random walk	Non-Dim	2.8746×10^{-7}
Accel bias sigma	Non-Dim	7.7118×10^{-6}
Velocity random walk	Non-Dim	4.0085×10^{-5}

4.1 Automated Driftmeter Utilizing 9 MP Camera

This section presents the results of the three Free INS error parameters presented in Chapter 3. Section 4.1.1 presents resutls for INS drift errors only. Section 4.1.3 presents the results for INS bias errors only. Section 4.1.5 presents the results for a combination of the INS errors.

4.1.1 A Single Run with INS Drift Errors Only.

The KF is able to estimate the Free INS's drift error, as illustrated in Figures 4.1 and 4.2. The KF's covariance indicates the uncertainty of the estimate, while the Free INS's covariance indicates the uncertainty in position. Due to the error accumulations within 15 epochs (150 seconds) the Free INS's uncertainty in position is 5 m. However, the Free INS's uncertainty in position accumulates to approximately 600 m within 360 epochs (1 hour). The KF's covariance for the x-position also accumulates with time, while the covariance of the y & z-positions stabilize. This indicates the KF's confidence in its estimate.

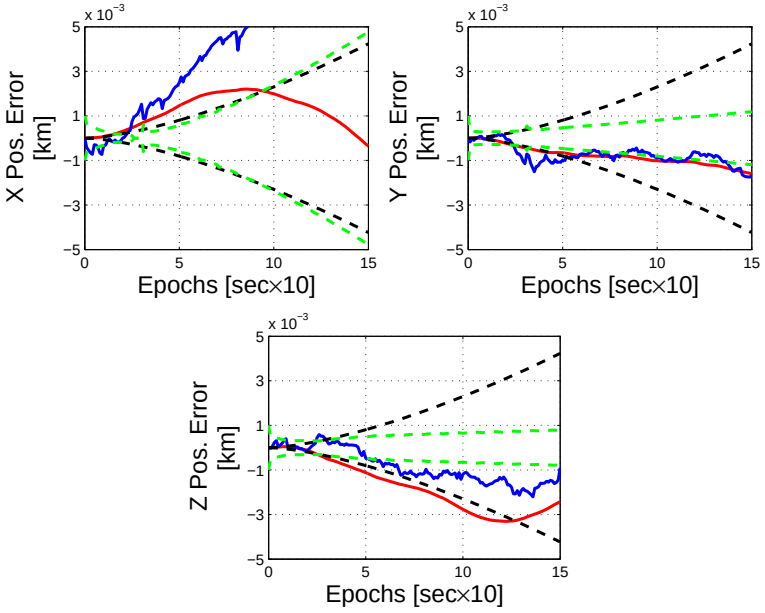

Figure 4.1: First 15 epochs of position error with only INS drift errors, aided by a 9 MP camera. The Free INS position error is indicated with a red solid line and the KF estimate with a blue solid line. The Free INS covariance is indicated with a black dashed line and the KF covariance is indicated with a green dashed line.

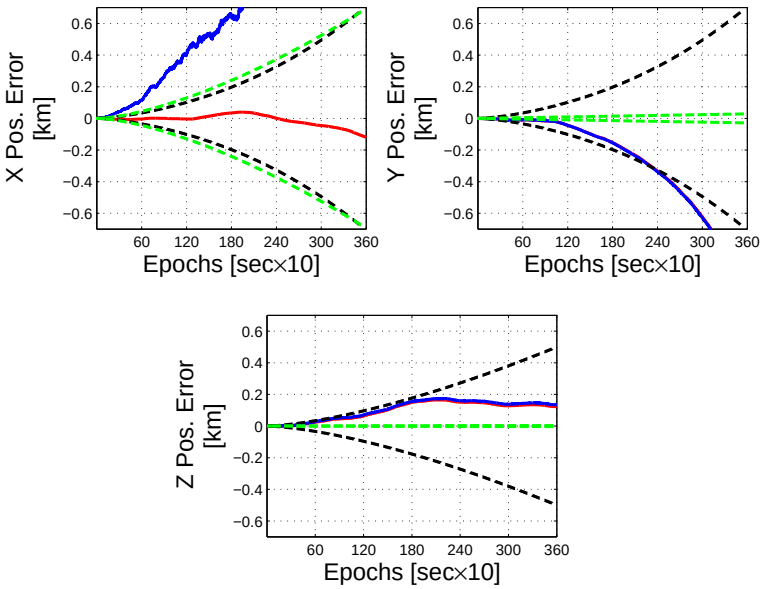

Figure 4.2: Full 360 epochs of position error with only INS sensor drift errors, aided by a 9 MP camera. Color scheme is the same as that in Figure 4.1.

4.1.2 60 Run Monte Carlo Analysis with INS Drift Errors Only.

The 60 run Monte Carlo analysis provides a statistical representation of the Free INS and the aided INS performance, and is indicated in Figures 4.3, 4.4, and 4.5. This analysis includes each individual run of the Free INS's and the aided INS's position error, along with their mean and standard deviations. The mean values are provided to illustrate the quality of the Monte Carlo analysis, which is determined by comparing the mean system output to the mean of the Gaussian distribution input (zero for this data).

In Figure 4.3, the x-axis standard deviation of the aided INS performance is the same as, if not worse than, the Free INS performance. Along the y-axis (in Figure 4.4) the aided system's performance is significantly better than the Free INS's performance, such that the standard deviation constrains its mean error close to zero. Likewise, the aided system's performance along the z-axis, (in Figure 4.5) is even better than the y-position's performance, such that the standard deviation constrains its mean error closer to zero.

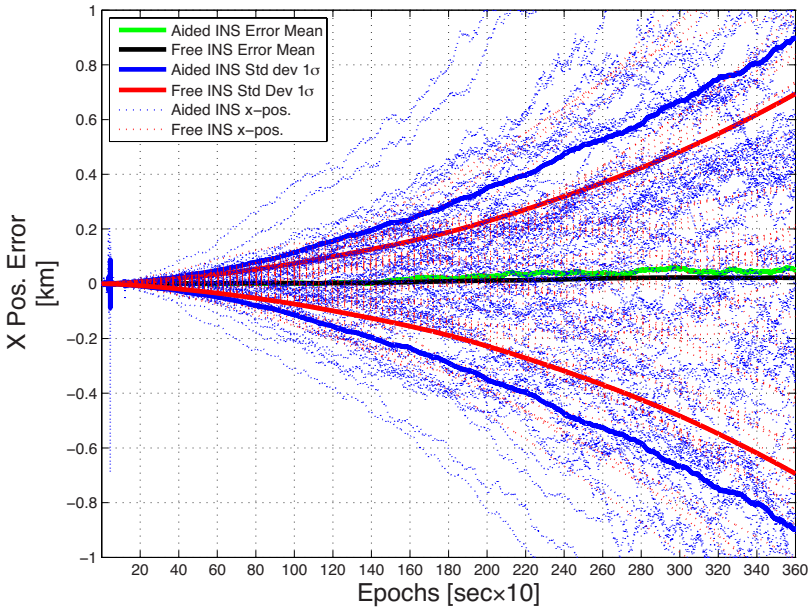

Figure 4.3: 60-run Monte Carlo of x-position error with only INS sensor drift errors and aided by an automated driftmeter, with a 9 megapixel camera.

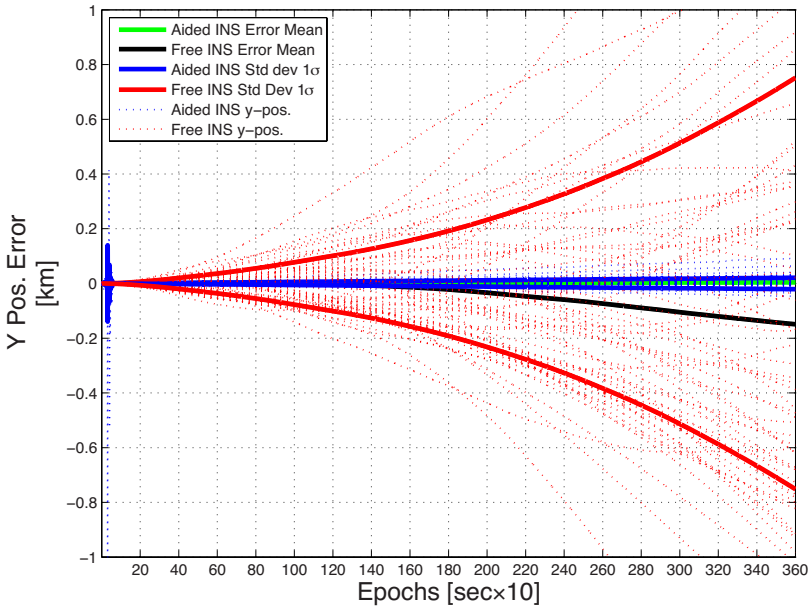

Figure 4.4: 60-run Monte Carlo of y-position error with only INS sensor drift errors and aided by an automated driftmeter, with a 9 megapixel camera.

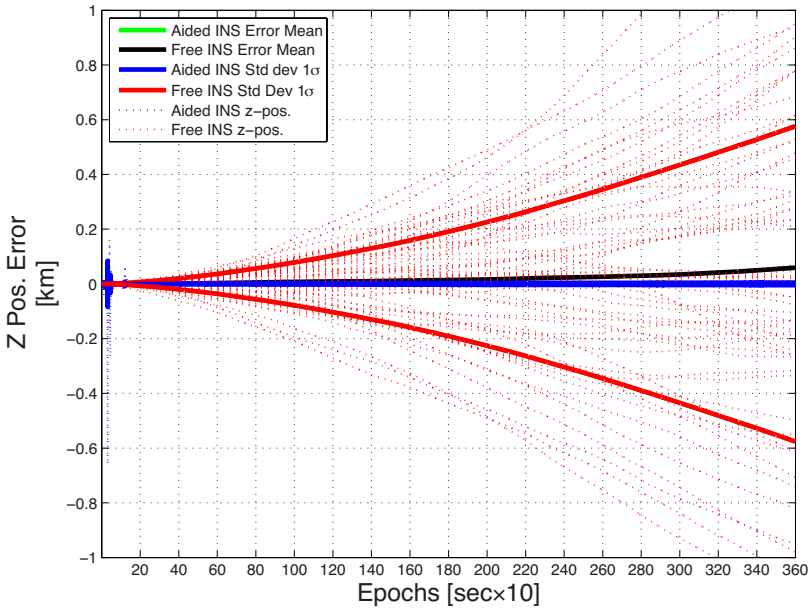

Figure 4.5: 60-run Monte Carlo of z-position error with only INS sensor drift errors and aided by an automated driftmeter, with a 9 megapixel camera.

The final navigation state error standard deviation results from this 60 run Monte Carlo analysis are presented in Table 4.2.

Table 4.2: 60 Run Monte Carlo with only drift final navigation state error standard deviations.

Std Dev	Unaided Final Value	Aided Final Value	Percent Improved
σ_x	0.694 km	899.93 m	−29.7%
σ_y	0.751 km	20.90 m	97.2%
σ_z	0.576 km	4.79 m	99.2%
σ_{v_x}	4.30×10^{-3} m/s	4.81×10^{-3} m/s	−11.9%
σ_{v_y}	4.73×10^{-3} m/s	1.72×10^{-4} m/s	96.4%
σ_{v_z}	5.88×10^{-2} m/s	2.54×10^{-4} m/s	99.6%
σ_ϕ	1.73×10^{-5} rad	1.13×10^{-5} rad	34.7%
σ_θ	1.76×10^{-5} rad	1.49×10^{-5} rad	15.3%
σ_ψ	1.85×10^{-5} rad	5.91×10^{-5} rad	−219.5%

4.1.3 A Single Run with INS Bias Errors Only.

The KF's ability to estimate the Free INS's bias error is illustrated in Figures 4.6 and 4.7. Contrary to the drift error analysis, this Free INS's error accumulates to 1 m within the first 15 epochs (150 seconds). For 360 epochs (1 hour), the Free INS's uncertainty in position accumulates to approximately 600 m, similar to the drift error plot. This KF's covariance for the x-position also increases with time; however, remains less than the covariance of the drift error-faulted INS. This KF's covariance for the y & z-positions stabilize in the same way as the system that only contains drift errors.

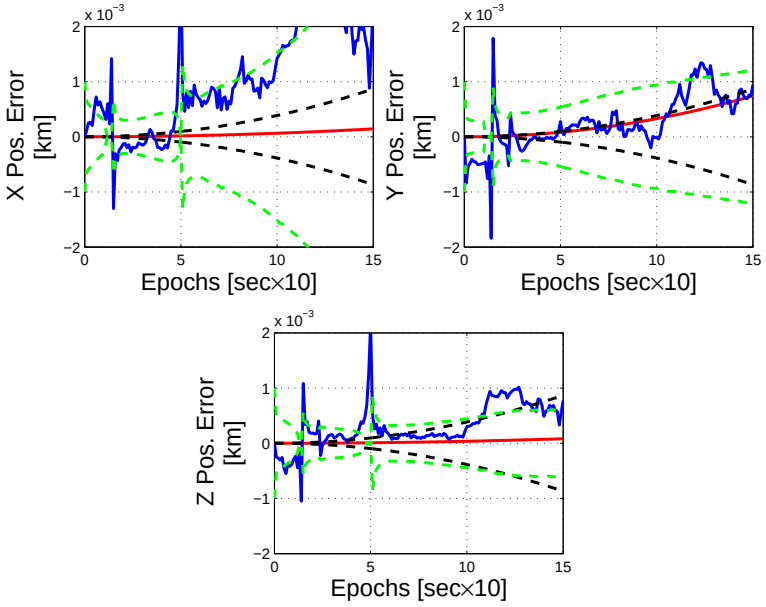

Figure 4.6: First 15 epochs of position error with only INS bias errors, aided by a 9 MP camera. The Free INS position error is indicated with a red solid line and the KF estimate with a blue solid line. The Free INS covariance is indicated with a black dashed line and the KF covariance is indicated with a green dashed line.

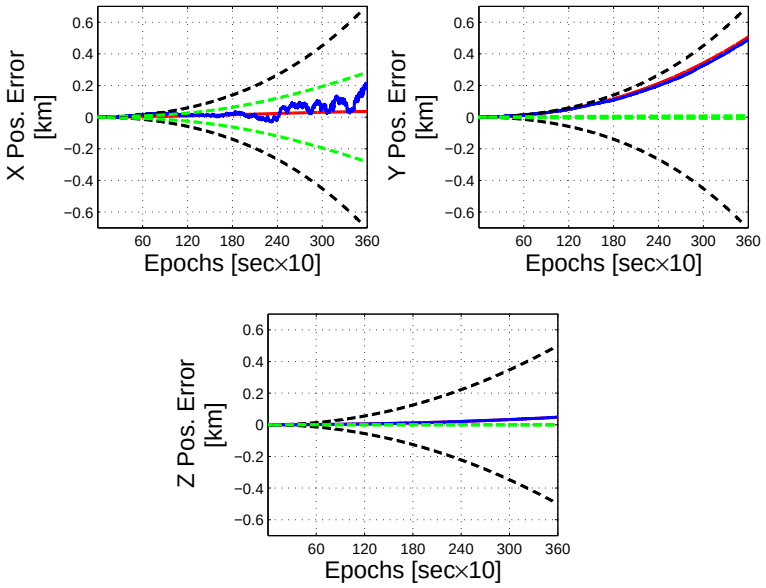

Figure 4.7: Full 360 epochs of position error with only INS sensor bias errors, aided by a 9 MP camera. Color scheme is the same as that in Fig 4.6.

4.1.4 60 Run Monte Carlo Analysis with INS Bias Errors Only.

This section presents the results of a 60 run Monte Carlo analysis with only INS sensor bias errors in Figures 4.8, 4.9, and 4.10. Contrary to the drift error analysis, when the standard deviation of the aided INS performance along the x-axis is evaluated,it proves slightly better than the Free INS performance. In the same manner, the aided INS performance along the y and z axes is much better than the Free INS performance.

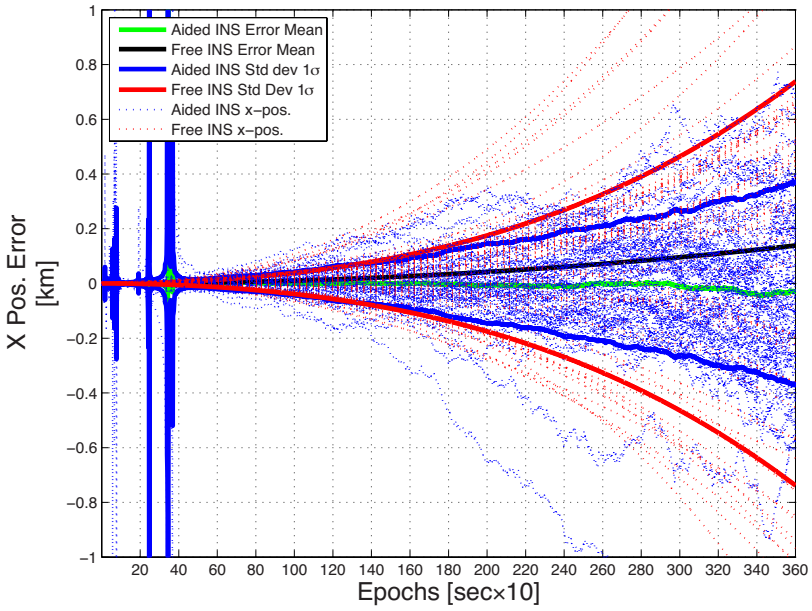

Figure 4.8: 60-run Monte Carlo of x-position error with only INS sensor bias errors and aided by an automated driftmeter, with a 9 megapixel camera.

Throughout these simulations, spikes are apparent from white Gaussian noise caused by the camera measurement noise. They are more evident early in the simulations due to the smaller average values of the estimates. These spikes in the standard deviations caused unstable results at times, which are not presented in the results section, because they are considered statistical outliers.

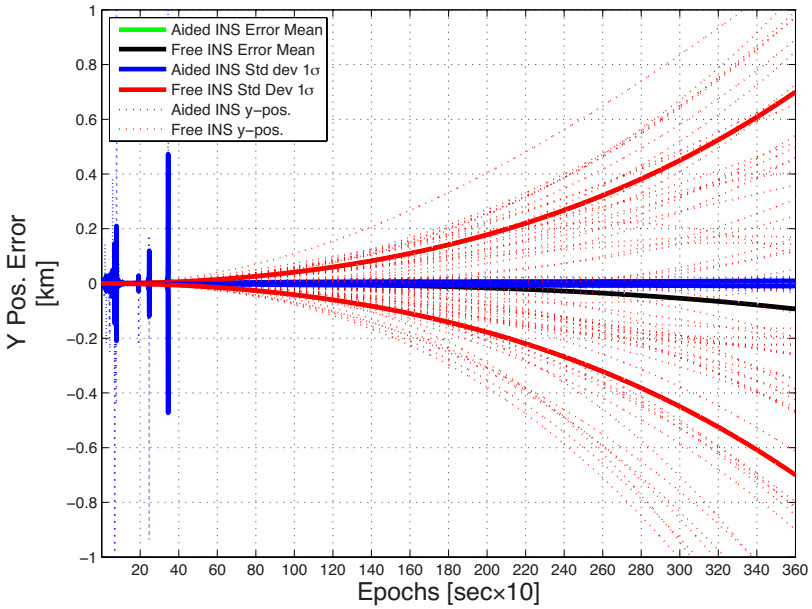

Figure 4.9: 60-run Monte Carlo of y-position error with only INS sensor bias errors and aided by an automated driftmeter, with a 9 megapixel camera.

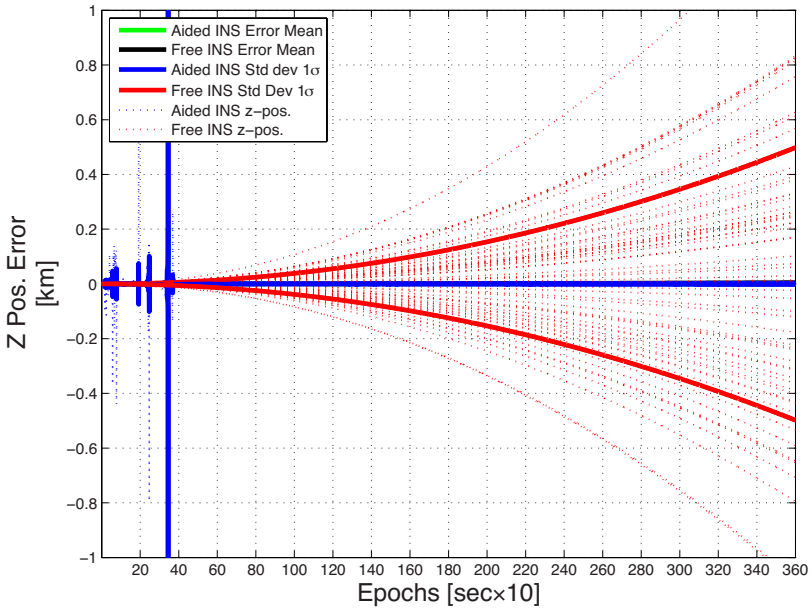

Figure 4.10: 60-run Monte Carlo of z-position error with only INS sensor bias errors and aided by an automated driftmeter, with a 9 megapixel camera.

The final navigation state error standard deviation results from this 60 run Monte Carlo analysis are presented in Table 4.3.

Table 4.3: 60 Run Monte Carlo with only bias final navigation state error standard deviations.

Std Dev	Unaided Final Value	Aided Final Value	Percent Improved
σ_x	0.738 km	369.01 m	50.0%
σ_y	0.700 km	9.56 m	98.6%
σ_z	0.498 km	2.54 m	99.49%
σ_{v_x}	5.41×10^{-3} m/s	2.48×10^{-3} m/s	54.2%
σ_{v_y}	4.92×10^{-3} m/s	3.68×10^{-5} m/s	99.25%
σ_{v_z}	5.40×10^{-3} m/s	1.32×10^{-5} m/s	99.8%
σ_ϕ	2.31×10^{-5} rad	8.13×10^{-6} rad	64.8%
σ_θ	2.64×10^{-5} rad	1.25×10^{-5} rad	52.7%
σ_ψ	2.26×10^{-5} rad	3.66×10^{-5} rad	-61.9%

4.1.5 A Single Run with Combined INS Sensor Errors.

The KF's ability to estimate both the drift and bias errors combined in the Free INS is illustrated in Figures 4.11 and 4.12. From this single run, significant change in performance is not evident when compared to just one type of inertial sensor error simulation. In the x-axis, the KF's covariance is slightly better than the Free INS's covariance. However, in the y and z-axis, the KF covariance is significantly better than the Free INS covariance.

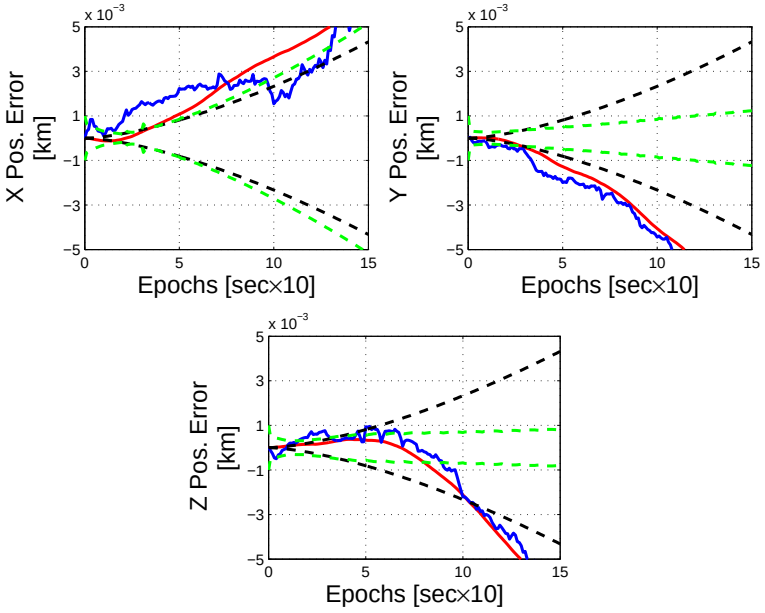

Figure 4.11: First 15 epochs of position error with combined INS errors, aided by a 9 MP camera. The Free INS position error is indicated with a red solid line and the KF estimate with a blue solid line. The Free INS covariance is indicated with a black dashed line and the KF covariance is indicated with a green dashed line.

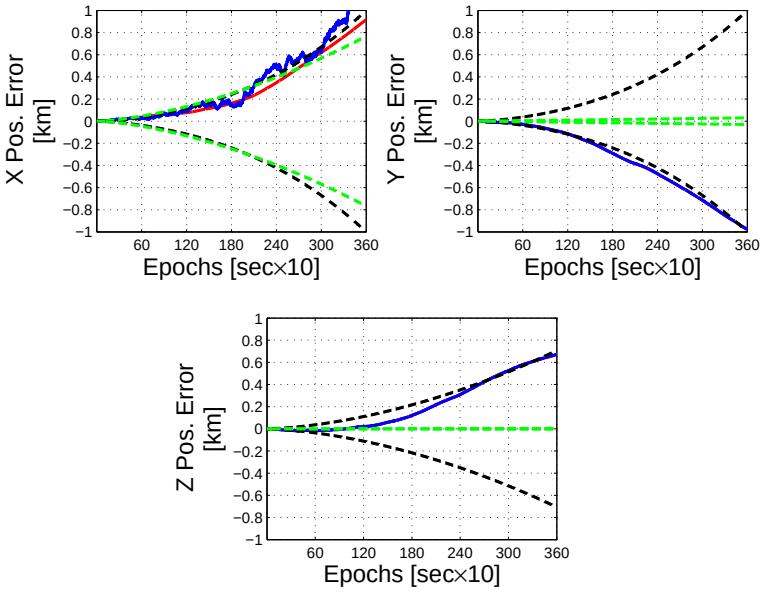

Figure 4.12: Full 360 epochs of position error with combined INS sensor errors, aided by a 9 MP camera. Color scheme is the same as that in Fig 4.11.

4.1.6 60 Run Monte Carlo Analysis with Combined INS Sensor Errors.

This section provides the results of a 60 run Monte Carlo analysis where both the drift and bias errors are combined in the Free INS. These results are shown in Figures 4.13, 4.14, and 4.15.

Having great similarity to the simulations with just drift error in the Free INS, the aided INS standard deviation is slightly better than the Free INS standard deviation in the x direction. The aided y and z standard deviation of the position error remains significantly better than the Free INS.

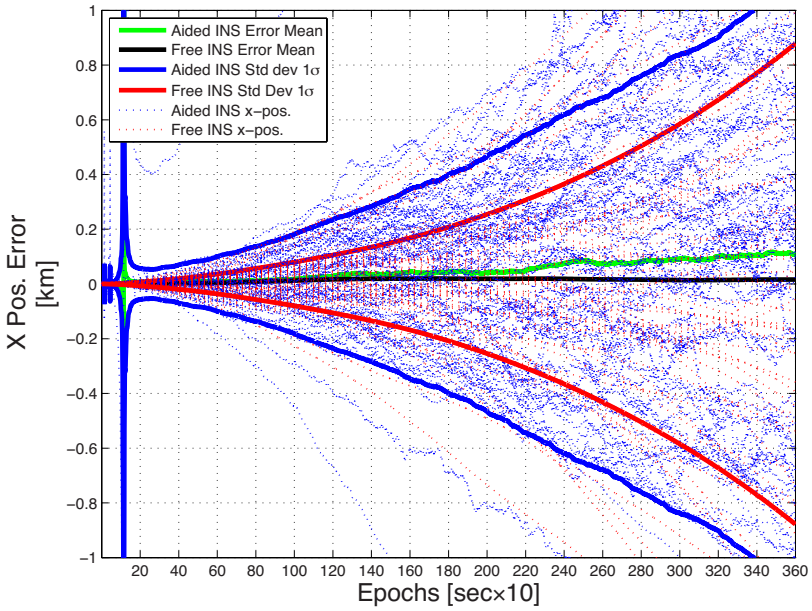

Figure 4.13: 60-run Monte Carlo of x-position error with combined INS sensor errors and aided by an automated driftmeter, with a 9 megapixel camera.

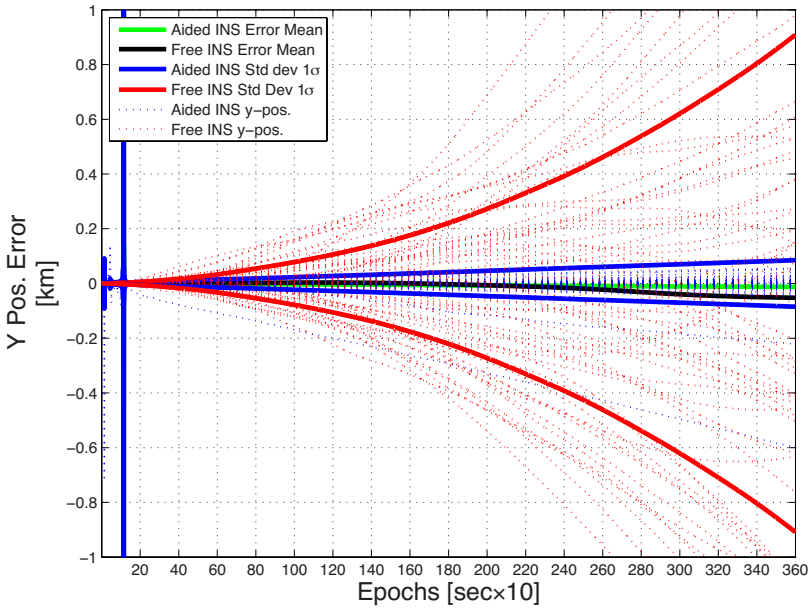

Figure 4.14: 60-run Monte Carlo of y-position error with combined INS sensor errors and aided by an automated driftmeter, with a 9 megapixel camera.

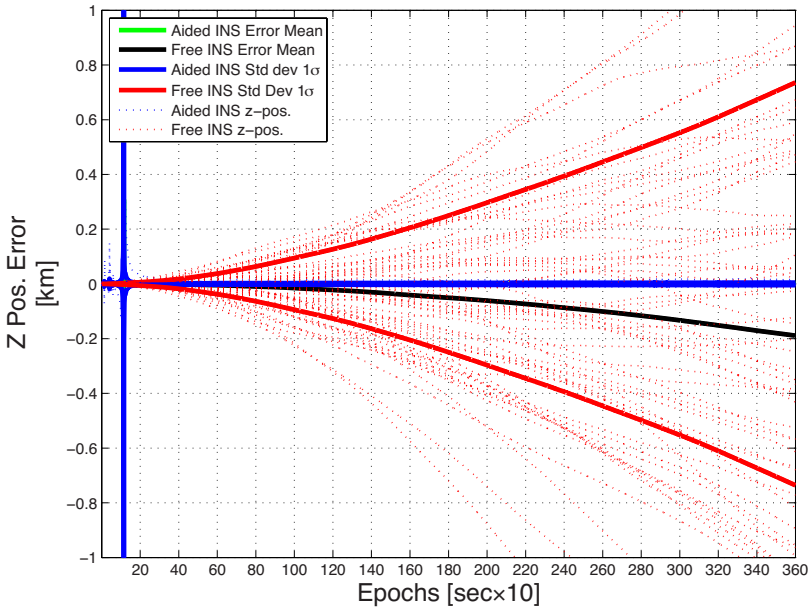

Figure 4.15: 60-run Monte Carlo of z-position error with combined INS sensor errors and aided by an automated driftmeter, with a 9 megapixel camera.

The final standard deviation of the navigation state error from this 60 run Monte Carlo analysis is presented in Table 4.4.

Table 4.4: 60 Run Monte Carlo with combined INS sensor errors final navigation state error standard deviations.

Std Dev	Unaided Final Value	Aided Final Value	Percent Improved
σ_x	0.878 km	1,091.21 m	−24.2%
σ_y	0.908 km	85.03 m	90.6%
σ_z	0.736 km	4.85 m	99.3%
σ_{v_x}	6.09×10^{-3} m/s	4.91×10^{-3} m/s	19.4%
σ_{v_y}	5.90×10^{-3} m/s	3.02×10^{-4} m/s	94.9%
σ_{v_z}	1.88×10^{-1} m/s	2.31×10^{-4} m/s	99.9%
σ_ϕ	2.46×10^{-5} rad	1.39×10^{-5} rad	43.5%
σ_θ	2.63×10^{-5} rad	1.65×10^{-5} rad	37.3%
σ_ψ	2.47×10^{-5} rad	2.43×10^{-4} rad	−883.8%

4.2 Comparison of a 9 MP with a 25 MP Camera Using 500 Run Monte Carlo

The results from the previous 60 run Monte Carlo analyses are sufficient to show that the system's performance is inadequate with the 9 MP camera and requires modification. This section performs a 500 run Monte Carlo analysis, first with the 9 MP camera and then with a modified 25 MP camera. The error configuration utilizing both error sources is most similar to a real Free INS system. Therefore, Section 4.2 will only be concerned with this configuration.

4.2.1 500 Run Monte Carlo Utilizing a 9 MP camera.

The plots for the 500 run Monte Carlo analysis, using a 9 MP camera, are presented in Figures 4.16, 4.17, and 4.18.

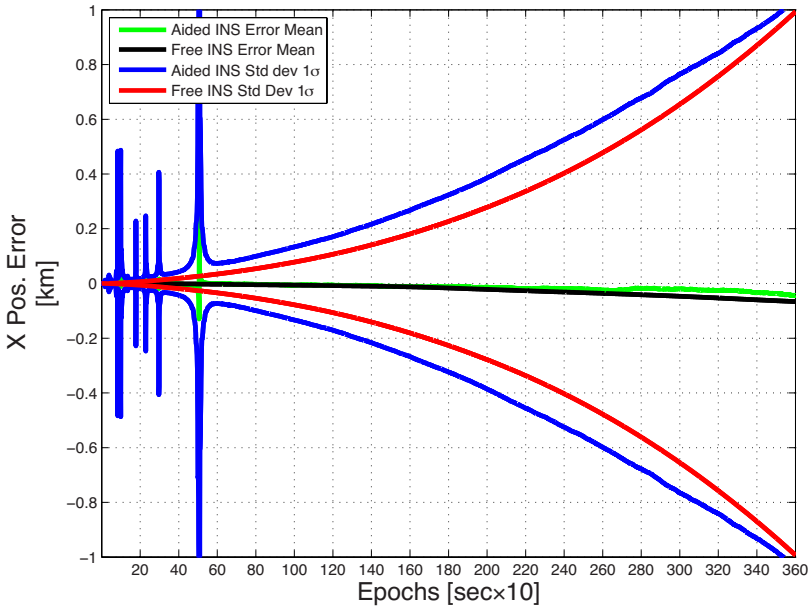

Figure 4.16: 500 Run Monte Carlo of x-position error with combined INS sensor errors and aided by an automated driftmeter, with a 9 megapixel camera.

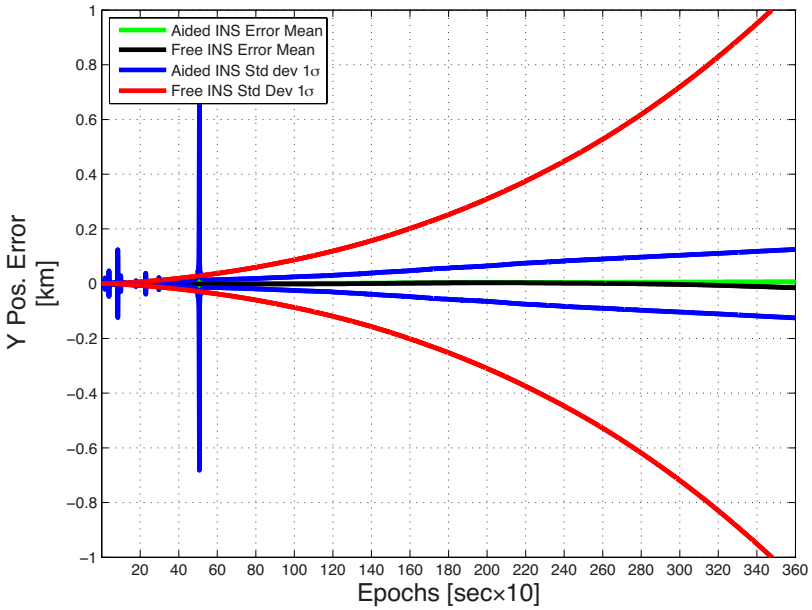

Figure 4.17: 500 Run Monte Carlo of y-position error with combined INS sensor errors and aided by an automated driftmeter, with a 9 megapixel camera.

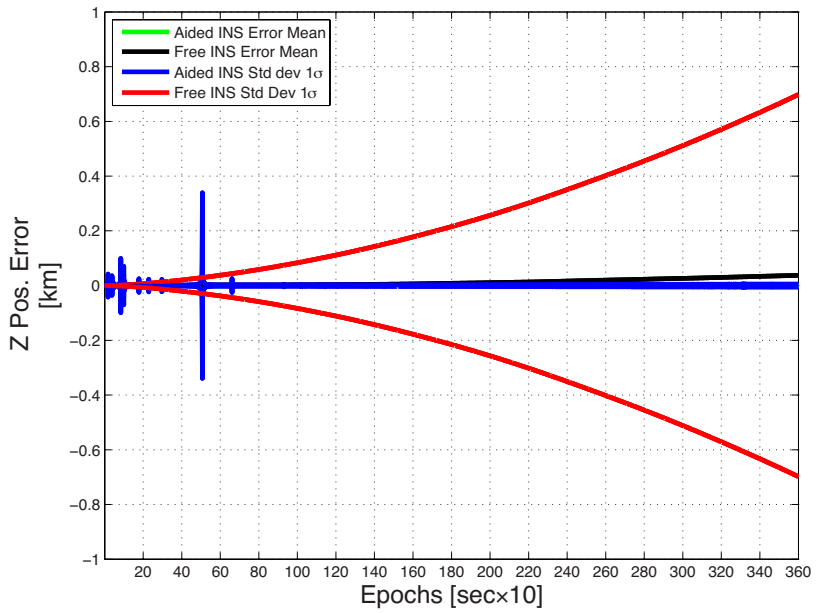

Figure 4.18: 500 Run Monte Carlo of z-position error with combined INS sensor errors, aided by an automated driftmeter, with a 9 megapixel camera.

The final standard deviation of the navigation state error from this 500 run Monte Carlo analysis is presented in Table 4.5. These results should represent a stronger statistical representation for the 9MP combined sensor error than the 60 run Monte Carlo.

Table 4.5: Final navigation state error standard deviation from a 500 Run Monte Carlo with combined INS sensor errors and a 9 MP camera

Std Dev	Unaided Final Value	9 MP Aided Final Value	Percent Improved
σ_x	0.992 km	1024.76 m	−3.2%
σ_y	1.081 km	125.18 m	88.4%
σ_z	0.698 km	5.29 m	99.2%
σ_{v_x}	6.72×10^{-3} m/s	5.24×10^{-3} m/s	22.0%
σ_{v_y}	7.13×10^{-3} m/s	3.97×10^{-4} m/s	94.4%
σ_{v_z}	3.73×10^{-2} m/s	2.4×10^{-4} m/s	99.4%
σ_ϕ	2.95×10^{-5} rad	1.39×10^{-5} rad	52.9%
σ_θ	2.94×10^{-5} rad	1.85×10^{-5} rad	37.1%
σ_ψ	2.97×10^{-5} rad	3.53×10^{-4} rad	−1088.5%

4.2.2 500 Run Monte Carlo Utilizing a 25 MP camera.

The plots for the 500 run Monte Carlo analysis, using a 25 MP camera, are presented in Figures 4.19, 4.20, and 4.21.

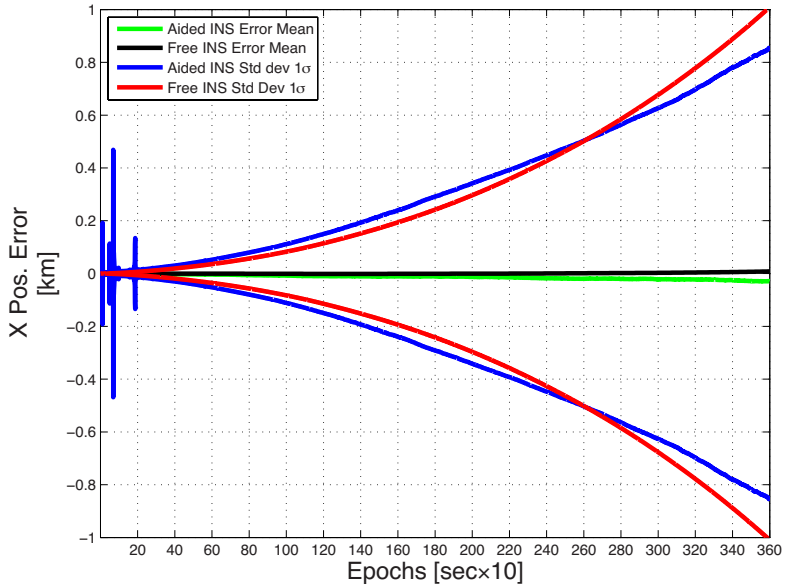

Figure 4.19: 500-run Monte Carlo of x-position error with combined INS sensor errors, aided by an automated driftmeter, with a 25 megapixel camera.

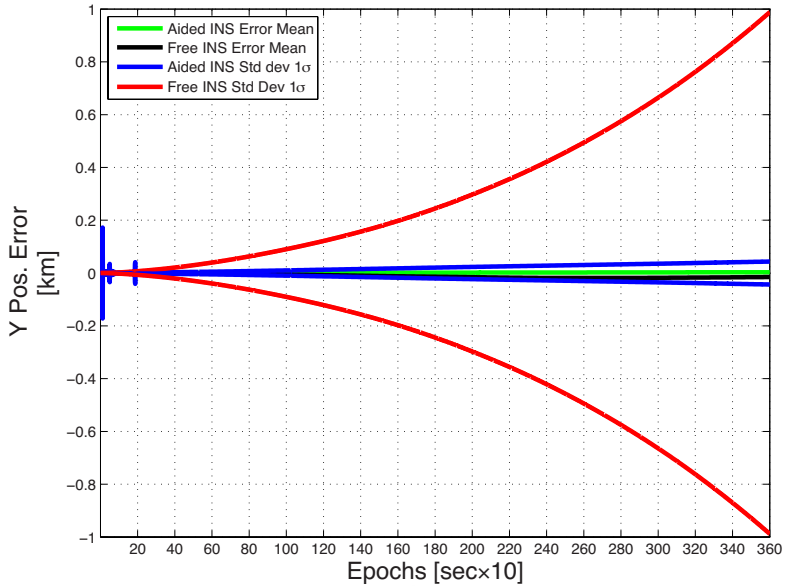

Figure 4.20: 500-run Monte Carlo of y-position error with combined INS sensor errors, aided by an automated driftmeter, with a 25 megapixel camera.

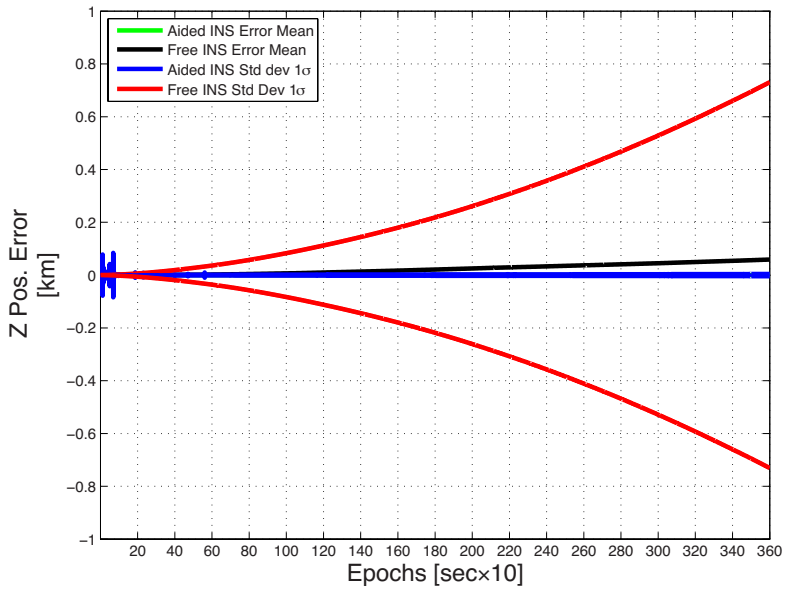

Figure 4.21: 500-run Monte Carlo of z-position error with combined INS sensor errors, aided by an automated driftmeter, with a 25 megapixel camera.

The final standard deviation of the navigation state error from this 500 run Monte Carlo analysis is presented in Table 4.6. By simply changing the camera resolution, significant improvements are evident throughout these tabulated results.

Table 4.6: Final navigation state error standard deviation from a 500 Run Monte Carlo with combined INS sensor errors and a 25 MP camera

Std Dev	Unaided Final Value	25 MP Aided Final Value	Percent Improved
σ_x	1.009 km	856.22 m	15.2%
σ_y	988.01 km	43.49 m	95.6%
σ_z	0.730 km	4.10 m	99.4%
σ_{v_x}	6.68×10^{-3} m/s	4.11×10^{-3} m/s	38.5%
σ_{v_y}	6.57×10^{-3} m/s	1.93×10^{-4} m/s	97.1%
σ_{v_z}	5.88×10^{-2} m/s	2.01×10^{-4} m/s	99.7%
σ_ϕ	2.97×10^{-5} rad	1.39×10^{-5} rad	53.2%
σ_θ	2.90×10^{-5} rad	1.52×10^{-5} rad	47.6%
σ_ψ	2.80×10^{-5} rad	1.24×10^{-4} rad	−342.9%

4.3 Summary

This chapter presents the simulation results of the automated driftmeter aided INS developed in Chapter 3. The driftmeter was first evaluated with a 9 MP camera. The results from a single run of each of the three Free INS error parameters illustrate that the KF is able to estimate the bias error of the Free INS more easily than the drift error, providing better aided navigation performance. It is also noted that the estimate of the x-position error is very weak and is further supported with 60 run Monte Carlo analyses, which statistically represents the performance of the aided system. The final standard deviation values of each navigation state error are presented in tables corresponding to these Monte Carlo analyses. These final navigation state error values are used to determine the percent improvement of the aided system. From these results it is noted that the aiding for the ψ Euler angle is also very week. Finally, the camera resolution is modified to 25 MP and the two different systems are compared using a 500 run Monte Carlo, where it is shown that 25 MP resolution provides improved navigation state error estimation and aiding throughout all nine error states.

V. Conclusions and Recommendations

This thesis advances the development of a method for aiding a navigation-grade INS with an optical sensor, acting as a automated driftmeter. The motivation of this research is to achieve precision navigation similar to GPS and thus providing an alternative passive navigation system for military aircraft applications. Simulations are performed to evaluate the KF's ability to mitigate the deleterious effects of the inertial sensor errors of a Free INS. The main contribution of this research is the calculation of the covariance of the geolocation error of a ground feature and then tracking that feature until it disappears from the field of view of the camera, whereupon it is replaced by a newly geolocated ground feature. Monte Carlo analyses are performed in order to gain a statistical representation of this new aided system's performance. This chapter summarizes the results of these Monte Carlo analyses and provides recommendations for future research.

5.1 Conclusions

This research incorporates a linear Kalman filter algorithm, which utilizes bearing measurements from geolocating and tracking ground features to aid a Free INS during a simulated one hour flight. Two levels of Monte Carlo analysis, a 60 run and a 500 run, are performed, and their results are compiled to establish the degree of improvement afforded by this method of aiding a navigation-grade INS with an optical sensor.

The current configuration of this automated driftmeter-aided INS does not meet the precision navigation standards established by GPS. It is shown with the single run simulations that the linear KF is able to precisely estimate the x, y, and z-position errors within the first 15 epochs (that is, after having geolocated 15 ground features over a timespan of 150 s). Over a longer duration of time, however, the linear KF is not able to estimate the error for the x-position data as effectively. In the best case scenario with

combined Free INS error sources, and utilizing the 25 MP camera, the x-position error range is reduced to 856 m. This range is far from the accuracy of GPS.

5.2 Recommendations for Future Work

The inability to estimate the errors in the x-position has been persistent throughout this research as well as the previous research by Quarmyne [4] and Relyea [3]. This problem is not resolved herein. Any future work should focus on the disparity between position error measurements. This may be resolved by using an indirect feedback KF configuration, as discussed in Chapter 2.

The spikes that are due to the camera measurement noise should be resolved to improve overall reliability of the aided system. This may be done by implementing residual monitoring in the KF algorithm. This is done to establish ”reasonableness checking of measurements before they are processed by the filter” [1].

Further research should evaluate the benefit of providing precise altitude information to the KF and thus reducing the coupled position error effect from the INS in the measurement equation. This additional altitude information should improve the overall navigation capabilities of this autonomous driftmeter. After all, altitude information was used with driftmeter measurements in the golden age of navigation.

This research employs a simplified navigation scenario, simulated in MATLAB, to evaluate the possibilities of using bearing-only optical measurements. The results proved inferior to the performance of the precision navigation standard of GPS. This research does, however, have the potential to provide an avenue for future improvement of this passive navigation tool for military applications.

Appendix A: Honeywell HG9900 INS

Specifications from a commercial navigation grade INS are used for comparison with the calibrated INS sensor values. The Honeywell HG9900 is a navigation grade INS with a long-time position accuracy of 0.8 $\frac{nmi}{hr}$ performance, which is equivalent to 1.48 $\frac{km}{hr}$. The HG9900 IMU's 1-σ error specifications are provided in Table A.1.

Table A.1: Honeywell HG9900 tactical-grade IMU 1-σ error specifications [22]. The value for the velocity random walk is not provided.

Parameter	UNITS	HG9900
Sampling interval	ms	3.33
Gyro bias sigma	deg/hr	< 0.003
Angular random walk	deg/$\sqrt{hr}$	< 0.002
Gyro scalefactor sigma	PPM	< 5.0
Accel bias sigma	m/s^2	$< 25 \times 10^{-6}$
Velocity random walk	m/s/$\sqrt{hr}$	not provided
Accel scalefactor sigma	PPM	< 100

The gyro scale factor causes an error to occur only during actual rotation. The accelerometer scale factor causes an error to occur only during actual acceleration. They are specified in terms of Parts Per Million (PPM). Therefore, the error for 360 degrees of rotation is computed as follows:

$$\left(\frac{5}{1000000}\right) \cdot 360\ deg = 0.0018\ deg$$

The error for an acceleration of 10 $\frac{m}{s^2}$ is computed as follows:

$$\left(\frac{100}{1000000}\right) \cdot 10\ \frac{m}{s^2} = 0.001\ \frac{m}{s^2}$$

In the scenario in this research, the nominal rotation and acceleration are zero; therefore, the scale factor errors can be ignored. Section A.1 analyzes the Gyro's error dynamics to better understand how these error specifications relate to the calibrated error values.

A.1 Connecting the HG9900 Gyro's Specifications to the Mathematical Model of the Error Equations

The continuous-time dynamics are expressed as

$$\dot{\theta} = \omega + b + \sigma_c \cdot \dot{w} \,, \quad \theta_0 = 0 \tag{A.1}$$

where ω is the true input angular rate, b is the gyro's random bias, $b \sim N(0,\ \sigma_b^2)$ and w is a unit Brownian motion $w \sim N(0,\ t)$. Therefore, the mathematical model's units for the gyro's continuous-time drift parameter σ_c are $\frac{rad}{\sqrt{s}}$ and it is related to the HG9900 Angle Random Walk specification σ_θ as follows:

$$\sigma_c = \frac{\sigma_\theta}{60 \cdot 57.3} \ \frac{rad}{\sqrt{s}} \tag{A.2}$$

$$\sigma_c = \frac{0.002}{60 \cdot 57.3} = 5.817 \times 10^{-7} \ \frac{rad}{\sqrt{s}} \tag{A.3}$$

The discrete-time system dynamics are as follows:

$$\theta_{k+1} = \theta_k + (\omega_k + b)\Delta T + \zeta_k \tag{A.4}$$

where

$$\zeta_k \sim N(0,\ \sigma_d^2) \,, \quad \theta_0 = 0 \tag{A.5}$$

When the true angular rate ω_k is zero and the bias is zero, then $\theta_k \sim N(0,\ k \cdot \sigma_d^2)$ (where $k = 3600 \cdot f_s$ at one hour). Therefore the following is true:

$$\sigma_\theta^2 = 3600 \cdot f_s \cdot \sigma_d^2 \tag{A.6}$$

which is

$$\sigma_d = \frac{\sigma_\theta}{60 \cdot 57.3} \cdot \frac{1}{\sqrt{f_s}}$$

The sampling frequency is 1 Hz or 1 $\frac{1}{s}$. Therefore, following is true:

$$\sigma_d = \frac{0.002}{60 \cdot 57.3} \cdot \frac{1}{\sqrt{1}} = 5.82 \times 10^{-7}\ rad$$

The manufacturer's specifications have now been related to the parameters of the discrete-time INS update scenario.

A.2 Non-Dimensionalized HG9900 Specifications

The HG9900's bias and drift error specifications are non-dimensionalized according to the method employed in Section A.1 using parameters described in Section 3.1.

Rate Gyro (HG9900)

- $0.003 \cdot \frac{\cancel{deg}}{\cancel{hr}} \cdot \frac{rad}{57.3\cancel{deg}} \cdot \frac{\cancel{hr}}{3600\cancel{s}} \cdot \frac{1000\cancel{m}}{100\frac{\cancel{m}}{\cancel{s}}} \quad \rightarrow \quad \sigma_{b_g} = 1.45 \times 10^{-7}$
- $0.002 \cdot \frac{\cancel{deg}}{\cancel{\sqrt{hr}}} \cdot \frac{rad}{57.3\cancel{deg}} \cdot \frac{\cancel{\sqrt{hr}}}{\sqrt{3600\cancel{s}}} \cdot \frac{1}{\sqrt{1\frac{1}{\cancel{s}}}} \quad \rightarrow \quad \sigma_{d_g} = 5.82 \times 10^{-7}$

Accelerometer (HG9900)

- $25 \times 10^{-6} \cdot \frac{10 \cdot \cancel{m}}{\cancel{s^2}} \cdot \frac{1000\cancel{m}}{(100\frac{\cancel{m}}{\cancel{s}})^2} \quad \rightarrow \quad \sigma_{b_a} = 2.50 \times 10^{-5}$
- not provided $\quad \rightarrow \quad \sigma_{d_a} \ll 2.50 \times 10^{-5}$

The accelerometer random walk value is not provided in the manufacturer specification sheet, presumably because it is small in comparison to the accelerometer bias and scale factor error. However, conversions are determined for the remaining 1-σ error terms. If the accelerometer drift error is assumed to be the same as the accelerometer bias error, then the average of the HG9900 error standard deviations is 1.3×10^{-5} compared to 1.2×10^{-5} for the average of the calibrated INS error values in Table 3.3. These average values are closer than one would expect. However, the assumption that accelerometer random walk value is equivalent to its bias value is probably the source of the error in comparison and it can be justified that the calibrated INS error values qualify as a navigation grade INS.

Appendix B: Free INS Results

B.1 Free INS with Process Noise Errors Only

This section presents the results from the free INS with only sensor drift errors.

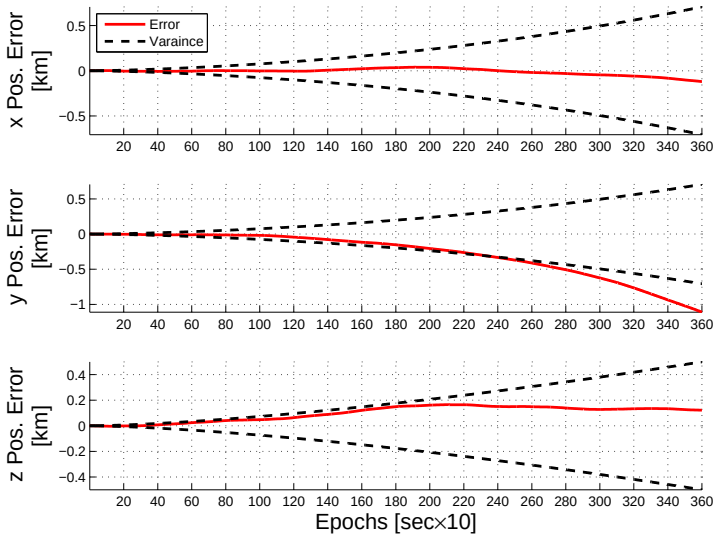

Figure B.1: Free INS position error caused by only sensor drift

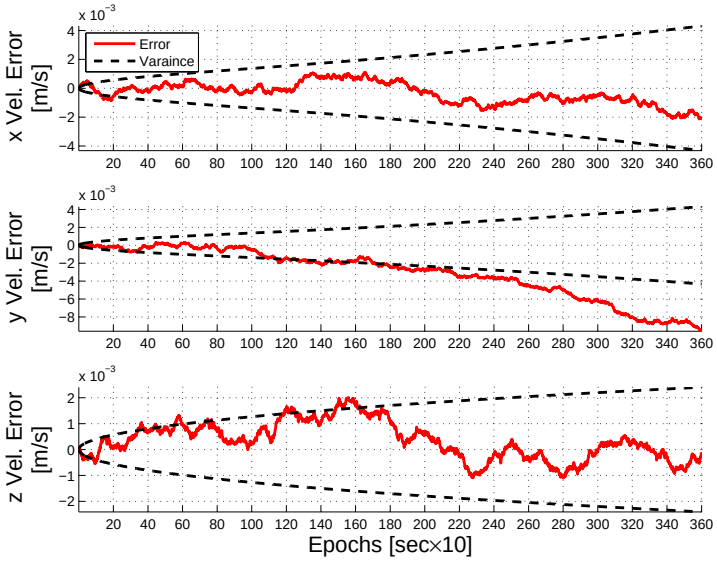

Figure B.2: Free INS velocity error caused by only sensor drift

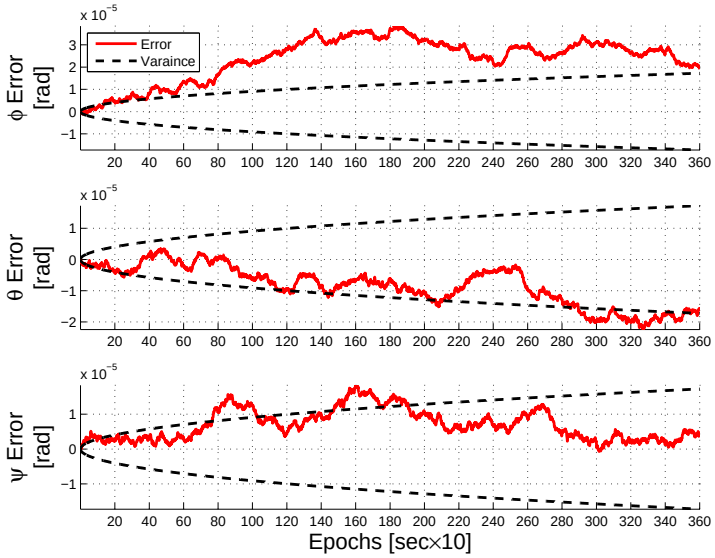

Figure B.3: Free INS attitude error caused by only sensor drift

B.2 Free INS with Bias Errors Only

This section presents the results from the free INS with only sensor bias errors.

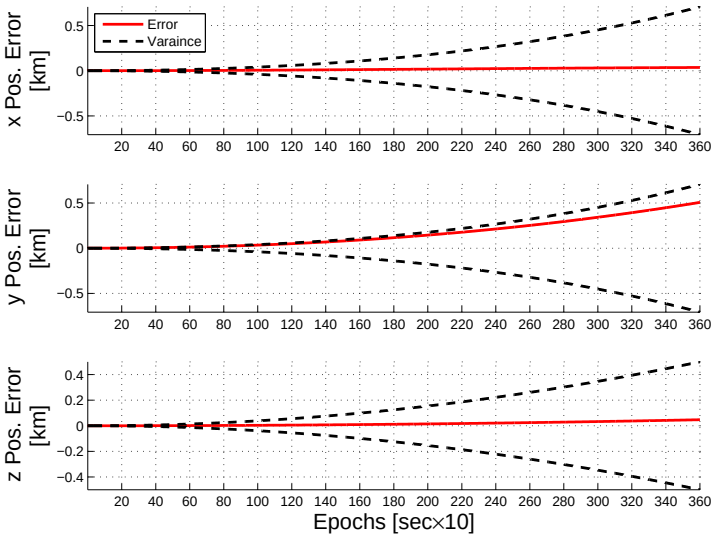

Figure B.4: Free INS position error caused by only sensor biases

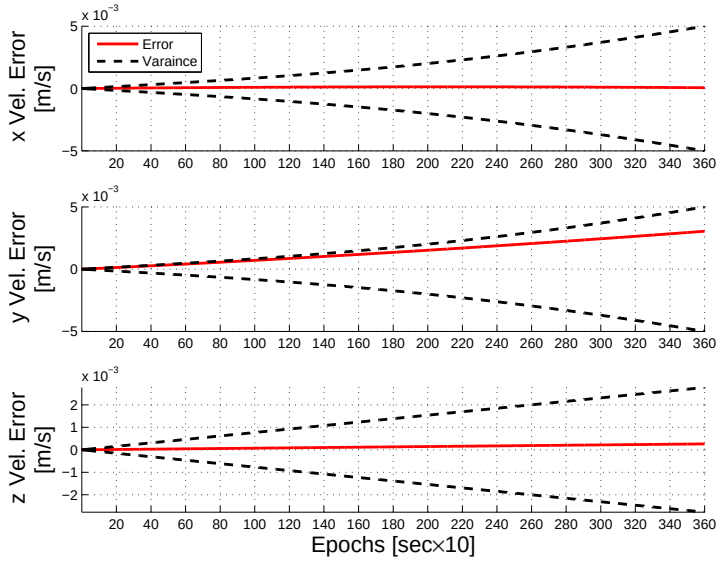

Figure B.5: Free INS velocity error caused by only sensor biases

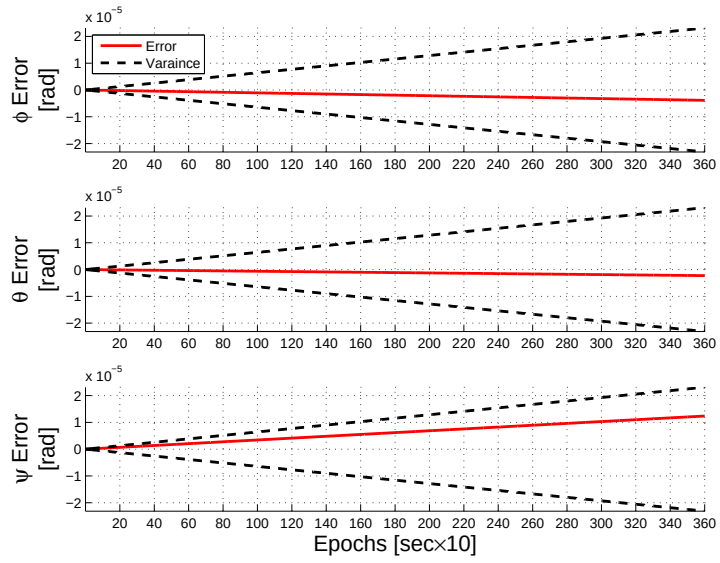

Figure B.6: Free INS attitude error caused by only sensor biases

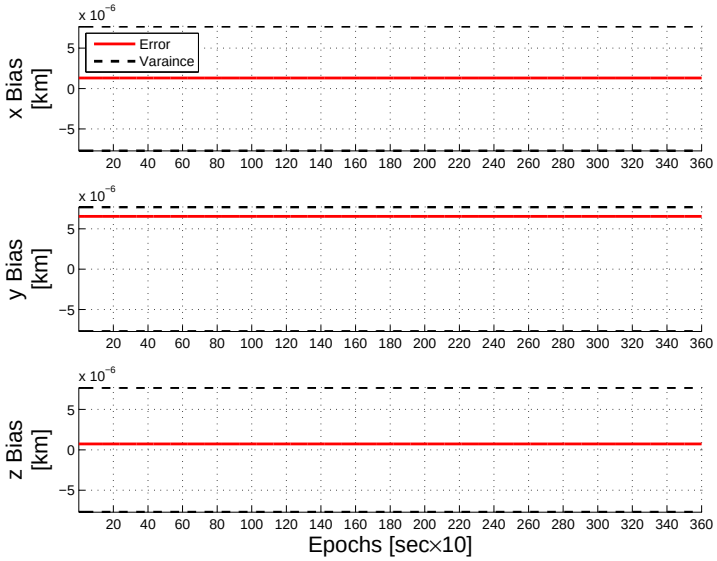

Figure B.7: Free INS accelerometer bias

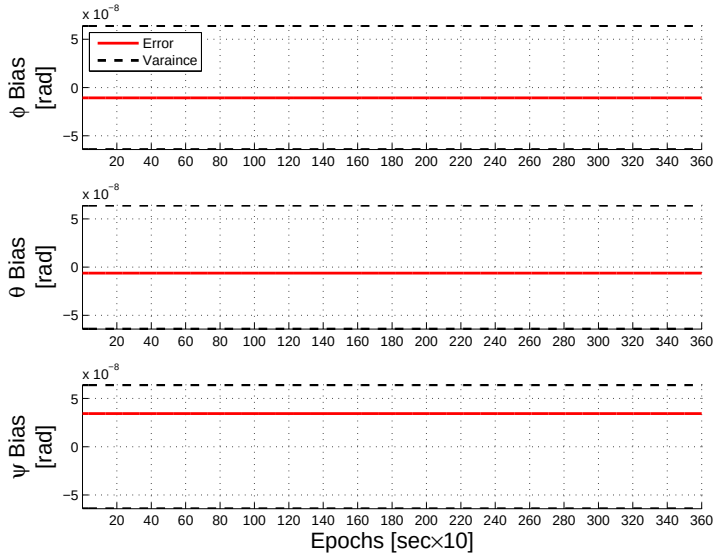

Figure B.8: Free INS gyroscope bias

B.3 Free INS with Combined Sensor Errors

This section presents the results from the free INS with both sensor drift and bias errors.

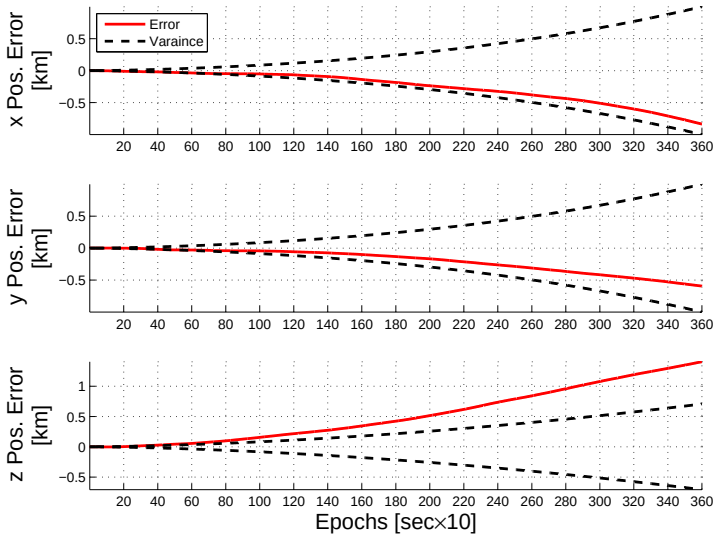

Figure B.9: Free INS position error caused by both sensor drift and biases

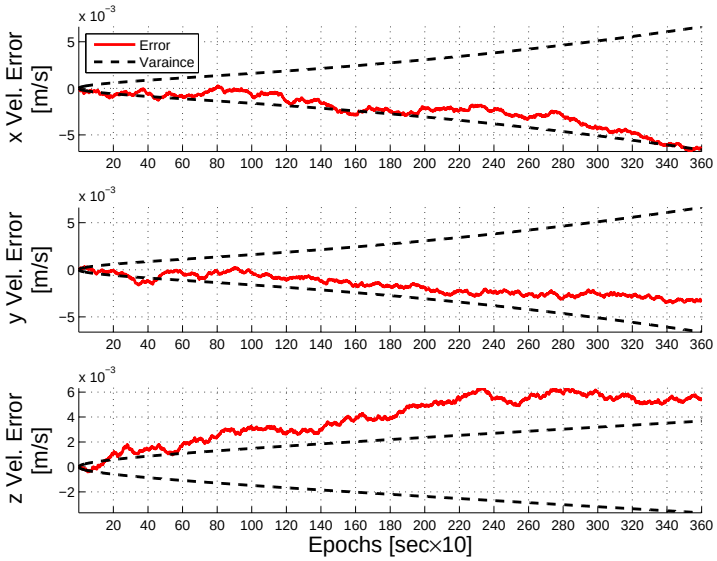

Figure B.10: Free INS velocity error caused by both sensor drift and biases

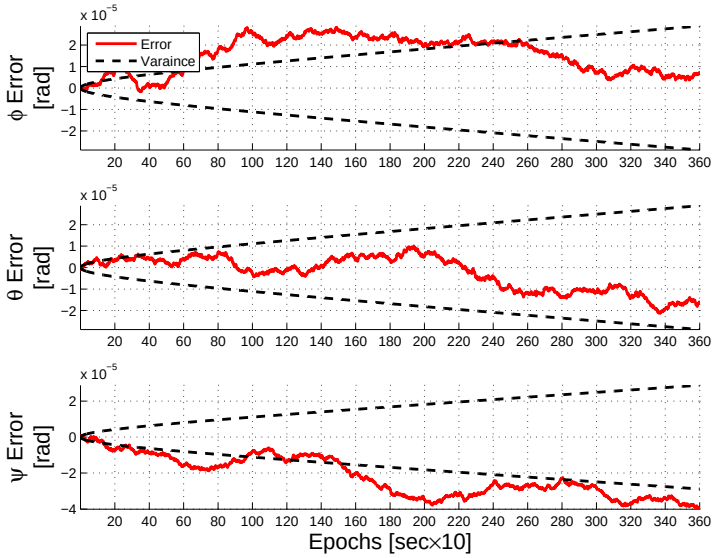

Figure B.11: Free INS attitude error caused by both sensor drift and biases

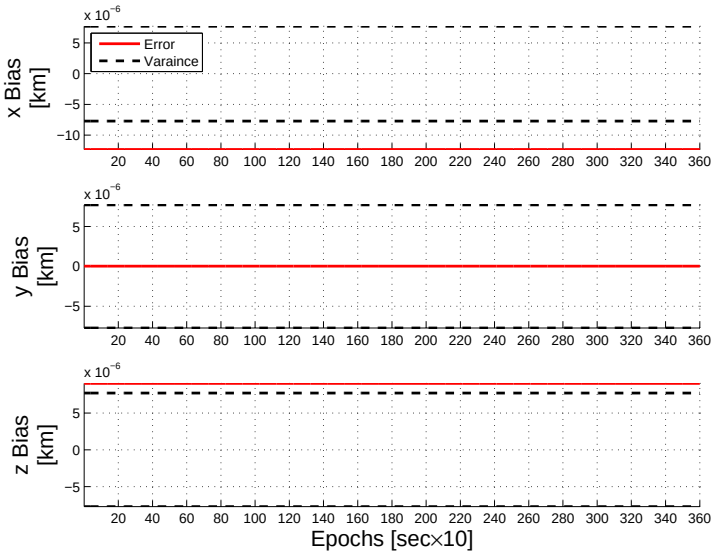

Figure B.12: Free INS accelerometer bias

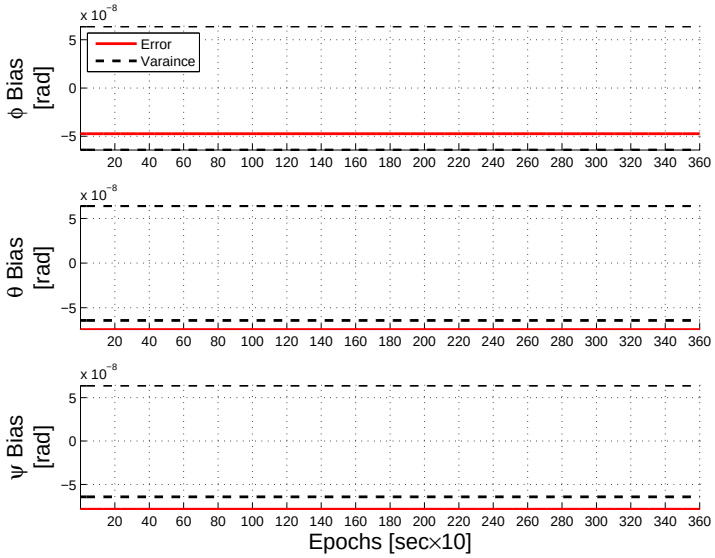

Figure B.13: Free INS gyroscope bias

Bibliography

[1] P. S. Maybeck, *Stochastic Models, Estimation, and Control*, vol. 1, 141-1. Mathmatics in Science and Engineering. Navtech Book & Software Store, republished with permission of author, 1994.

[2] R. G. Brown and P. Y. C. Hwang, *Introduction to Random Signals and Applied Kalman Filtering with MATLAB Exercises*. John Wiley & Sons, Inc., 4 ed., 2012.

[3] A. L. Relyea, "Covariance analysis of vision aided navigation by bootstrapping," Master's thesis, Air Force Institute of Technology, Wright Patterson AFB, OH, March 2012.

[4] J. O. Quarmyne, "Inertial navigation system aiding using vision," Master's thesis, Air Force Institute of Technology, Wright Patterson AFB, OH, March 2013.

[5] G. Mutlu, "The navigation potential of ground feature tracking," Master's thesis, Air Force Institute of Technology, Wright Patterson AFB, OH, September 2009.

[6] A. J. Hughes, *History of Air Navigation*. Unwin Brothers Limited Working, 1946.

[7] P. V. Weems, *Air Navigation*. Weems System of Navigation, 4th ed., 1955.

[8] L. C. Ramsey, *The Navigation of Aircraft*. The Ronald Press Company, 1929.

[9] E. Long, "Pioneer drift meter," 2012.

[10] D. A. Penland, "B-3 drift meter," 2012.

[11] W. Wrigley, "History of inertial navigation," *Navigation: Journal of The Institute of Navigation*, vol. 24, pp. 1–6, Spring 1977.

[12] E. Bekir, *Introduction to Modern Navigation Systems*. World Scientific Publishing Co. Pte. Ltd., 2007.

[13] K. R. Britting, *Inertial Navigation Systems Analysis*. Artech House, 2010.

[14] M. Grewal and A. Andrews, "How good is your gyro? ask the experts," *Control Systems, IEEE Transactions on*, vol. 30, pp. 12–86, 2010.

[15] B. W. Parkinson, T. Stansell, R. Beard, and K. Gromoz, "History of satellite navigation," *Navigation: Journal of The Institute of Navigation*, vol. 42, pp. 109–164, Spring 1995.

[16] M. J. Veth, *Optical and Inertial Sensor Fusion*. PhD thesis, Air Force Institute of Technology, Wright Patterson AFB, OH, September 2006.

[17] D. H. Titterton and J. L. Weston, *Strapdown Inertial Navigation Technology*. London, UK: The Institution of Engineering and Technology, second ed., 2004.

[18] M. Pachter, A. Porter, and M. Polat, "Ins aiding using bearing-only measurements of an unknown ground object," *Navigation: Journal of The Institute of Navigation*, vol. 53, pp. 1–20, Spring 2006.

[19] M. B. Nielsen, "Development and flight test of a robust optical-inertial navigation system using low-cost sensors," Master's thesis, Air Force Institute of Technology, Wright Patterson AFB, OH, March 2008.

[20] D. G. Lowe, "Distinctive image features from scale-invariant keypoints," *International Journal of Computer Vision*, vol. 60, pp. 91–110, November.

[21] Y. Ma and S. Rao, "Comparision of point features for vision based navigation," in *Proceedings of the 2012 International Technical Meeting of The Institute of Navigation*, (Newport Beach, CA), pp. 915–921, January 2012.

[22] H. I. Inc., "HG9900 Inertial Measurement Unit," August 2009. Datasheet.

REPORT DOCUMENTATION PAGE

Form Approved
OMB No. 0704–0188

1. REPORT DATE *(DD–MM–YYYY)*	2. REPORT TYPE	3. DATES COVERED *(From — To)*
27–03–2014	Master's Thesis	Oct 2012–Mar 2014

4. TITLE AND SUBTITLE

Automated Driftmeter Fused with Inertial Navigation

5a. CONTRACT NUMBER

5b. GRANT NUMBER

5c. PROGRAM ELEMENT NUMBER

6. AUTHOR(S)

Tuma, Allan D., Second Lieutenant, USAF

5d. PROJECT NUMBER

5e. TASK NUMBER

5f. WORK UNIT NUMBER

7. PERFORMING ORGANIZATION NAME(S) AND ADDRESS(ES)

Air Force Institute of Technology
Graduate School of Engineering and Management (AFIT/EN)
2950 Hobson Way
WPAFB, OH 45433-7765

8. PERFORMING ORGANIZATION REPORT NUMBER

AFIT-ENG-14-M-79

9. SPONSORING / MONITORING AGENCY NAME(S) AND ADDRESS(ES)

Air Force Research Laboratory
Attn: Dr. Stewart DeVilbiss
2241 Avonics Dr. bldg 620
WPAFB, OH 45433
(312)798-4413 stewart.deviliss@wpafb.af.mil

10. SPONSOR/MONITOR'S ACRONYM(S)

AFRL/RYWN

11. SPONSOR/MONITOR'S REPORT NUMBER(S)

12. DISTRIBUTION / AVAILABILITY STATEMENT

DISTRIBUTION STATEMENT A:
APPROVED FOR PUBLIC RELEASE; DISTRIBUTION UNLIMITED

13. SUPPLEMENTARY NOTES

14. ABSTRACT

The motivation of this research is to address the use of bearing-only measurements taken by an optical sensor to aid an Inertial Navigation System (INS) whose accelerometers and gyroscopes are subject to drift and bias errors. The concept of Simultaneous Localization And Mapping (SLAM) is employed in a bootstrapping manner: the bearing measurements are used to geolocate ground features, following which the bearings taken over time of the said ground features are used to improve the navigation state provided by the INS. In this research the INS aiding action of tracking stationary, but unknown, ground features over time is evaluated. It does not, however, address the critical image registration issue associated with image processing. It is assumed that stationary ground features are able to be detected and tracked as pixel representations by a real-time image processing algorithm.

Simulations are performed which indicate the potential of this research. It is shown that during wings level flight at constant speed and fixed altitude, an aircraft that geolocates and tracks ground objects can significantly reduce the error in two of its three dimensions of flight, relative to an Earth-fixed navigation frame. The aiding action of geolocating and tracking ground features, in-line with the direction of flight, with a downward facing camera did not provide improvement in the aircraft's x-position estimate. However, the aircraft's y-position estimate, as well as the altitude estimate, were significantly improved.

15. SUBJECT TERMS

Vision Aiding, INS, SLAM, Geolocation, Kalman Filter, Navigation, Image Aided-Navigation, Feature Tracking, Passive Navigation

16. SECURITY CLASSIFICATION OF:			17. LIMITATION OF ABSTRACT	18. NUMBER OF PAGES	19a. NAME OF RESPONSIBLE PERSON
a. REPORT	b. ABSTRACT	c. THIS PAGE			Dr. Meir Pachter (ENG)
U	U	U	UU	123	19b. TELEPHONE NUMBER *(include area code)* (937) 255-3636 x7247 meir.pachter@afit.edu